LLE Review

Quarterly Report

UR
LLE
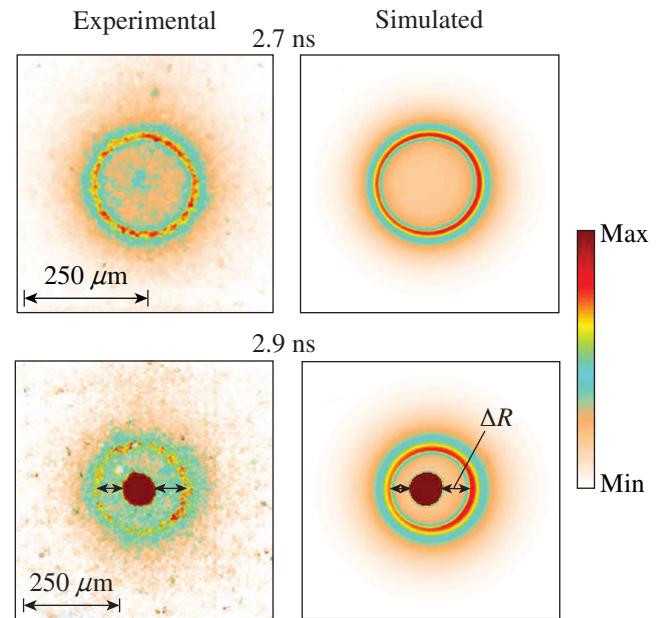
About the Cover:

The cover photo shows LLE Scientist Dr. Igor Igumenshchev in front of the LLE cluster Typhoon. He developed a three-dimensional Eulerian, radiation–hydrodynamics code, known as *ASTER*, to model the implosion of spherical targets. Typhoon is the latest cluster to be installed at LLE, with over 5000 cores, 50 TB of memory, and interconnected with an EDR (Enhanced Data Rate) Infiniband, providing the computational power necessary to run large codes such as *ASTER*.

ASTER can use the measured pointing and power history of each of the 60 OMEGA beams, the measured target offset, the measured target thickness as a function of position, and can include the target stalk in a full three-dimensional simulation of an individual OMEGA target shot. Shown to the right are experimental and simulated x-ray self-emission images for OMEGA shot 79638 at 2.7 ns and 2.9 ns, showing the ability of the code to reproduce experimental results.

Experimental 2.7 ns Simulated

250 µm

2.9 ns

ΔR

Max

Min

250 µm

Printed in the United States of America
Available from
    National Technical Information Services
    U.S. Department of Commerce
    5285 Port Royal Road
    Springfield, VA 22161
    www.ntis.gov

For questions or comments, contact Jonathan Davies, Editor, Laboratory for Laser Energetics, 250 East River Road, Rochester, NY 14623-1299, (585) 273-4679.

Worldwide-Web Home Page: http://www.lle.rochester.edu/ (Color online)

LLE Review

Quarterly Report

UR
LLE

Contents

In Brief

This volume of the LLE Review, covering October–December 2016, features "Three-Dimensional Hydrodynamic Simulations of OMEGA Implosions" by I. V. Igumenshchev, D. T. Michel, E. M. Campbell, R. Epstein, C. J. Forrest, V. Yu. Glebov, V. N. Goncharov, J. P. Knauer, F. J. Marshall, R. L. McCrory, S. P. Regan, T. C. Sangster, and C. Stoeckl (LLE); R. C. Shah (LANL); and A. J. Schmitt and S. Obenschain (NRL). This article (p. 1) considers the effects of low-mode asymmetries on OMEGA direct-drive implosions in the three-dimensional Eulerian hydrodynamic code *ASTER*. Beam-power imbalance, beam mispointing, beam mistiming, target offset, and variation in target-layer thickness are considered, using values determined from experimental measurements. *ASTER* indicates that implosion performance is mainly affected by target offset (~10 to 20 μm), beam-power imbalance ($\sigma_{rms} \sim 10\%$), and variation in target-layer thickness (~5%).

Additional research highlights presented in this issue include:

- S. X. Hu, R. Gao, and Y. Ding (LLE); and L. A. Collins and J. D. Kress (LANL) evaluate the equation of state of silicon using density-functional-theory molecular dynamics simulations for densities from 0.001 to 500 g/cm^3 and temperatures from 2000 to 10^8 K (p. 13). This first-principles equation of state (FPEOS) is compared to *SESAME* 3810. The Hugoniot from FPEOS is ~20% softer than that from *SESAME* 3810. For off-Hugoniot conditions, the pressure and internal energy from FPEOS are higher than *SESAME* 3810 below 10^4 to 10^5 K, depending on density, and lower at higher temperatures. In *LILAC* simulations of the implosion of a silicon shell, FPEOS gives ~30% higher areal density and ~70% higher neutron yield than *SESAME* 3810 because of the larger compressibility of silicon in FPEOS.

- C. J. Forrest, P. B. Radha, J. P. Knauer, V. Yu. Glebov, V. N. Goncharov, S. P. Regan, M. J. Rosenberg, T. C. Sangster, W. T. Shmayda, and C. Stoeckl (LLE); and M. Gatu Johnson (MIT) analyze measurements of the deuterium–tritium (DT) to deuterium–deuterium (DD) neutron yield ratio from cryogenic target experiments on OMEGA to evaluate species separation (p. 23). No indication of species separation is found.

- W. Theobald, A. Bose, R. Yan, R. Betti, M. Lafon, D. Mangino, A. Christopherson, C. Stoeckl, W. Seka, W. Shang, D. T. Michel, and C. Ren (LLE); R. C. Nora (LLNL); A. Casner (CEA); J. Peebles and F. N. Beg (UCSD); X. Ribeyre, E. Llor Aisa, A. Colaitis, and V. Tikhonchuk (CELIA); and M. S. Wei (GA) report results from OMEGA experiments on spherically converging shocks, comparing CH, Be, C and SiO$_2$ ablators (p. 29). CH gives 2 to 3$\times$ more hot electrons than any other ablator and a higher effective ablation pressure, which is attributed to stronger damping of ion-acoustic waves by H ions.

- C. Stoeckl, R. Epstein, R. Betti, W. Bittle, J. A. Delettrez, C. J. Forrest, V. Yu. Glebov, V. N. Goncharov, D. R. Harding, I. V. Igumenshchev, D. W. Jacobs-Perkins, R. T. Janezic, J. H. Kelly, T. Z. Kosc, R. L. McCrory, D. T. Michel, C. Mileham, P. W. McKenty, F. J. Marshall, S. F. B. Morse, S. P. Regan, P. B. Radha, B. Rice, T. C. Sangster, M. J. Shoup III, W. T. Shmayda, C. Sorce, W. Theobald, J. Ulreich,

and M. D. Wittman (LLE); D. D. Meyerhofer (LANL); and J. A. Frenje, M. Gatu Johnson, and R. D. Petrasso (MIT) present results from backlighting of cryogenic target experiments on OMEGA using Si He$_\alpha$ emission driven by OMEGA EP (p. 36). The imaging system has been used to study the evolution of nonuniform ablators, perturbations caused by mounting stalks, and carbon mix into the DT. Mix has been observed only for adiabats below 4.

- P. J. Angland, D. Haberberger, S. Ivancic, and D. H. Froula describe a new technique to extract electron density profiles from angular filter refractometry (AFR) measurements using a simulated annealing algorithm (p. 48). A seven-parameter function is chosen for the electron density and used to generate an AFR image that is compared to the measurement using a χ^2 test. The algorithm was applied to measurements of plasma expansion from a plane target and produced a fit with a statistical uncertainty of no more than 10% in the region of interest.

Jonathan Davies
Editor

Three-Dimensional Hydrodynamic Simulations
of OMEGA Implosions

Introduction

Direct-drive inertial confinement fusion (ICF) experiments conducted at the 30-kJ Omega Laser Facility[1] are used to demonstrate the hydrodynamic equivalence of scaled-down cryogenic target implosions to ignition designs at MJ energies[2] such as those available at the National Ignition Facility.[3] OMEGA implosion experiments demonstrate good agreement between the measured and simulated efficiency of conversion of the laser energy into the kinetic energy of the imploding shell (~4%). The fuel-compression stage of cryogenic implosions significantly underperforms, however, typically showing that the implosion's hot-spot pressure and deuterium–tritium (D–T) fusion neutron yield do not exceed ~60% of the values predicted in simulations using the one-dimensional (1-D) radiation–hydrodynamics code *LILAC*.[4] This and other experimental evidence, including asymmetries of x-ray images of implosion shells and hot spots, nonspherical distribution of stagnated fuel shell ρR, and ~100-km/s directional motions of hot-spot plasma, both inferred from neutron measurements, suggest that short- and long-scale nonuniformities in implosion shells can cause the observed performance degradation.[5]

Short-scale nonuniformities (corresponding to Legendre modes $\ell \gtrsim 30$) can be seeded by laser imprint[6] and small target-surface and structural defects.[7] The effects of Rayleigh–Taylor (RT) growth of these nonuniformities likely dominate over other effects of performance degradation in low-adiabat ($\alpha \lesssim 3$) and high in-flight aspect ratio (IFAR $\gtrsim 25$) implosions. Here, the adiabat α is defined in 1-D simulations as the ratio of the pressure in the imploding DT fuel shell to the corresponding Fermi-degenerated pressure and the IFAR is defined as the ratio of the shell's radius to its thickness (at a density level of 1 g/cm^3) at the moment when the ablation radius equals 2/3 of the initial radius of the inner shell.[8] The short-scale RT-growth effects can be mitigated using mid- to high-adiabat ($\alpha \gtrsim 4$) and/or low-IFAR ($\lesssim 20$) implosions.[8]

Large-scale nonuniformities (with modes $\ell \lesssim 10$) can develop because of laser illumination and structural asymmetries of implosion targets. The asymmetry of illumination is caused by the OMEGA laser's 60-beam-port configuration in addition to target offset (~10 to 20 μm) and inaccuracy of pointing, power balance, and timing of the beams (with typical $\sigma_{rms} < 10$ μm, 10%, and 5 ps, respectively). The structural asymmetries include mounting stalks,[9] variations of thickness and shape of plastic (CH or CD) ablator shells in warm and cryogenic targets (with $\sigma_{rms} < 1$ μm), and variations in thickness of the DT ice layer in cryogenic targets (with $\sigma_{rms} \sim$ 1 μm). Large-scale modes are amplified by the secular and Bell–Plesset[10] growths and by the RT growth during the deceleration and stagnation stages. Variations of α and IFAR have little effect on the growth of these modes.

Investigation of the effects of large-scale asymmetries and the development of strategies to mitigate them are important steps toward improving the performance of OMEGA implosions. To understand these effects, experimental observations of implosion asymmetries are simulated in detail employing the three-dimensional (3-D) radiation–hydrodynamics code *ASTER*.[11] Results of 3-D simulations are post-processed to be directly compared with observables, which include x-ray images and deuterium–deuterium (DD) and/or DT fusion neutron spectra, among others.

This article describes recent progress in 3-D *ASTER* simulations of room-temperature and cryogenic OMEGA implosions focusing on large-scale ($\ell \lesssim 10$) target asymmetries as sources of the degradation in implosion performance. Simulations show that mode 1 is typically the most-destructive one in the case of both room-temperature and cryogenic implosions. The presence of this mode results in relatively large residual kinetic energy of implosion shells at maximum compression in comparison with that resulting from other modes (≥ 2) of similar amplitude. This large residual kinetic energy causes undercompression of the hot spot and a reduction of neutron yields down to values found in experiments. Mode 1 can be observed as an offset of the core emission in x-ray images with respect to the initial target center and as a directional variation of neutron spectra.

All above-mentioned sources of long-scale nonuniformities (except for that caused by the OMEGA discrete-beam illumination,[11] which introduces a dominant mode $\ell = 10$) can contribute to mode-1 perturbations. Mount stalks and target offsets apparently result in such perturbations. Beam mistiming, mispointing, and imbalance, as well as initial target structural asymmetry, can be considered as quasi-random sources and result in perturbations having broad spectra, which peak at the lowest modes from 1 to ~3 and gradually decline toward higher modes. Recent 3-D simulations suggest that the latter sources can be important contributors to mode-1 asymmetries.

The goal of this work is to estimate the relative importance of different sources of large-scale nonuniformities in developing asymmetries in OMEGA implosions. This will help to specify improvements in both the OMEGA laser and target fabrication that can lead to improved implosion performance and a better understanding of the physics and robustness of the laser direct-drive approach. Understanding the sources of nonuniformities requires 3-D simulations assuming laser illumination and initial target structural asymmetries that are suggested by direct and indirect measurements and pre-shot target characterization. Results of these simulations are compared with asymmetries of implosion shells measured at different evolution stages, ranging from the beginning of shell acceleration until bang time.

The following sections (1) briefly describe the code *ASTER* and recent developments; (2) present results of 3-D *ASTER* simulations of room-temperature and cryogenic implosions and compare these results with experiments; and (3) present our discussion and conclusions.

The Numerical Method

Large-scale nonuniformities in OMEGA implosions were simulated using the 3-D radiation–hydrodynamics code *ASTER*. This code was tested against 1-D *LILAC* and two-dimensional (2-D) *DRACO*[12] results, showing good agreement with both results.[11]

ASTER is an Eulerian code implemented on a spherical grid. Its hydrodynamic algorithm is based on the piecewise-parabolic Godunov method.[13] This code uses a 3-D simplified laser-deposition model, which assumes inverse bremsstrahlung for light absorption and includes cross-beam energy transfer (CBET),[14] and electron and ion Spitzer thermal transport[15] without flux limitation. *ASTER* can use various on-the-fly and post-processing diagnostic routines that simulate, for example, neutron spectra and images, burn history, x-ray images, etc.

ASTER is characterized by low numerical noise that allows one to simulate nonuniform implosions without using any kind of diffusion or Fourier filtering to reduce the noise. Figure 149.1

TC13236JR
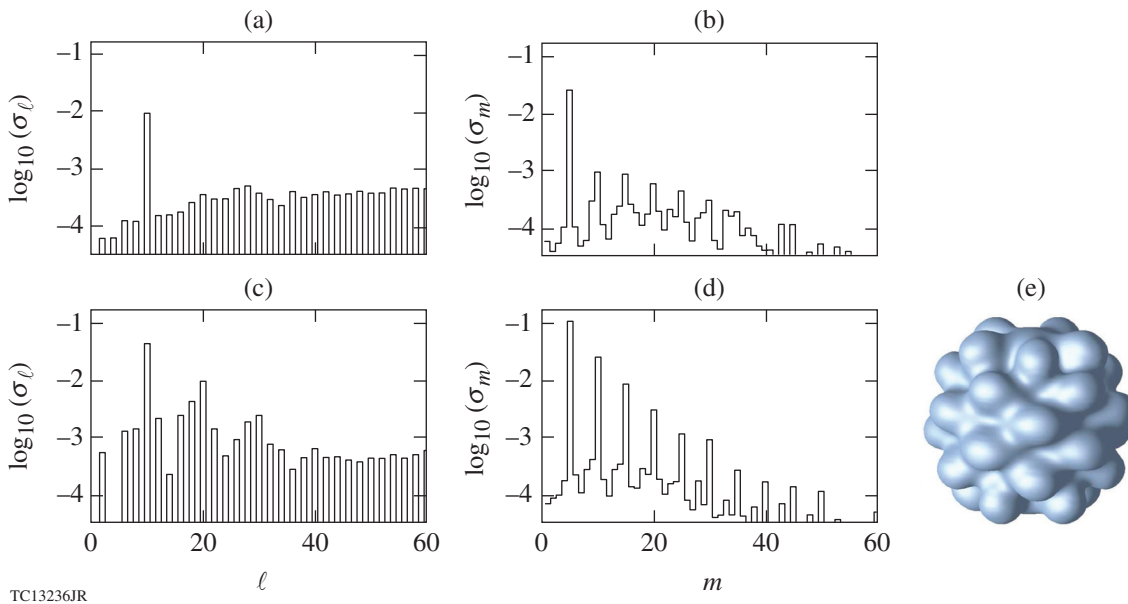
Figure 149.1
Three-dimensional *ASTER* test simulation assuming 1% perturbation of the mode $(\ell,m) = (10,5)$ in laser deposition. [(a),(b)] The power spectra σ_ℓ and σ_m [see Eq. (1)] of the areal-density perturbation, respectively, at the end of the laser pulse, $t = 2.52$ ns; [(c),(d)] these spectra at $t = 2.805$ ns, which corresponds to $t_{bang} + 30$ ps. (e) An illustration of the shape of the hot spot at the latter time showing an isosurface of $T_i = 1$ keV.

shows example simulations of OMEGA cryogenic shot 77066 (see **Cryogenic Implosions**, p. 7) assuming a 1% perturbation of mode $(\ell,m) = (10,5)$ in laser deposition. This simulation uses a numerical grid of 64×128 zones in the θ and ϕ dimensions, respectively. Figures 149.1(a)–149.1(c) show resulting normalized power spectra σ_ℓ and σ_m of the angular distribution of the areal density. These spectra are defined as follows:

$$\sigma_\ell = \sqrt{\sum_{m=-\ell}^{\ell} \sigma_{\ell,m}^2} \quad \text{and} \quad \sigma_m = \sqrt{\sum_{\ell=1}^{\ell_{\max}} \sigma_{\ell,m}^2}, \qquad (1)$$

where $\sigma_{\ell,m}^2 = \left(C_{\ell,m}/C_{00}\right)^2$ and $C_{\ell,m}$ are the expansion coefficients on the real (tesseral) spherical harmonics. Figures 149.1(a) and 149.1(b) show these spectra at the end of the laser pulse, $t = 2.52$ ns, when the shell's implosion velocity approaches its maximum. One can see in these figures that the fundamental modes $\ell = 10$ and $m = 5$ dominate by more than an order of magnitude over the level of background noise introduced by numerical effects. At this time, the fundamental mode experiences mainly secular growth and is insignificantly affected by RT growth because of its relatively large wavelength. Figures 149.1(c) and 149.1(d) show the same spectra at $t = 2.805$ ns, which is about 30 ps after bang time, or peak neutron rate. At this time the shell is at maximum compression and is just beginning to move outward. Here, the shell undergoes an efficient RT growth and the perturbations become nonlinear, so that harmonics with $\ell = 20$, 30, and 40 and $m = 10$, 15, ... are clearly visible and dominate over the background noise. These harmonics are still, however, below the amplitude of the fundamental mode $(\ell,m) = (10,5)$. Figure 149.1(e) shows the 3-D structure of the hot spot at $t = 2.805$ ps, represented by a 1-keV ion temperature isosurface.

Recent developments of *ASTER* include the capability to simulate radiation transport using multigroup flux-limited diffusion.[16] This development is important since it makes it possible to accurately simulate room-temperature plastic-shell implosions, in which radiative ablation of the inner edge of the dense shell at maximum compression is important. Radiation transport is implemented using the parallel geometric multigrid algorithm.[17] The use of spherical grids with anisotropies near the poles and typically higher resolution in the radial direction (versus angular directions) requires modifications to the standard multigrid relaxation and coarsening procedures to retain optimal efficiency.[18] To treat the polar anisotropies, the algorithm uses nonuniform coarsening strategies, in which the grid is coarsened only in regions and directions that have sufficient isotropic grid coverage. This is combined with line

relaxation (using the marching algorithm) in the radial direction. The algorithm is adapted for parallel calculations using a domain decomposition approach similar to that used in the hydrodynamic part of *ASTER*.[11] Intensive test simulations have been performed to check the accuracy of the radiation-transport routine in *ASTER*. Results of these simulations showed good agreement with corresponding results obtained using *LILAC* and *DRACO*.

Simulation Results

The goal of this study is to identify the effects of large-scale asymmetries in OMEGA implosions with the help of 3-D simulations including a variety of nonuniformities in laser illumination and target structure. The nonuniformities can be chosen only to investigate their effects based on measurements. In the latter case, simulation results are compared with experiments.

Laser-induced nonuniformities include those created by the OMEGA beam-port geometry, target offset, and beam power imbalance, mistiming, and mispointing. The initial target structure nonuniformities can be caused by a variation in the thickness and shape of plastic shells in room-temperature and cryogenic targets and DT-ice shells in cryogenic targets.

The effects of beam imbalance and mistiming in *ASTER* simulations are included by using the power history of individual laser beams measured on a particular shot. This history is measured before laser light enters the target chamber; therefore, it can be different from the actual on-target value, which is affected by beam-forming optics and protective blast windows. The effects of the latter two are included in simulations by applying time-independent "imbalance correction" factors, which increase or reduce the power of individual beams. These factors are inferred using cross-calibration analysis of time-integrated x-ray images of laser spots from all 60 beams illuminating 4-mm-diam gold sphere targets with a 1-ns square pulse.[19] These targets are chosen to be larger than the nominal OMEGA targets (with radius $R_t = 430\ \mu$m) to avoid the overlapping of laser spots (with radius $R_b \approx 430\ \mu$m). The imbalance correction factors are typically determined with the accuracy corresponding to about 1% to 2% of the beam power.

Beam mispointing is inferred using the same x-ray data from 4-mm-diam gold targets as in the case of the imbalance measurements.[19] The mispointing data are determined with the accuracy of ~5 μm and assumed to be fixed in time. These data are provided as horizontal (δx) and vertical (δy) displacements of laser spots with respect to their nominal positions on the target surface. *ASTER* models beam mispointing by

displacing the deposition regions for each beam by the angles of $\delta\theta = \delta y/R_{dep}$ and $\delta\phi = \delta x/R_{dep}$ in the spherical coordinates, where R_{dep} is the radius of the deposition region.

Target offset, or displacement of target center with respect to the laser pointing center, is measured using x-ray imaging[20] with an accuracy of about ±3 to 5 μm. Offsets are typically small for warm implosions (<5 μm) and can be significant for cryogenic implosions (~10 to 20 μm). *ASTER* models target offsets by displacing the deposition region of each beam by angles $\delta\theta$ and $\delta\phi$, which are calculated depending on the offset and its directionality and the radius R_{dep}.

Cryogenic and room-temperature targets are routinely used in OMEGA experiments to study implosion physics. While implosions of these targets share many common physical effects, there are important differences in experimental setups, initial target uniformity, and details of implosion physics that require separate considerations. First we will describe the *ASTER* simulations of room-temperature implosions. These simulations reproduce well the amplitude of observed asymmetries in implosion targets but not the directionality of these asymmetries. Next we will consider the results of cryogenic implosion simulations, which yield similar conclusions: there is good reproduction of the asymmetry amplitudes, but not directionality. The lack of agreement with the directionality can be explained by an inaccuracy of the assumed nonuniformities, which are measured within the time and space resolu-

tion of the diagnostics, while some of them are inferred from indirect measurements.

1. Room-Temperature Implosions

Room-temperature implosions have several advantages with respect to their cryogenic counterparts that make them a preferable choice for an initial study of large-scale asymmetries: (1) the relatively low fabrication and operation costs that result in an increased shot rate, (2) the ability to add high-Z dopants to the shell that is not fully ablated and confines fuel at stagnation, (3) smaller target offsets, and (4) relatively small initial target nonuniformities. The latter two allow one to concentrate on studying laser-induced asymmetries, whereas the ability to add dopants can help to quantify implosion core asymmetry using self-emission x-ray radiography.

Figure 149.2 shows two warm implosion designs that correspond to OMEGA shots (a) 79638 and (b) 79972. These designs have an IFAR ≈ 18 and 27, respectively, and are relatively stable with respect to high-mode ($\ell \gtrsim 30$) RT growth. Shot 79638 (a) uses a 10-atm D_2–filled, 27-μm-thick plastic (CH) shell. Simulations of this shot are used to study implosion asymmetry during the laser drive and are compared with self-emission x-ray images (at $h\nu > 1$ keV) of implosion shells.[21] This x-ray emission comes mainly from a thin layer of plasma located immediately outside the ablation surface. Such images, therefore, can be used to measure the shape and outer radius of implosion shells.
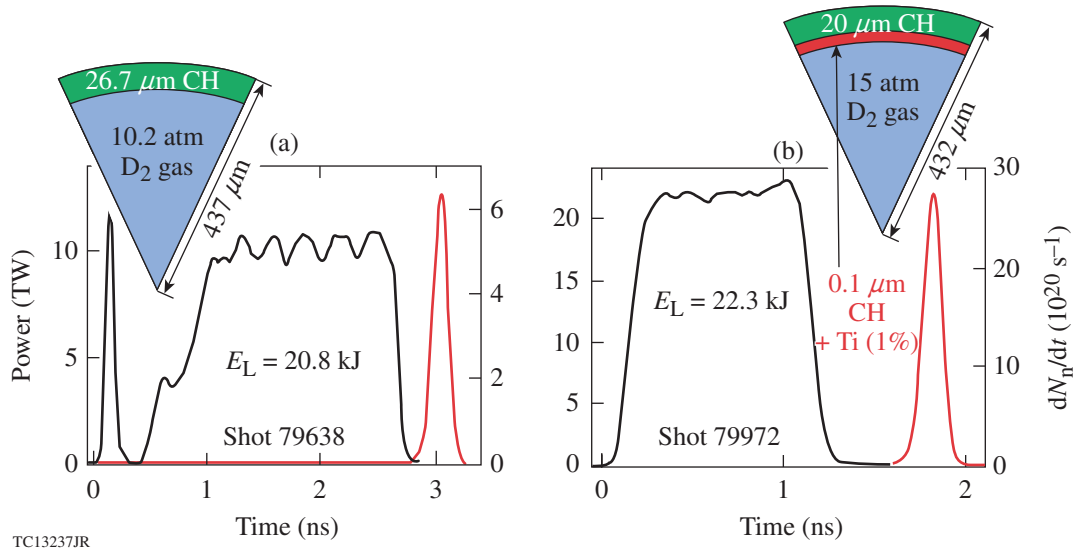

TC13237JR

Figure 149.2
Schematic target structure, laser pulse (in black), and simulated neutron rate (in red, left axis) of two warm implosion designs corresponding to OMEGA shots (a) 79638 and (b) 79972.

The design in Fig. 149.2(b) (shot 79972) uses a 15-atm D_2–filled, 20-μm-thick plastic shell, which is doped by Ti (1% by atom) at the inner surface to a depth of ~0.1 μm. The purpose of this dopant is to characterize the shape and physical conditions at the fuel–ablator interface using Ti He$_\beta$ line emission (in the 5.45- to 5.65-keV x-ray band) at the time of hot-spot formation since this line emits at $T_e \gtrsim 1$ keV (Ref. 22).

Figures 149.3(a) and 149.3(b) compare experimental and simulated self-emission images, respectively, from shot 79638 at $t = 2.7$ ns (the TIM-5 viewing direction at $\theta = 100.8°$ and $\phi = 270°$ in the OMEGA coordinates). These images represent the shape of the ablation surface at the end of the acceleration phase. The simulations assume the known illumination nonuniformity seeds: OMEGA beam overlap and measured individual beam power histories (which introduce beam imbalance and mistiming) and mispointing (with $\sigma_{rms} \approx 16$ μm). The measured and simulated images were post-processed[23] to determine perturbations of the ablation surface. Figure 149.4 shows the evolution of the amplitude and phase of mode-2 perturbations in experiment and simulations. The measured mode-2 amplitude grows in time in good agreement with simulations [see Fig. 149.4(a)]. The mode-2 phases are almost independent in time in both experiment and simulations, but they are different by about 40° [see Fig. 149.4(b)]. The latter discrepancy in the phases suggests that the nonuniformity seeds assumed in simulations do not accurately represent the actual seeds.
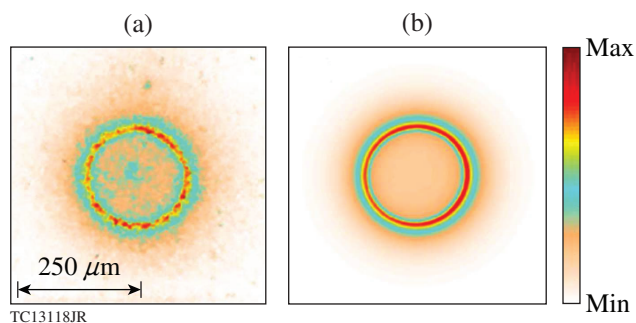
indicates significant mode-1 perturbations. The offset and its direction are in good agreement in both experimental and simulated images. Simulations show that this offset corresponds to mode-1 distortion of the implosion shell and fuel volume at bang time, as shown in Fig. 149.6. As a result, the simulated neutron yield 4.49×10^{10} is reduced to 43% of the yield of the corresponding uniform (1-D) implosion. This yield is a factor of 3 larger, however, than the measured yield $(1.79 \pm 0.09) \times 10^{10}$. Several factors explain the better-simulated performance: (1) an underestimation of the assumed nonuniformity seeds,
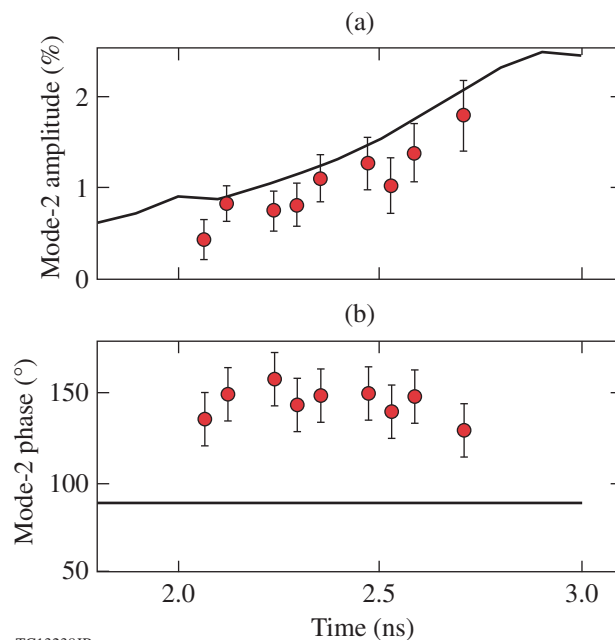
Figure 149.4
Evolution of (a) amplitude and (b) phase of mode-2 perturbations of the ablation surface in shot 79638 (TIM-5 view). Measurements are shown by red dots with error bars and simulations are shown by black lines.

Figure 149.3
(a) Experimental and (b) simulated broadband x-ray ($h\nu > 1$ keV), self-emission images of the implosion shell in shot 79638 at $t = 2.7$ ns (TIM-5 view).

Figures 149.5(a) and 149.5(b) compare experimental and simulated self-emission images of shot 79638 at $t = 2.9$ ns (in the same viewing direction as in Fig. 149.3). At this time, emissions from the ablation surface (outer ring) and from the core (center spot) are observed simultaneously. The offset of the core (~5 μm), which is seen as a directional variation of the gap ΔR between the core edge and ablation surface edge in Fig. 149.5,

Figure 149.5
(a) Experimental and (b) simulated self-emission images of shot 79638 at $t = 2.9$ ns. The offset of the emitting core (center spot) with respect to the image of the ablation surface (ring) represents the mode-1 perturbation.

TC13240JR

Figure 149.6

(a) Meridional and (b) equatorial cross sections of the distribution of density from simulations of room-temperature shot 79638 at peak neutron production, $t = 3.02$ ns. The dashed line in (a) shows the equatorial plane and in (b) the location of the cross-section plane in (a). The solid line inside the dense shell shows the fuel–ablator (D–CH) interface.

(2) missing effects of small-scale mix that were not included in simulations; and/or (3) an inaccuracy in prescribing 1-D physics effects (laser absorption, CBET, heat transport, preheat, etc.).

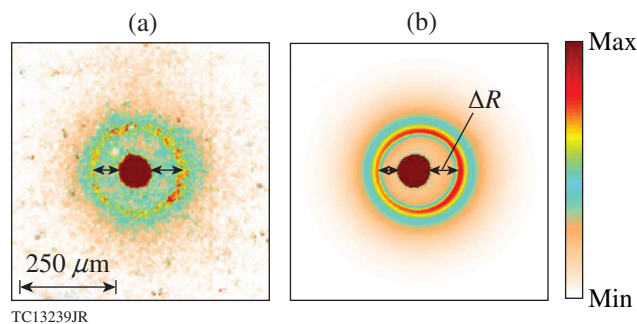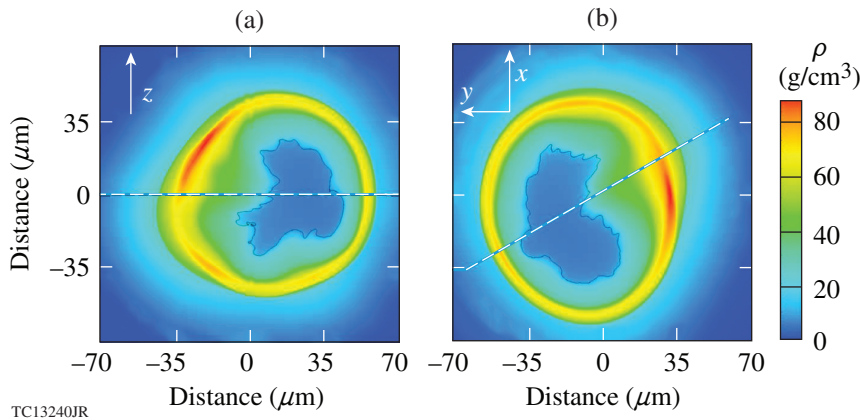Another example of significant mode-1 perturbation in OMEGA implosions is presented by shot 79972. Here, mode 1 was measured at a time near target stagnation. Figure 149.7 compares narrowband Ti He$_\beta$ emission images from this shot at two times, $t \approx t_{bang} - 100$ ps and $t \approx t_{bang}$. The emission limb, which corresponds to the location of the fuel–ablator (D–CH) interface, is consistently brighter on one side in both images, indicating the presence of dominant mode-1 asymmetry in the implosion core. The imager was located opposite the mounting stalk, so the limb asymmetry is unlikely to be caused by the stalk. There is a bright spot inside the limb, which is clearly observed in Fig. 149.7(a) at the earlier time and less clearly in Fig. 149.7(b) at the later time. This spot can be attributed to a jet that penetrates the hot spot and is introduced by the mounting assembly (stalk and glue spot).[9]

The observed mode-1 asymmetry in shot 79972 is likely caused by laser-illumination nonuniformities and can be quantified by comparing it with results of *ASTER* simulations. Figure 149.8 shows simulated distributions of the density and electron temperature in the equatorial cross section of shot 79972, assuming measured individual beam-power histories and pointing misalignment. The assumed perturbations result in mode-1 asymmetry of the dense CH-ablator shell and wide directional motion of the fuel material, which can be seen in Fig. 149.8 as distortion of the hot, low-density central volume occupied by this material. There is also a narrow, high-velocity jet moving in the same direction as the wide flow. This jet develops in the fuel material during successive bouncing of converging shocks produced by the shell during its deceleration. The yellow arrow in Fig. 149.8(a) indicates the directions

TC13123JR
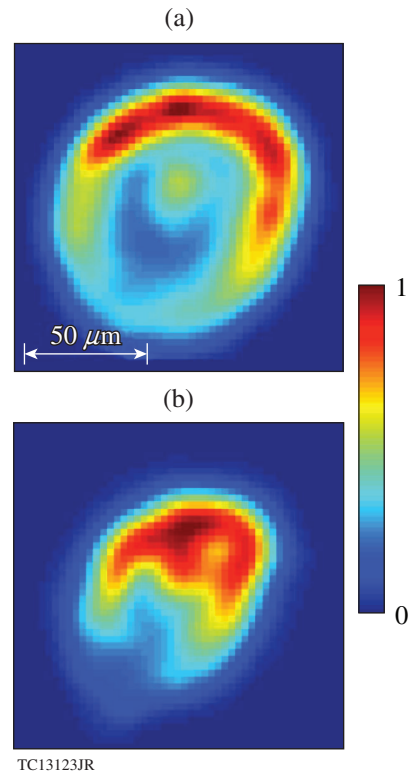
Figure 149.7

Narrowband Ti He$_\beta$ (from 5.45 to 5.65 keV) images for shot 79972 at (a) $t \approx t_{bang} - 100$ ps and (b) $t \approx t_{bang}$. The view is opposite the position of the target-mounting stalk.

of the wide flow and jet and points to a dip in the ablator shell into which the jet "drills."

The solid (color) line inside the dense shell in Fig. 149.8(a) shows the fuel–ablator interface, at which the Ti-doped material is concentrated [see Fig. 149.2(b)]. Simulated images of Ti He$_\beta$ line emission from this implosion are presented in Fig. 149.9.

TC13241JR
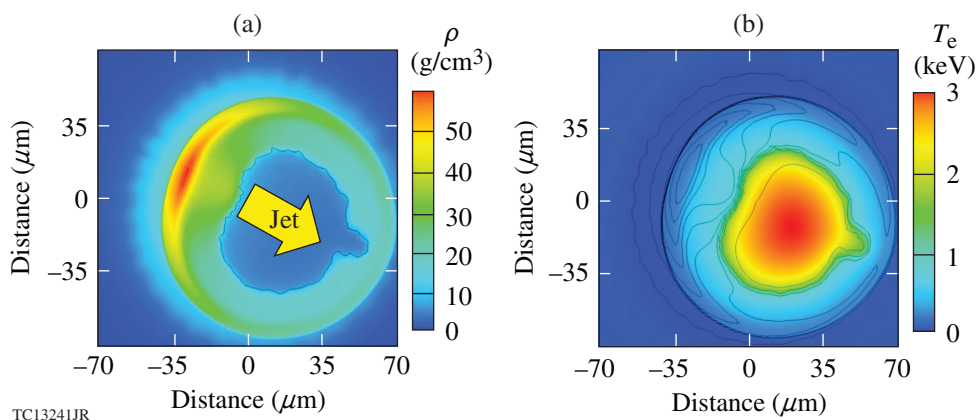
Figure 149.8

Equatorial cross sections of the distribution of (a) density and (b) electron temperature in simulations of shot 79972 at peak neutron production, $t = 1.785$ ns. The solid line in (a) shows the fuel–ablator interface where Ti-doped CH material is located. The arrow indicates the direction of a wide flow and jet, which develop in the hot-spot plasma because of the mode-1 perturbation. The solid lines in (b) show linearly spaced contours of the electron number density.

TC13242JR

Figure 149.9

Simulated Ti He$_\beta$ images for shot 79972 at (a) $t = t_{bang} - 80$ ps and (b) $t_{bang} = 1.785$ ns. The viewing direction is from the pole and (b) corresponds to the distributions of density and electron temperature shown in Fig. 149.8, but at a different azimuthal orientation. The arrow in (a) points in the same direction of the jet in Fig. 149.8(a).

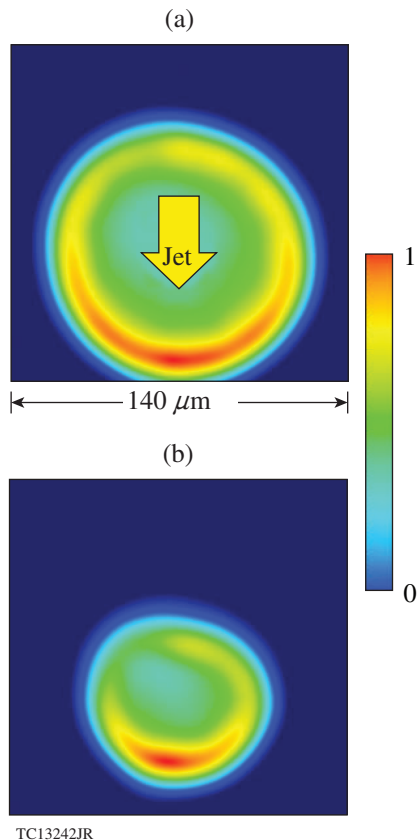These images are calculated for the polar view and correspond to $t = t_{bang} - 80$ ps and $t = t_{bang}$, where $t_{bang} = 1.785$ ns [Figs. 149.9(a) and 149.9(b), respectively], and were produced by applying the same spatial (≈ 10-μm) and temporal (≈ 40-ps) smearing as in the experiment. The arrow in Fig. 149.9(a) shows the direction of the wide flow in the hot spot and corresponds to the same direction as in Fig. 149.8(a).

Simulations indicate that the asymmetry of the limb emission observed in shot 79972 (Fig. 149.7) is related to the wide directional motion of the fuel material caused by the mode-1 asymmetry of the shell. The brighter side of the emission limb develops in the direction of this motion. A detailed analysis shows that this brightening is mainly attributed to a local increase of T_e in the corresponding part of the fuel–ablator interface, while the role of variation in n_e is less significant [see Fig. 149.8(b)].

By comparing Figs. 149.7 and 149.9, one finds that while experiment and simulations show good agreement with respect to the amplitude of limb brightening, they disagree in directionality of this brightening. This disagreement is similar to that found in the simulations of shot 79638 (see Fig. 149.4) and confirms the claim that illumination nonuniformity seeds assumed in simulations do not accurately represent the real on-target seeds.

2. Cryogenic Implosions

Figure 149.10 shows a target schematic, pulse shape, and neutron history (from 1-D simulations) for shot 77066—one of the best-performing cryogenic OMEGA implosions—in which
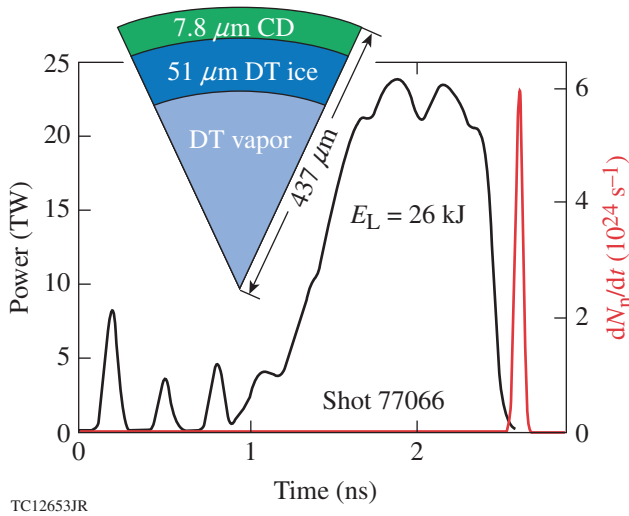
TC12653JR

Figure 149.10
Schematic of the cryogenic capsule, laser pulse (black line), and simulated neutron rate (red line, right axis) for OMEGA shot 77066.

about 56 Gbar of hot-spot pressure was inferred.[24] This shot is characterized by an $\alpha \approx 3.2$ and IFAR ≈ 24 and should be relatively stable with respect to short-scale RT growth. The neutron yield, neutron-averaged (over DT neutrons) ion temperature $(T_i)_n$, and hot-spot pressure from uniform (1-D) *ASTER* simulations of this shot are 2.06×10^{14}, 3.39 keV, and 138 Gbar, respectively, and using *LILAC* they are 1.72×10^{14}, 3.67 keV, and 115 Gbar, respectively. *ASTER* simulations result in the absorption fraction of laser energy $f_{abs} = 0.54$ and bang time $t_{bang} = 2.66$ ns, while these results from *LILAC* are 0.60 and 2.68 ns, respectively. Table 149.I summarizes these results as well as the results of measurements. The discrepancies between the 1-D *ASTER* and *LILAC* results are relatively small and can be attributed to differences in the hydrodynamic methods used (Eulerian piecewise-parabolic method in *ASTER* and Lagrangian finite-difference scheme in *LILAC*) and the physical models (e.g., Spitzer versus nonlocal[25] heat transports, respectively).

Three-dimensional simulations of shot 77066 assume all sources of nonuniformities that can be currently quantified.

These include the power history of each individual beam, a target offset of 4 μm (in the direction of $\theta = 83°$ and $\phi = 315°$), and an ice-shell thickness variation with a mode-1 amplitude of 2 μm (oriented vertically, where the bottom is thinner), which were all measured in this shot. Simulations also assume beam-power imbalance correction factors and mispointing data (with $\sigma_{rms} = 8.5$ μm), which were measured in pointing shot 77059.

Figures 149.11(a) and 149.11(b) show, respectively, the equatorial and meridional (at $\phi = 83°$) cross sections of the distribution of density at peak neutron production, $t = 3.572$ ns. Figure 149.12 shows a 3-D view of the hot spot at the same moment, where the hot-spot shape is represented by the isosurface $T_i = 900$ eV. The assumed sources of nonuniformities result in a distortion of the dense shell with the dominant mode 1. This mode can be clearly observed in Figs. 149.11(a) and 149.12 as an ~10-μm shift of the dense shell and hot-spot centroids in the direction $\theta \approx 30°$ and $\phi \approx 83°$ with respect to the initial target center that was located at the origin. The shell is more dense on the side opposite the direction of the shift because of larger laser drive on that side resulting in higher convergence of the shell mass.

Simulations with the assumed asymmetries predict a yield of 8.07×10^{13} neutrons and $(T_i)_n = 3.03$ keV, therefore reducing the yield to 39% and $(T_i)_n$ to 89% of the corresponding values of uniform *ASTER* simulations. The measured neutron yield is $(3.9 \pm 0.2) \times 10^{13}$, which corresponds to 23% of the yield of *LILAC* simulations (see Table 149.I).

Neutron-averaged ion temperatures in OMEGA implosions are routinely inferred from DD and DT neutron spectra that include the thermal smearing and bulk motion effects in the hot spot.[26] In the case of cryogenic OMEGA implosions, DT neutron spectra are measured by detectors at three different directions: (1) $\theta = 84.98°$ and $\phi = 311.76°$, (2) $\theta = 87.86°$ and $\phi = 161.24°$, and (3) $\theta = 61.30°$ and $\phi = 47.64°$. These directions are indicated by the white dashed arrows in Fig. 149.11(a). The inferred ion temperatures in shot 77066 in these directions are

Table 149.I: Simulated and measured performance of OMEGA cryogenic shot 77066.

	Neutron yield	$(T_i)_n$ (keV)	P_{hs} (Gbar)	f_{abs} (%)	t_{bang} (ns)
LILAC	1.72×10^{14}	3.67	115	60	2.68
1-D *ASTER*	2.06×10^{14}	3.39	138	54	2.66
3-D *ASTER*	8.07×10^{13}	3.03	88	54	2.66
Experiment	$(3.9 \pm 0.2) \times 10^{13}$	N/A[*]	56±7	58±1	2.60±0.05

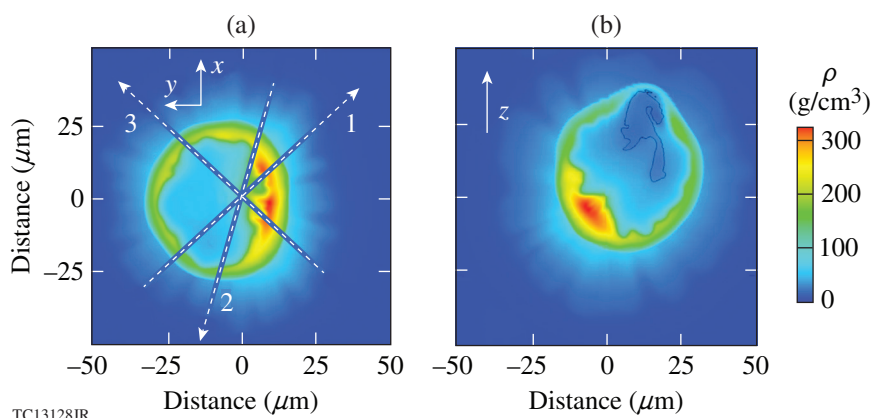[*]$(T_i)_n$ in the absence of bulk motion cannot be measured.

(a)   (b)

TC13128JR

Figure 149.11

Distribution of density in simulations of shot 77066 in the (a) equatorial and (b) meridional (at $\phi = 83°$) planes at peak neutron production, $t = 3.57$ ns. These simulations assume various nonuniformities in laser drive and initial target structure (see text). The white arrows show the coordinate axis indicating orientation of the images. The white dashed arrows show the three directions in which neutron data were collected.
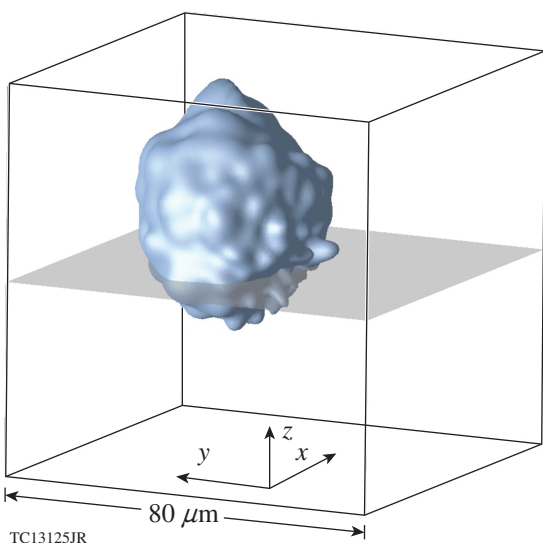

TC13125JR

Figure 149.12

A 3-D view of the isosurface $T_i = 900$ eV, which represents the shape of the hot spot at peak neutron production in the same simulations as in Fig. 149.11. The cube with side sizes of 80 μm with the center at the origin and coordinate basis indicate spatial scale and orientation. The equatorial plane is shown in gray.

measurements and simulations show good agreement for the amplitude of directional variation of T_i: the measured difference between the minimum and maximum temperatures is 0.6 keV, while the simulated difference is 0.9 keV. The latter agreement indicates that simulations correctly reproduce the actual magnitude of hot-spot asymmetry.

Shifts of the simulated neutron spectra in energy in Fig. 149.13 with respect to the unshifted energy of DT neutrons, $E_n = 14.1$ MeV, show a correlation with the direction of the hot-spot shift (see Fig. 149.11) caused by bulk motions. The spectra in red and green in Fig. 149.13 are shifted by $\Delta E \approx 40$ keV to smaller and larger energies, respectively. These spectral shifts are explained by negative and positive projection components

TC13128JR2
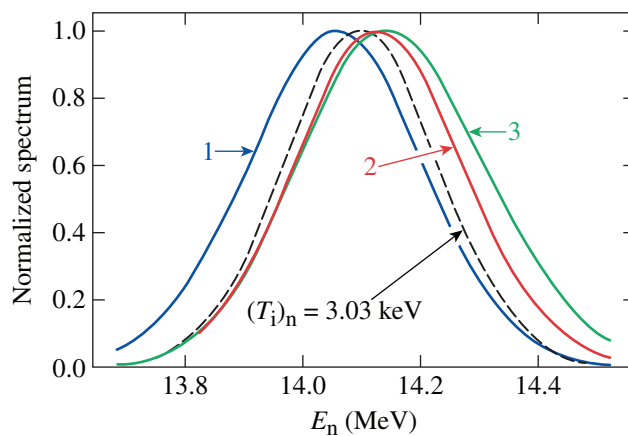
Figure 149.13

Simulated DT neutron spectra for shot 77066. The spectra in blue, red, and green (labeled 1, 2, and 3, respectively) were calculated for the three directions of OMEGA neutron diagnostics approximately indicated in Fig. 149.11(a) by the white dashed arrows (correspondingly labeled 1, 2, and 3). The hot-spot temperatures inferred from these spectra are 3.9, 3.5, and 4.4 keV, respectively. The black dashed line shows, for comparison, the Gaussian spectrum corresponding to $(T_i)_n = 3.03$ keV.

3.2±0.2, 3.8±0.2, and 3.6±0.2 keV, respectively. Figure 149.13 shows simulated neutron spectra for the same directions, which are denoted by the numbers 1, 2, and 3, respectively. Gaussian fits to these spectra reveal ion temperatures of 3.9, 3.5, and 4.4 keV, respectively. These temperatures are substantially larger than simulated $(T_i)_n = 3.03$ keV, indicating significant bulk motion effects in the hot spot of this implosion. A comparison of these measured and simulated temperatures shows disagreements in their directional distributions. For example, the minimum and maximum temperatures are measured in directions 1 and 2 ($T_i = 3.2±0.2$ and $3.8±0.2$ keV, respectively), whereas simulations show those temperatures in directions 2 and 3 ($T_i = 3.5$ and 4.4 keV, respectively). On the other hand,

of the hot-spot motion (in the direction $\theta \approx 50°$ and $\phi \approx 83°$) in directions 1 and 3, respectively [see Fig. 149.11(a)]. Direction 2 is more perpendicular to the hot-spot motion and has a relatively small, positive projection component. This explains the relatively small shift of the spectrum shown in red in Fig. 149.13.

The spectral shifts in directions 1 and 3 correspond to the neutron-averaged hot-spot velocity components $\tilde{v}_f \sim \Delta E \big/ \sqrt{2E_n m_n} \sim 70$ km/s. Correcting this estimate for an angle of ~50° between the hot-spot velocity and these directions [i.e., multiplying $\tilde{v}_f$ by a factor of ~1/cos(50°)], one obtains an estimate of neutron-averaged velocity of the hot spot, $v_f \sim 110$ km/s. Simulations have found that the local flow velocity in the hot spot can substantially vary, taking the maximum value of about a factor of 5 larger than v_f in the hottest, low-density part of the hot spot. This part produces relatively fewer neutrons, however, and, therefore, insignificantly contributes to v_f. The shown example demonstrates the importance of spectral-shift measurements to understanding conditions in hot spots.

Discussion and Conclusions

Three-dimensional hydrodynamic simulations using the code *ASTER* were conducted to investigate sources of large-scale asymmetries in room-temperature and cryogenic OMEGA implosions. Simulations of room-temperature implosions were focused on studying the effects of laser-induced nonuniformities caused by OMEGA beam overlap, target offset, and beam imbalance, mispointing, and mistiming. It was shown that simulations assuming measured sources of these nonuniformities reproduce the amplitude of modes 1 and 2 observed in experiments at an earlier implosion evolution (up to the end of the laser pulse). The development of modes 1 and 2 was studied using self-emission x-ray radiography in up to three viewing directions. The phases of mode 2, however, were not correctly predicted in simulations. The latter indicates that the measured nonuniformity sources assumed in simulations do not accurately represent the actual sources.

Significant mode-1 asymmetry was observed in room-temperature implosions near the bang time. These implosions used plastic-shell targets, in which the inner edge of the shell was doped with titanium to a depth of ~0.1 μm. These targets start producing Ti He$_\beta$ line emission from the fuel–ablator interface when the temperature there exceeds ~1 keV. This emission forms bright limbs on x-ray images. Measurements typically find mode-1 asymmetry of the limb brightening, and this asymmetry is well reproduced in simulations assuming measured sources of illumination nonuniformity. The limb asymmetry is attributed to distortions of the dense shell and

hot spot with dominant mode 1, which is induced by laser illumination nonuniformities. Simulations suggest that the brighter limb side is developed in the direction of the hot-spot motion caused by these distortions; however, simulations do not reproduce the measured directionality of the limb brightening. This, again, indicates that the nonuniformity sources assumed in simulations do not accurately represent the actual sources.

To study the effects of large-scale asymmetry on performance degradation of cryogenic implosions, 3-D simulations of cryogenic shot 77066 were performed assuming the best currently known sources of the asymmetry. These sources were quantified and include the above-mentioned laser-illumination nonuniformities and nonuniformities caused by the target offset and variation in ice-shell thickness (≈ 4 μm and ± 2 μm for mode 1, respectively). Simulations showed the development of dominant mode-1 asymmetry in the implosion shell at the time of maximum compression. This results in bulk motions in the hot spot with the neutron average velocity ~100 km/s in the direction that coincides with the direction of the mode-1 shell asymmetry. These motions result in a directional variation of the hot-spot temperature that is inferred from DT neutron spectra. The experimental and simulated temperatures show good agreement for the amplitude of this variation, but not for directionality of the maximum and minimum temperature measurements. The large-scale asymmetries result in a reduction of the simulated neutron yield to 39% of that of 1-D *ASTER* simulations, whereas the experimental yield shows 23% of the yield of *LILAC* simulations—a factor-of-about-2 overperformance in the simulation yields. This disagreement of the hot-spot temperature asymmetry in experiment and simulations suggests that it can be caused by an inaccuracy of the nonuniformity sources assumed in simulations.

Three-dimensional *ASTER* simulations of room-temperature and cryogenic OMEGA implosions show that large-scale asymmetries of the magnitudes observed in experiments can explain the measured performance degradation in mid- and high-adiabat implosions. Achieving better agreements between experiments and simulations will require a substantial improvement in the measurements of actual on-target nonuniformity sources that are assumed in simulations. In particular, current simulations assuming measured sources do not accurately reproduce directionality of low-mode perturbations (from modes 1 to 3), which limits the prediction capabilities of 3-D simulations.

A technique to correct the measured implosion shell asymmetry by modifying the power distribution of OMEGA

laser beams is under development. This technique uses a 3-D reconstruction of the shape of implosion shells with the help of self-emission x-ray radiography applied in several (three or more) viewing directions. Modifications of the beam-power distribution, which are based on *ASTER* predictions, will minimize the shell asymmetry and improve implosion performance.

The present study ignored the possibility that large-scale asymmetries in implosion shells can be affected by small-scale perturbations (with $\ell \gtrsim 50$) through mode coupling at the nonlinear stages of perturbation growth. The importance of this effect is unknown and will be studied in future works.

REFERENCES

1. T. R. Boehly, D. L. Brown, R. S. Craxton, R. L. Keck, J. P. Knauer, J. H. Kelly, T. J. Kessler, S. A. Kumpan, S. J. Loucks, S. A. Letzring, F. J. Marshall, R. L. McCrory, S. F. B. Morse, W. Seka, J. M. Soures, and C. P. Verdon, Opt. Commun. **133**, 495 (1997).

2. S. Atzeni and J. Meyer-ter-Vehn, *The Physics of Inertial Fusion: Beam Plasma Interaction, Hydrodynamics, Hot Dense Matter*, International Series of Monographs on Physics (Clarendon, Oxford, 2004).

3. E. I. Moses *et al.*, Phys. Plasmas **16**, 041006 (2009).

4. J. Delettrez, R. Epstein, M. C. Richardson, P. A. Jaanimagi, and B. L. Henke, Phys. Rev. A **36**, 3926 (1987).

5. V. N. Goncharov, S. P. Regan, E. M. Campbell, T. C. Sangster, P. B. Radha, J. F. Myatt, D. H. Froula, R. Betti, T. R. Boehly, J. A. Delettrez, D. H. Edgell, R. Epstein, C. J. Forrest, V. Yu. Glebov, D. R. Harding, S. X. Hu, I. V. Igumenshchev, F. J. Marshall, R. L. McCrory, D. T. Michel, W. Seka, A. Shvydky, C. Stoeckl, W. Theobald, and M. Gatu-Johnson, Plasma Phys. Control. Fusion **59**, 014008 (2017).

6. P. B. Radha, V. N. Goncharov, T. J. B. Collins, J. A. Delettrez, Y. Elbaz, V. Yu. Glebov, R. L. Keck, D. E. Keller, J. P. Knauer, J. A. Marozas, F. J. Marshall, P. W. McKenty, D. D. Meyerhofer, S. P. Regan, T. C. Sangster, D. Shvarts, S. Skupsky, Y. Srebro, R. P. J. Town, and C. Stoeckl, Phys. Plasmas **12**, 032702 (2005).

7. I. V. Igumenshchev, V. N. Goncharov, W. T. Shmayda, D. R. Harding, T. C. Sangster, and D. D. Meyerhofer, Phys. Plasmas **20**, 082703 (2013).

8. V. N. Goncharov, T. C. Sangster, R. Betti, T. R. Boehly, M. J. Bonino, T. J. B. Collins, R. S. Craxton, J. A. Delettrez, D. H. Edgell, R. Epstein, R. K. Follet, C. J. Forrest, D. H. Froula, V. Yu. Glebov, D. R. Harding, R. J. Henchen, S. X. Hu, I. V. Igumenshchev, R. Janezic, J. H. Kelly, T. J. Kessler, T. Z. Kosc, S. J. Loucks, J. A. Marozas, F. J. Marshall,

A. V. Maximov, R. L. McCrory, P. W. McKenty, D. D. Meyerhofer, D. T. Michel, J. F. Myatt, R. Nora, P. B. Radha, S. P. Regan, W. Seka, W. T. Shmayda, R. W. Short, A. Shvydky, S. Skupsky, C. Stoeckl, B. Yaakobi, J. A. Frenje, M. Gatu-Johnson, R. D. Petrasso, and D. T. Casey, Phys. Plasmas **21**, 056315 (2014).

9. I. V. Igumenshchev, F. J. Marshall, J. A. Marozas, V. A. Smalyuk, R. Epstein, V. N. Goncharov, T. J. B. Collins, T. C. Sangster, and S. Skupsky, Phys. Plasmas **16**, 082701 (2009).

10. G. I. Bell, Los Alamos National Laboratory, Los Alamos, NM, Report LA-1321 (1951); M. S. Plesset, J. Appl. Phys. **25**, 96 (1954).

11. I. V. Igumenshchev, V. N. Goncharov, F. J. Marshall, J. P. Knauer, E. M. Campbell, C. J. Forrest, D. H. Froula, V. Yu. Glebov, R. L. McCrory, S. P. Regan, T. C. Sangster, S. Skupsky, and C. Stoeckl, Phys. Plasmas **23**, 052702 (2016).

12. P. B. Radha, T. J. B. Collins, J. A. Delettrez, Y. Elbaz, R. Epstein, V. Yu. Glebov, V. N. Goncharov, R. L. Keck, J. P. Knauer, J. A. Marozas, F. J. Marshall, R. L. McCrory, P. W. McKenty, D. D. Meyerhofer, S. P. Regan, T. C. Sangster, W. Seka, D. Shvarts, S. Skupsky, Y. Srebro, and C. Stoeckl, Phys. Plasmas **12**, 056307 (2005).

13. P. Colella and P. R. Woodward, J. Comput. Phys. **54**, 174 (1984).

14. I. V. Igumenshchev, D. H. Edgell, V. N. Goncharov, J. A. Delettrez, A. V. Maximov, J. F. Myatt, W. Seka, A. Shvydky, S. Skupsky, and C. Stoeckl, Phys. Plasmas **17**, 122708 (2010).

15. L. Spitzer, Jr. and R. Härm, Phys. Rev. **89**, 977 (1953).

16. D. Mihalas and B. Weibel-Mihalas, *Foundations of Radiation Hydrodynamics* (Oxford University Press, New York, 1984).

17. W. L. Briggs, V. E. Henson, and S. F. McCormick, *A Multigrid Tutorial*, 2nd ed. (Society for Industrial and Applied Mathematics, Philadelphia, 2000).

18. S. Buckeridge and R. Scheichl, Numer. Linear Algebr **17**, 325 (2010).

19. F. J. Marshall, J. A. Delettrez, R. Epstein, R. Forties, R. L. Keck, J. H. Kelly, P. W. McKenty, S. P. Regan, and L. J. Waxer, Phys. Plasmas **11**, 251 (2004); R. A. Forties and F. J. Marshall, Rev. Sci. Instrum. **76**, 073505 (2005).

20. W. Grimble, F. J. Marshall, and E. Lambrides, "Measurement of Cryogenic Implosion Core Offsets in OMEGA's Inertial Confinement Fusion Experiments," to be submitted to Review of Scientific Instruments.

21. D. T. Michel, C. Sorce, R. Epstein, N. Whiting, I. V. Igumenshchev, R. Jungquist, and D. H. Froula, Rev. Sci. Instrum. **83**, 10E530 (2012).

22. R. C. Shah, B. M. Haines, F. J. Wysocki, J. F. Benage, J. Fooks, V. Glebov, P. Hakel, M. Hoppe, I. V. Igumenshchev, G. Kagan, R. C. Mancini, F. J. Marshall, D. T. Michel, T. J. Murphy, M. E. Schoff, C. Stoeckl, and B. Yaakobi, "Systematic Fuel Cavity Asymmetries in Directly Driven ICF Implosions," to be published in Physical Review Letters.

23. D. T. Michel, A. K. Davis, W. Armstrong, R. Bahr, R. Epstein, V. N. Goncharov, M. Hohenberger, I. V. Igumenshchev, R. Jungquist, D. D. Meyerhofer, P. B. Radha, T. C. Sangster, C. Sorce, and D. H. Froula, High Power Laser Science and Engineering **3**, e19 (2015).

24. S. P. Regan, V. N. Goncharov, I. V. Igumenshchev, T. C. Sangster, R. Betti, A. Bose, T. R. Boehly, M. J. Bonino, E. M. Campbell, D. Cao, T. J. B. Collins, R. S. Craxton, A. K. Davis, J. A. Delettrez, D. H. Edgell, R. Epstein, C. J. Forrest, J. A. Frenje, D. H. Froula, M. Gatu Johnson, V. Yu. Glebov, D. R. Harding, M. Hohenberger, S. X. Hu, D. Jacobs-Perkins, R. T. Janezic, M. Karasik, R. L. Keck, J. H. Kelly, T. J. Kessler, J. P. Knauer, T. Z. Kosc, S. J. Loucks, J. A. Marozas, F. J. Marshall, R. L. McCrory, P. W. McKenty, D. D. Meyerhofer, D. T. Michel, J. F. Myatt, S. P. Obenschain, R. D. Petrasso, R. B. Radha, B. Rice, M. Rosenberg, A. J. Schmitt, M. J. Schmitt, W. Seka, W. T. Shmayda, M. J. Shoup III, A. Shvydky, S. Skupsky, S. Solodov, C. Stoeckl, W. Theobald, J. Ulreich, M. D. Wittman, K. M. Woo, B.Yaakobi, and J. D. Zuegel, Phys. Rev. Lett. **117**, 025001 (2016); **117**, 059903(E) (2016).

25. V. N. Goncharov, T. C. Sangster, P. B. Radha, R. Betti, T. R. Boehly, T. J. B. Collins, R. S. Craxton, J. A. Delettrez, R. Epstein, V. Yu. Glebov, S. X. Hu, I. V. Igumenshchev, J. P. Knauer, S. J. Loucks, J. A. Marozas, F. J. Marshall, R. L. McCrory, P. W. McKenty, D. D. Meyerhofer, S. P. Regan, W. Seka, S. Skupsky, V. A. Smalyuk, J. M. Soures, C. Stoeckl, D. Shvarts, J. A. Frenje, R. D. Petrasso, C. K. Li, F. Séguin, W. Manheimer, and D. G. Colombant, Phys. Plasmas **15**, 056310 (2008).

26. M. Gatu Johnson, J. A. Frenje, D. T. Casey, C. K. Li, F. H. Seguin, R. Petrasso, R. Ashabranner, R. M. Bionta, D. L. Bleuel, E. J. Bond, J. A. Caggiano, A. Carpenter, C. J. Cerjan, T. J. Clancy, T. Doeppner, M. J. Eckart, M. J. Edwards, S. Friedrich, S. H. Glenzer, S. W. Haan, E. P. Hartouni, R. Hatarik, S. P. Hatchett, O. S. Jones, G. Kyrala, S. Le Pape, R. A. Lerche, O. L. Landen, T. Ma, A. J. MacKinnon, M. A. McKernan, M. J. Moran, E. Moses, D. H. Munro, J. McNaney, H. S. Park, J. Ralph, B. Remington, J. R. Rygg, S. M. Sepke, V. Smalyuk, B. Spears, P. T. Springer, C. B. Yeamans, M. Farrell, D. Jasion, J. D. Kilkenny, A. Nikroo, R. Paguio, J. P. Knauer, V. Yu. Glebov, T. C. Sangster, R. Betti, C. Stoeckl, J. Magoon, M. J. Shoup III, G. P. Grim, J. Kline, G. L. Morgan, T. J. Murphy, R. J. Leeper, C. L. Ruiz, G. W. Cooper, and A. J. Nelson, Rev. Sci. Instrum. **83**, 10D308 (2012).

First-Principles Equation-of-State Table of Silicon and Its Effects on High-Energy-Density Plasma Simulations

Introduction

As one of the most-abundant elements on Earth, silicon is important to many different fields ranging from the semiconductor industry,[1] geophysics,[2] photovoltaics,[3] planetary and astrophysics,[4–6] to inertial confinement fusion (ICF) physics studies.[7–9] For ICF applications, silicon has been used as a dopant to ablators in indirect-drive ICF target designs.[10] It has also been applied to mitigate laser-imprint effects[11,12] and the two-plasmon–decay instability[13,14] for multilayer target designs in direct-drive ICF implosions.[15] For these high-energy-density (HED) applications, it is essential to know the properties of silicon under extreme conditions. The equation of state (EOS) of silicon is one of such intrinsic properties that are crucial to both ICF and geophysics applications since it is needed for hydrodynamic simulations of ICF implosions and for understanding the geophysics of the earth's outer core.[2]

The EOS studies of silicon under megabar (Mbar) pressures began in the 1960s (Ref. 16) using explosive drive. The principal Hugoniot measurements of silicon were continued in the 1970s and 1980s by different groups.[17,18] Many surprises were found in our understanding of the behavior of shocks in silicon. For instance, the elastic behavior of shocks was observed in silicon even at Mbar pressures.[19] Namely, the lattice reduction related to shock compression may occur only along the shock-propagation direction, instead of hydrostatical lattice-shrinking in all three dimensions. Furthermore, the measured optical emission from shocked silicon was found to be much lower than expected, which has been hypothesized to be caused by the unusually long electron–ion equilibration time in shocked silicon.[20–22] These abnormal phenomena have been observed in shock experiments up to ~6-Mbar pressures. What might occur for silicon pressures >10 Mbar remains to be seen. To the best of our knowledge, these anomalies observed in shocked silicon are not fully understood. To this end, a thorough understanding of silicon properties under HED conditions is necessary.

Theoretical investigations on shock compressions of silicon have been performed by classical molecular-dynamics methods,[23–25] quantum molecular dynamics simulations based on the density functional theory (DFT),[26–29] and path-integral Monte Carlo (PIMC) modeling.[27,29] Most of these studies have been devoted to the moderate-pressure regime of $P < 2$ Mbar, while the two most-recent first-principles calculations[27,29] extended the Hugoniot pressures from ~1 Mbar to over ~10 Gbar for the first time. These calculations combined the orbital-based–DFT Kohn–Sham molecular-dynamics (KSMD) method, the orbital-free–DFT molecular-dynamics (OFMD) method, and the PIMC simulation. All three first-principles calculations are in good agreement in predicting the principal Hugoniot of silicon, which was found to be ~20% softer than both the extensively used *SESAME*-EOS model[30] (Table 3810) and the quotidian equation-of-state (QEOS) model.[31] The predicted softening of silicon should have important implications for HED simulations of silicon plasmas. However, those calculations are concerned with only the plasma conditions along the principal Hugoniot. To study how such a softening behavior of silicon affects HED plasma simulations, we must expand our first-principles calculations to cover a wide range of off-Hugoniot plasma conditions.

In this article, we calculated the EOS for a wide range of silicon plasma conditions by using DFT-based molecular-dynamics simulations. To be specific, we have sampled silicon densities from $\rho = 0.001$ g/cm^3 to $\rho = 500$ g/cm^3 and temperatures from $T = 2000$ K to $T = 10^8$ K. Based on these *ab-initio* calculations, we have built a first-principles equation-of-state (FPEOS) table of silicon for ICF and HED applications. For off-Hugoniot conditions, we have investigated the differences in pressure and internal energy between FPEOS and *SESAME* EOS. Implementing the FPEOS table of silicon into the one-dimensional (1-D) hydrocode *LILAC*[32] and two-dimensional (2-D) hydrocode *DRACO*, we have tested its effects on HED plasma simulations of ICF implosions using a Si ablator. Comparisons with traditional *SESAME*-EOS simulations illustrated the need for more-accurate EOS tables to precisely design ICF and HED experiments.

The following sections: (1) describe the details of our first-principles calculations; (2) compare the FPEOS and *SESAME*

EOS for different isochoric plasma conditions (for complete-ness, the principal Hugoniot comparison is included, even though it has been reported elsewhere[29]); (3) present the effects of the FPEOS table on HED plasmas through *LILAC* simula-tions of ICF implosions using a silicon layer as the ablator; and (4) present our conclusions.

Molecular-Dynamics Simulations
Based on the Density Functional Theory

First-principles methods, such as DFT-based quantum molecular dynamics (QMD),[33–36] path-integral Monte Carlo,[37] and quantum Monte Carlo (QMC),[38,39] have been developed over the past decades to understand the properties of materi-als under extreme conditions. Two different versions of QMD have been implemented by the condensed-matter and HED physics communities. One uses the orbital-based Kohn–Sham formalism[40] with the finite-temperature density functional theory, in conjunction with the molecular-dynamics method for ion motion. The other is the orbital-free molecular-dynamics method,[41] which is based on the original DFT idea that the free energy of a many-electron system can be written as a function solely depending on the electron density. For most cases, the KSMD method has been proven to be an accurate and efficient method for calculating material properties under high com-pression at temperatures generally below the electron Fermi temperature T_F. It becomes impractical for high-temperature ($T > T_F$) simulations because thermal excitation of electrons requires a large number of orbitals for convergence. The OFMD method is a natural extension of the KSMD method for high-T material simulations, even though it is not as accurate as KSMD. Nevertheless, the pressure difference between KSMD and OFMD calculations is still within ~1% in the overlapping regime of $T \sim T_F$ (valid for both methods), which is acceptable for general ICF/HED applications.

We have used the Vienna *ab initio* Simulation Package (VASP)[42–44] for KSMD simulations, in which electrons are treated quantum mechanically with a plane-wave finite-temper-ature DFT description. The electrons and ions of the material are in thermodynamic equilibrium with equal temperature ($T_e = T_i$). The electron–ion Coulomb interaction is represented by a projector augmented-wave (PAW) pseudopotential with "frozen" 1*s*-core electrons. The electron exchange-correlation potential is described by the generalized-gradient approxi-mation (GGA) with the Perdew–Burke–Ernzerhof (PBE) functional.[45] Under the Born–Oppenheimer approximation, the self-consistent electron density is first determined for an ion configuration. Then, the classical ions are moved by the combined electronic and ionic forces, using Newton's equation.

This molecular-dynamics procedure is repeated for thousands of time steps from which the thermodynamic EOS quantities such as pressure and internal energy can be directly calculated.

In our KSMD simulations, we have employed the Γ point (**k** = 0) sampling of the Brillouin zone. We used either 32 or 64 Si atoms (depending on density) in a cubic cell with a peri-odic boundary condition. The cubic cell size is determined from the mass density. The PAW potential of Si included 12 active electrons; the plane-wave cutoff energy was set to 2000 eV. In all KSMD simulations, a sufficient number of bands (varying from 500 to 4100) were included such that the occupation of the highest band was less than 10^{-5}. The time step varied from $\delta t = 1.5$ fs to $\delta t = 0.085$ fs, respectively, for the lowest and highest densities ($\rho_{min} = 0.1$ g/cm^3 and $\rho_{max} = 50$ g/cm^3). Good convergence was obtained for these parameter sets. The sampled temperature points varied from $T = 2000$ K to a maximum temperature of $T = 500,000$ K. Outside these density and temperature ranges, we switched to the OFMD calculations since the 1*s*-core electrons must be included in the EOS calculations.

The OFMD method[41] originated from the true spirit of the Hohenberg–Kohn theorem,[46] i.e., the free energy of an elec-tron–ion system at any ion configuration can be written as a function of the electron density. The kinetic energy of the elec-trons is currently represented by the Thomas–Fermi functional plus the von Weizsäcker correction that takes into account the gradient of electron density. These terms were obtained from the semiclassical expansion of the partition function up to the first order. In OFMD simulations, all electrons, both bound and free, are treated equally. The divergence of the electron-nucleus potential is regularized for each thermodynamic condition through a similar procedure of generating the norm-conserving pseudopotential as the PAW treatment. The cutoff radius is chosen to be less than 10% of the Wigner–Seitz radius to avoid an overlap of regularized ion spheres. The exchange-correlation function is expressed in the local density approximation of Perdew and Zunger.[47]

At each time step of an OFMD simulation, the electron free energy for an ionic configuration is first minimized in terms of the local electron density. Then, the classical ions are moved by the combined electronic and ionic forces, the same as in the KSMD procedure. In our OFMD simulations of sili-con plasmas, we used 128 atoms in a cubic cell with periodic boundary conditions. The time step varied from $\delta t = 0.144$ fs to $\delta t = 6 \times 10^{-5}$ fs, respectively, for the lowest-density/lowest-temperature ($\rho = 0.001$ g/cm^3 and $T = 125,000$ K) point and

the highest-density/highest-temperature (ρ = 500 g/cm^3 and $T = 10^8$ K) point. Finally, the thermodynamic EOS quantities were statistically evaluated from the molecular-dynamics (MD) propagation of the system (5000 to 100,000 steps, depending on the density).

For each isochoric curve, we examined the EOS quantities for the overlapping temperature points between the KSMD and OFMD calculations. We made the transition from KSMD to OFMD at the temperature point where their differences were the smallest (within ~1%). Carrying out these calculations for a wide range of silicon plasma conditions, we obtained both pressure and internal energies for all the sampled density and temperature points (ρ = 0.001 to 500 g/cm^3 and T = 2000 to 10^8 K). As an example, in Fig. 149.14 we plot the total pressures as a function of the silicon plasma temperature for each of the sampled isochoric curves.
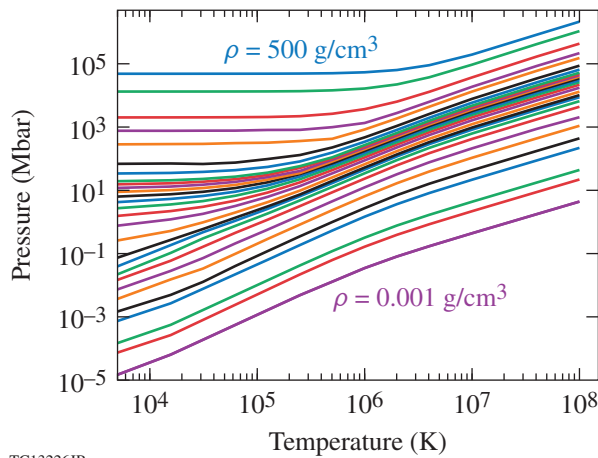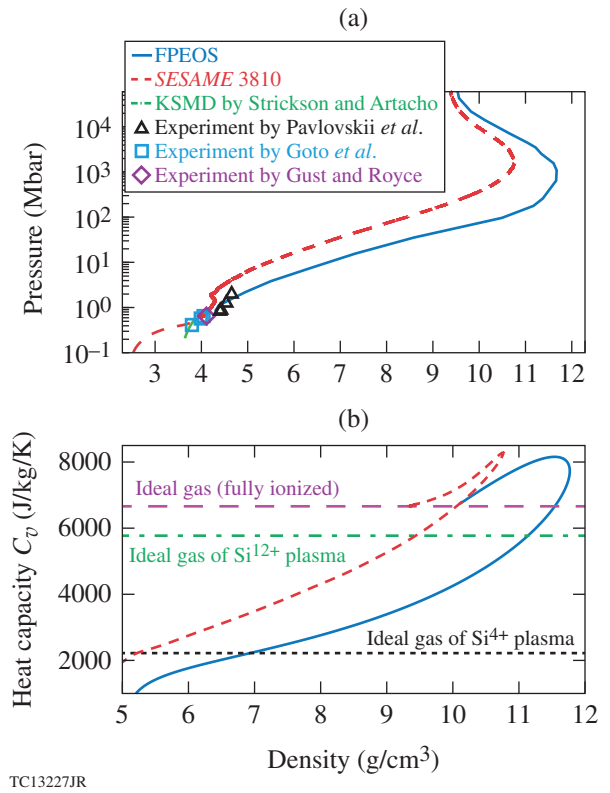

Figure 149.14
Silicon pressure as a function of temperature for all densities (ρ = 0.001 to 500 g/cm^3) scanned by our first-principles (KSMD + OFMD) calculations.

Comparison Between FPEOS and *SESAME* EOS

From the FPEOS table, we can derive the principal Hugoniot curve for silicon shocks by using the Rankine–Hugoniot equation. The initial state is chosen to be solid silicon (ρ_0 = 2.329 g/cm^3) in its diamond phase at ambient pressure (P_0 = 1 bar). We compare the FPEOS Hugoniot with the one derived from the extensively used *SESAME*-EOS model (*SESAME* 3810 table) in Fig. 149.15(a), in which the Hugoniot pressure spanning more than five orders of magnitude is plotted as a function of the shock density. The *SESAME*-EOS model was based on the chemical picture of matter, meaning that the total free energy can be decomposed into the cold curve, the ionic excitation, and the electron thermal excitation. It was typically

Figure 149.15
(a) The shock Hugoniot of silicon predicted by FPEOS (solid blue line) is compared to the EOS-model *SESAME* 3810 (dashed red line), a recent KSMD study (dashed green line),[28] and available experiments (various symbols) by Pavlovskii *et al.*,[16] Gust and Royce,[17] and Goto *et al.*[18] (b) A comparison of heat capacity calculated from FPEOS and *SESAME* 3810 along the principal Hugoniot. Diamond-phase silicon (ρ_0 = 2.329 g/cm^3) is chosen as the initial state for the Hugoniot calculations.

constructed (constrained) by the best-available experimental data (typically limited). Specifically, for *SESAME* 3810 (Si) constructed in 1997, the EOS below the solid–liquid phase transition was based on experimental Hugoniot data.[16–18] For conditions above the liquid phase transition, the EOS was constructed such that the shock Hugoniot was "similar" to germanium (*SESAME* 3950) up to 4.4 Mbar. The ion thermal contribution is based on a Debye model with a correction for the liquid's specific heat beyond the melt temperature.[48] The correction also ensures that in the high-temperature limit, the proper model (ideal gas) that is recovered will give a shock Hugoniot compression ratio $\rho/\rho_0 = 4$. The Hugoniot comparison in Fig. 149.15(a) indicates that under shock compression, silicon is much softer than predicts by the traditional chemical picture of materials.[29] For example, at a constant pressure of ~20 Mbar, the *SESAME* 3810 table predicts a shock density of $\rho \simeq 6.3$ g/cm^3, while the FPEOS table gives a much-higher

shock density of $\rho \simeq 7.7$ g/cm^3. Namely, the FPEOS table predicts that silicon under 10- to 1000-Mbar pressures is ~20% softer than *SESAME* 3810. For the same shock density at $\rho = 8$ g/cm^3, the *SESAME* 3810 model predicts a shock pressure of $P \simeq 73.4$ Mbar, which is more than 3× higher than the FPEOS case ($P \simeq 24$ Mbar). Figure 149.15(a) indicates that the maximum compression (ρ/ρ_0) changes from the *SESAME*-predicted value of ~4.6 to 5.0 in FPEOS. Finally, in the same figure, we have plotted the existing experimental data,[16–18] which are represented by the different symbols. These Hugoniot data were obtained from explosively driven shock experiments. To the best of our knowledge, no published data exist for laser-shock Hugoniot measurements in pressures above 10 Mbar. The opacity of Si for most velocity interferometer system for any reflector (VISAR) laser wavelengths[49] is one of the hurdles for accurate shock measurements in silicon. Nevertheless, it is shown in Fig. 149.15 that the explosively driven shock data up to ~2 Mbar agree well with our calculations, which seems also to indicate the softening of silicon under compression. It is noted that at the measured highest shock density of $\rho =$ 4.6 g/cm^3, the *SESAME*-EOS–predicted pressure is at least 2× higher than the experimental value of $P \simeq 2$ Mbar.

To further examine the properties of shocked silicon, we have calculated the heat capacity C_v along its principal Hugoniot. Because C_v is a measure of the energy change with respect to temperature at a fixed volume, it can give some indication of how rapidly the entropy is increasing with temperature in a silicon shock. The obtained C_v results are plotted in Fig. 149.15(b) as a function of the Hugoniot density for both *SESAME* 3810 (dashed red line) and FPEOS (solid blue line). In Fig. 149.15(b), we also plot three horizontal lines to indicate the expected heat capacities for ideal-gas plasmas of three different ionization stages of Si^{4+}, Si^{12+}, and Si^{14+}, respectively. For instance, the lowest dashed black line represents the ideal-gas plasma that includes only Si^{4+} and free electrons without any interactions. Since the electron ionization process acts like a "heat sink" for the system, one expects the heat capacity to increase during the ionization of bound electrons. This is especially true for the innermost shell electrons because of the large energy gaps between the L-shell and K-shell electrons. This is exactly what can be seen in Fig. 149.15(b), where the FPEOS calculation (solid blue line) gives a peak of C_v near the peak compression at $\rho \simeq 11.5$ g/cm^3 [see Fig. 149.15(a)]. After the 1s-electron ionization is completed, the heat capacity approaches the ideal-gas limit (horizontal dashed pink line) as a fully ionized Si plasma is formed. The *SESAME* 3810–predicted C_v has a similar trend, but the same value of C_v is reached at a smaller density. In other words, at the same density the FPEOS-predicted C_v is ~50%

lower than the *SESAME* 3810 case, meaning that less entropy increase is expected in FPEOS. By referring to the ideal-gas C_v, one can argue that the same ionization stage is first reached at much-lower densities in *SESAME* 3810 than in FPEOS. Again, all of these features are consistent with the higher compressibility of silicon predicted by FPEOS.

Next, we compare the pressure and internal energy of silicon plasmas for off-Hugoniot conditions between FPEOS (solid blue line) and *SESAME* 3810 (dashed red line) in Figs. 149.16–149.18. Figures 149.16(a) and 149.17(a) show the pressure as a function of plasma temperature, respectively, for silicon densities of $\rho = 5$ g/cm^3 and $\rho = 10$ g/cm^3, while the internal energy comparisons are made in Figs. 149.16(b) and 149.17(b). One sees in Fig. 149.16(a) that the *SESAME* pressure is ~10% lower than FPEOS for temperatures $T < 10^4$ K, but it
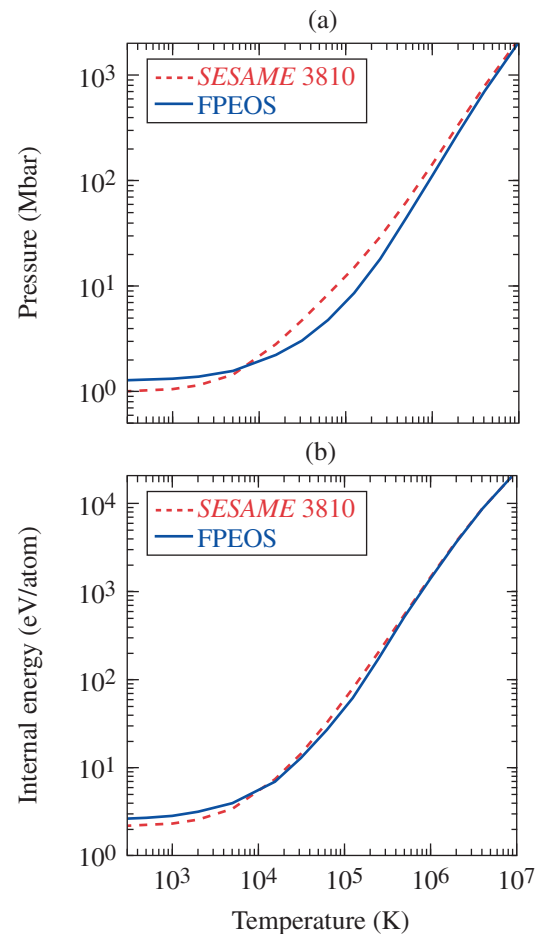

TC13228JR

Figure 149.16
The off-Hugoniot equation-of-state comparisons between FPEOS and *SESAME* 3810. The (a) pressures and (b) internal energies are plotted as functions of temperature for a silicon density of $\rho = 5$ g/cm^3.

reverses for $10^4 < T < 10^6$ K with a "crossover" temperature at $T \sim 10^4$ K (~1 eV). The pressure difference between FPEOS and *SESAME* 3810 reaches a maximum of ~50% in the warm dense regime ($T \sim 10^5$ K) at this density ($\rho = 5$ g/cm^3). This is the regime in which both electron degeneracy and strong ion–ion coupling play significant roles in determining the EOS. The internal energy comparison in Fig. 149.16(b) shows a similar trend, although the difference is only ~20%. For high temperatures of $T > 10^6$ K, both FPEOS and *SESAME* 3810 are in good agreement with each other as the two EOS tables correctly approach the ideal gas limit. Figure 149.17 shows similar EOS comparisons for $\rho = 10$ g/cm^3. At this higher density note that the crossover temperature now moves to near

~10^5 K (~10 eV), and the maximum difference in pressure between FPEOS and *SESAME* 3810 reduces to ~20%. The difference in internal energy in Fig. 149.17(b) is also reduced when compared to Fig. 149.16(b).

Finally, we explore two other isochores at high densities of $\rho = 50$ g/cm^3 and $\rho = 500$ g/cm^3, respectively, in Figs. 149.18(a) and 149.18(b). Again, the two panels compare the pressures of FPEOS with *SESAME* 3810 at various temperatures. Figure 149.18(b) indicates that both FPEOS and *SESAME* 3810 are very close to each other at this high density of $\rho = 500$ g/cm^3, even though *SESAME* 3810 gives a slightly higher pressure over the entire temperature range (no more crossover is seen between
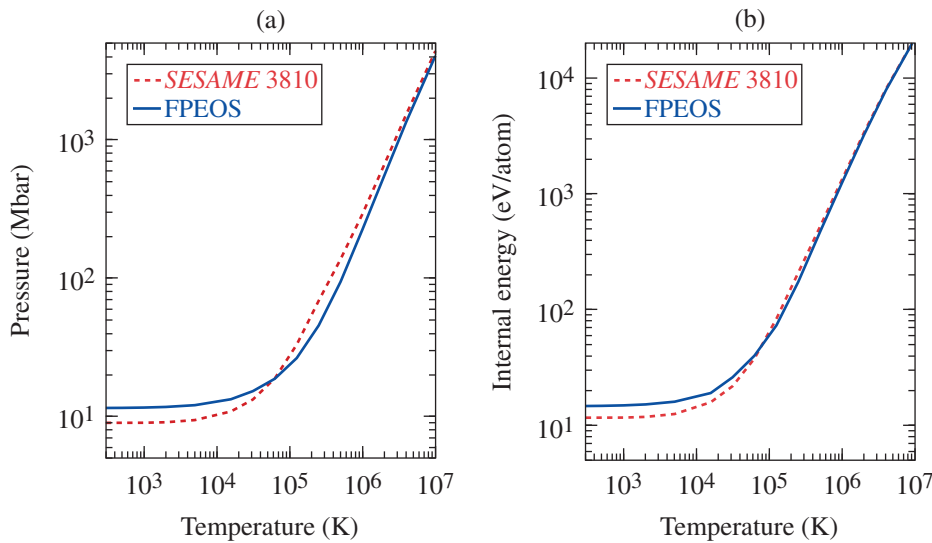

TC13229JR

Figure 149.17
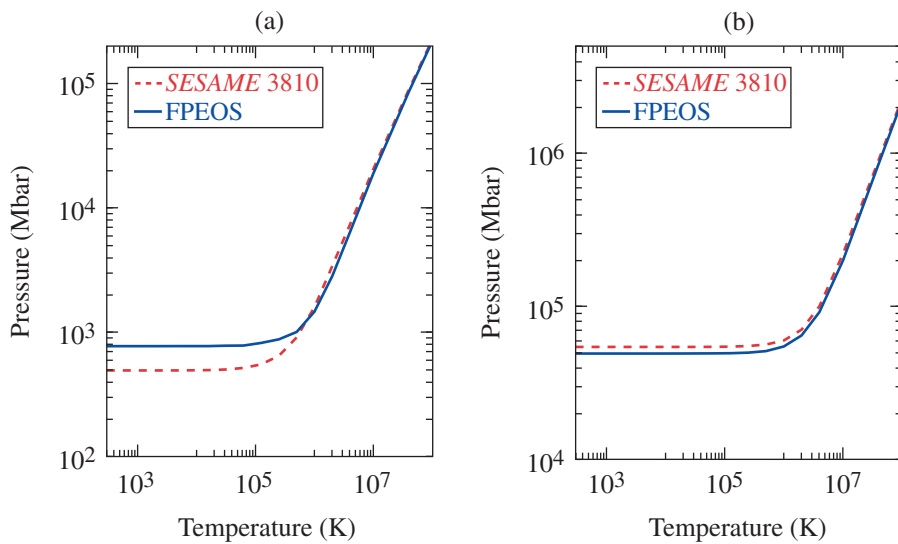Same as Fig. 149.16 except for a silicon density of $\rho = 10$ g/cm^3.

TC13230JR

Figure 149.18
Pressure comparisons between FPEOS and *SESAME* 3810 for higher densities of silicon plasmas: (a) $\rho = 50$ g/cm^3 and (b) $\rho = 500$ g/cm^3.
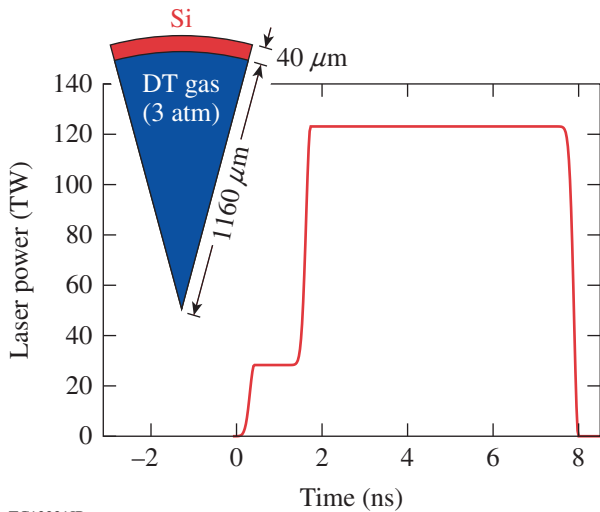
the two EOS's). Both EOS tables are in better agreement with each other in this electron-degeneracy–dominated regime. For the intermediate density of $\rho = 50$ g/cm^3, Fig. 149.18(a) still shows a trend similar to the one seen in Figs. 149.16 and 149.17. Namely, the *SESAME* 3810 model still underestimates the pressure for the low-T regime ($T < 10^6$ K). With these large EOS differences identified in both on-Hugoniot and off-Hugoniot warm-dense-plasma conditions, we expect to see significant effects on HED plasma simulations between using the newly established FPEOS and using the *SESAME* 3810 for silicon.

EOS Effects on HED Plasma Simulations Involving Silicon

To examine the EOS effects on HED plasma simulations, we have implemented our FPEOS table of silicon into our radiation–hydrodynamics codes *LILAC* and *DRACO*. We have extrapolated our EOS results for temperatures outside our calculation range (2000 K to 10^8 K). With the implementation of the FPEOS table, we can investigate its effects on HED simulations involving silicon plasmas. Since in an ICF implosion the capsule generally undergoes a path sweeping through many different density and temperature conditions, integrated ICF implosion simulations would be more suitable for examining EOS effects. As an example, we consider a NIF (National Ignition Facility)-type direct-drive implosion with the target and pulse shape shown in Fig. 149.19. The $\phi =$ 2.4-mm capsule is made of a 40-μm Si layer filled with 3 atm of deuterium–tritium (DT) gas. The step laser pulse has a total

energy of 800 kJ, with a duration of 8 ns. Figures 149.20–149.23 show the *LILAC* simulation results using either FPEOS (solid blue line) or *SESAME* 3810 (dashed red line) for silicon. Both simulations used the same nonlocal thermal-transport model[50] and inverse-bremsstrahlung absorption with cross-beam energy transfer modeling.[51] For DT gas, the two simulations used the same FPEOS table[52,53] and the same first-principles opacity table[54] of DT, so that the EOS tests solely focused on the silicon ablator layer. In Fig. 149.20, we plot the density and temperature profile snapshot at $t = 0.9$ ns as a function of target radius for the two simulations. At this time, the shock is still propagating inside the Si layer (the shock front is located at $R \sim 1180$ μm). Figure 149.20 indicates that (1) the shock density in FPEOS is ~20% higher than the *SESAME* simulation and (2) the shock in the *SESAME* simulation is ahead of the FPEOS case, giving a shock-speed difference of ~10%. These features can be understood by considering the softening of silicon shock in FPEOS (see Fig. 149.15). Namely, the identical laser drive gives the same ablation pressure in the two simulations; for the same shock pressure (P_s), the FPEOS simulation will give ~20%-higher shock density (ρ_s) as the Hugoniot curve seen in Fig. 149.15(a). Since the shock speed depends on the shock density through $V_s = \sqrt{P_s / \rho_0} / \sqrt{1 - \rho_0 / \rho_s}$, one can see that for the same P_s, the ~20%-higher shock density in FPEOS will give an ~10%-smaller shock speed than the *SESAME* case. Figure 149.20 also indicates that the shock temperature is ~20% higher in FPEOS.
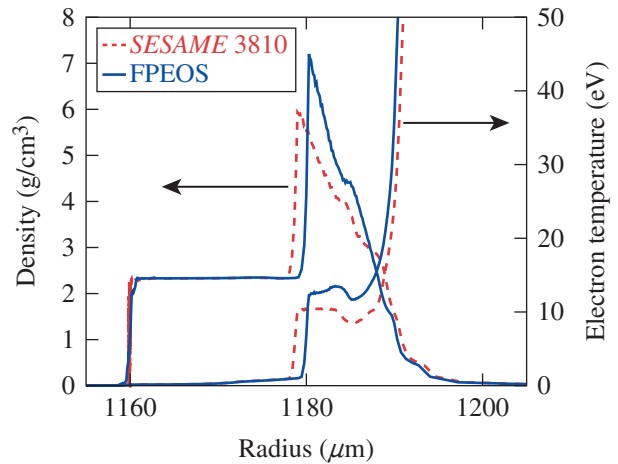

TC13231JR

Figure 149.19
The laser pulse shape and target dimensions for implosion simulations to test the silicon EOS effects. The capsule consists of a 40-μm-thick silicon shell ($\rho_0 = 2.329$ g/cm^3) filled with 3 atm of DT gas. The initial target radius $R = 1200$ μm. The total laser energy is 800 kJ with an 8-ns pulse duration, available at the National Ignition Facility.

TC13232JR

Figure 149.20
Comparisons of density and electron temperature profiles predicted by the two *LILAC* simulations using FPEOS (solid blue lines) and *SESAME* 3810 (dashed red lines) EOS models. The snapshot was taken at $t = 0.9$ ns, when the first shock was still propagating in the silicon layer.
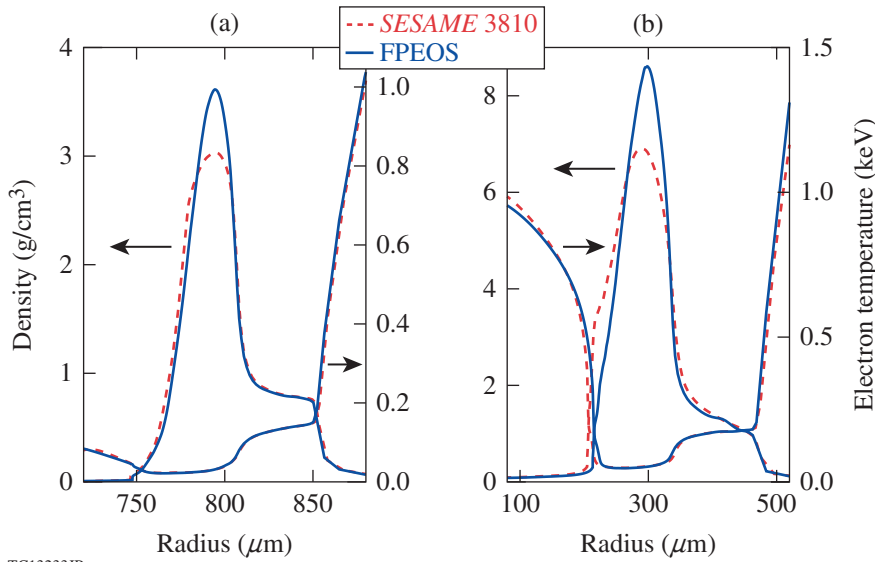
Figure 149.21
Same as Fig. 149.20 but for different implosion times: (a) $t = 5.4$ ns (in flight of the imploding shell) and (b) $t = 7.9$ ns (the end of shell acceleration).

TC13233JR
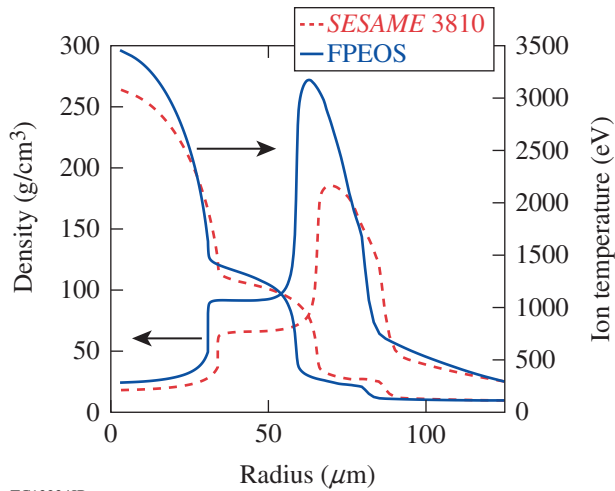
TC13234JR

Figure 149.22
Comparisons of density and ion temperature profiles predicted by the two *LILAC* simulations using FPEOS (solid blue lines) and *SESAME* 3810 (dashed red line) EOS models. Peak neutron production is at $t \sim 9.0$ ns.

As the implosion proceeds, Fig. 149.21 shows the density and temperature profiles during the in-flight stage of $t = 5.4$ ns [Fig. 149.21(a)] and at the end of acceleration of $t = 7.9$ ns [Fig. 149.21(b)]. One sees from Fig. 149.21 that the peak density of the shell from the FPEOS simulation is always ~20% higher than the *SESAME* 3810 case. This can be attributed to the greater compressibility of silicon predicted by FPEOS. Except for the difference in peak density, the two simulations give very similar density and temperature profiles for the imploding shell. Some difference in the back surface of the shell appears only at the end of the acceleration phase, as indicated by Fig. 149.21(b). Note that the coronal plasma conditions are also very similar
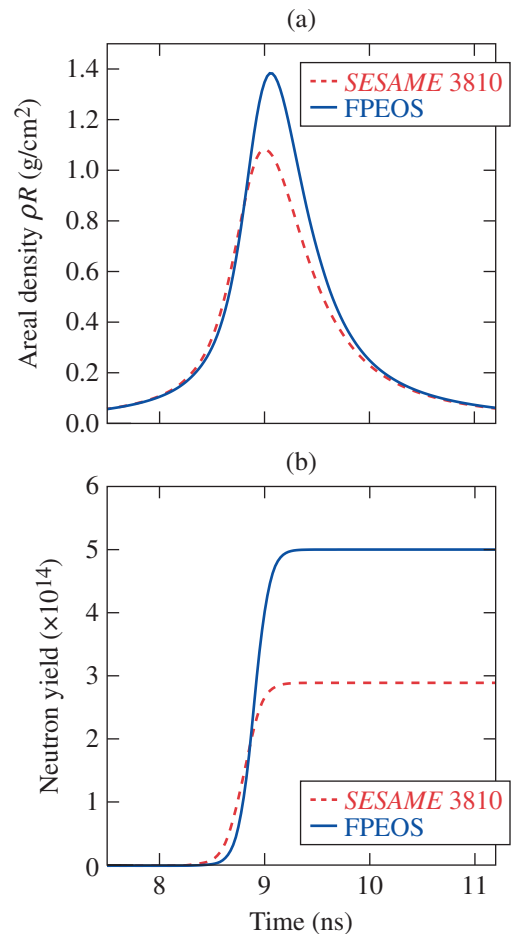
TC13235JR

Figure 149.23
Comparisons of (a) the areal density ρR and (b) the total neutron yield as functions of time for the two *LILAC* simulations using FPEOS (solid blue lines) and *SESAME* 3810 (dashed red line) EOS models.

in the two cases, as the EOS difference becomes very small at high temperatures of $T > 10^6$ K. Figure 149.21 also shows an interesting double-ablation-front feature, which can develop in such mid-Z–ablator implosions[55] because of the significant radiation preheat from coronal emissions. The ~20% difference in peak density in the two simulations can have significant consequences when the imploding shell stagnates. Figure 149.22 displays the situation at the time of peak neutron production (near peak compression). Again, the figure shows the density and ion temperature as functions of the target radius. The maximum density reached in the FPEOS simulation is $\rho_p = 271.9$ g/cm^3, in contrast to the *SESAME* 3810–predicted $\rho_p = 185.5$ g/cm^3. The Si shell is converged slightly more in FPEOS than *SESAME*, resulting in a somewhat different hot-spot radius ($R_{hs} = 30.5$ μm versus $R_{hs} = 33.6$ μm). Consequently, the maximum ion temperature is increased from $T_i \simeq 3.07$ keV (*SESAME*) to $T_i \simeq 3.45$ keV (FPEOS).

Finally, we plot the history of the compression areal density (ρR) and neutron yield, respectively, in Figs. 149.23(a) and 149.23(b) for the two implosion simulations. One sees from Fig. 149.23(a) that the peak areal density reaches a value of $\rho R = 1.38$ g/cm^2 in FPEOS, which is ~30% higher than the *SESAME* simulation. The total neutron yield predicted by FPEOS, shown by Fig. 149.23(b), is increased by more than ~70% with respect to the *SESAME* case [$Y = 5.0 \times 10^{14}$ (FPEOS) versus $Y = 2.9 \times 10^{14}$ (*SESAME*)]. As a result, the EOS difference can have significant consequences on predicting the 1-D target performance. This illustrates the importance of having a more-accurate EOS table to the 1-D hydrodynamic designs of ICF/HED experiments.

Conclusion

We have applied DFT-based molecular-dynamics simulation methods to investigate the EOS of silicon, spanning a wide range of plasma conditions from $\rho = 0.001$ to 500 g/cm^3 and $T = 2000$ to 10^8 K. The resulting pressures and internal energies have been assembled into a first-principles equation-of-state table, which is studied in detail by comparing it with the extensively used *SESAME* 3810 table of silicon. We found that the shock Hugoniot of silicon is ~20% softer in FPEOS than *SESAME* 3810. For off-Hugoniot warm-dense-plasma conditions, the pressure difference can reach ~50% between FPEOS and *SESAME* 3810, while the internal energy difference is within ~20%. After implementing the FPEOS table of silicon into our 1-D radiation–hydrodynamics code *LILAC*, we tested its effects on HED plasma simulation by carrying out hydro-simulations of an ICF implosion with a Si shell using either FPEOS or *SESAME* 3810. The simulation results showed (a) the FPEOS-predicted shock density is ~20% higher than the *SESAME* 3810 case (accordingly, the shock speed is ~10% lower in the former case); (b) the peak density of the imploding Si shell is ~20% larger in FPEOS than in *SESAME*; (c) the maximum density at peak compression is higher by ~40%; and (d) the final areal density and yield predicted by FPEOS are respectively higher by ~30% and ~70%, with respect to the *SESAME* simulation. The observed differences in target performance can be attributed to the different compressibility of silicon predicted by FPEOS. These studies illustrate the importance of having a more-accurate EOS table in order to precisely design ICF/HED experiments. Hopefully these results will facilitate shock-wave experiments in the untested high-pressure (>10-Mbar) regime.

REFERENCES

1. G. J. Cheng *et al.*, J. Manuf. Sci. Eng. **130**, 011008 (2008).

2. Y. Zhang *et al.*, Geophys. Res. Lett. **41**, 4554 (2014).

3. H. Sai *et al.,* Appl. Phys. Lett. **106**, 213902 (2015).

4. A. Benuzzi-Mounaix *et al.*, Phys. Scr. **2014**, 014060 (2014).

5. W. D. Langer and A. E. Glassgold, Astrophys. J. **352**, 123 (1990).

6. P. Schilke *et al.*, Astron. Astrophys. **321**, 293 (1997).

7. M. J. Edwards, J. D. Lindl, B. K. Spears, S. V. Weber, L. J. Atherton, D. L. Bleuel, D. K. Bradley, D. A. Callahan, C. J. Cerjan, D. Clark, G. W. Collins, J. E. Fair, R. J. Fortner, S. H. Glenzer, S. W. Haan, B. A. Hammel, A. V. Hamza, S. P. Hatchett, N. Izumi, B. Jacoby, O. S. Jones, J. A. Koch, B. J. Kozioziemski, O. L. Landen, R. Lerche, B. J. MacGowan, A. J. MacKinnon, E. R. Mapoles, M. M. Marinak, M. Moran, E. I. Moses, D. H. Munro, D. H. Schneider, S. M. Sepke, D. A. Shaughnessy, P. T. Springer, R. Tommasini, L. Bernstein, W. Stoeffl, R. Betti, T. R. Boehly, T. C. Sangster, V. Yu. Glebov, P. W. McKenty, S. P. Regan, D. H. Edgell, J. P. Knauer, C. Stoeckl, D. R. Harding, S. Batha, G. Grim, H. W. Herrmann, G. Kyrala, M. Wilke, D. C. Wilson, J. Frenje, R. Petrasso, K. Moreno, H. Huang, K. C. Chen, E. Giraldez, J. D. Kilkenny, M. Mauldin, N. Hein, M. Hoppe, A. Nikroo, and R. J. Leeper, Phys. Plasmas **18**, 051003 (2011).

8. R. L. McCrory, R. Betti, T. R. Boehly, D. T. Casey, T. J. B. Collins, R. S. Craxton, J. A. Delettrez, D. H. Edgell, R. Epstein, J. A. Frenje, D. H. Froula, M. Gatu-Johnson, V. Yu. Glebov, V. N. Goncharov, D. R. Harding, M. Hohenberger, S. X. Hu, I. V. Igumenshchev, T. J. Kessler, J. P. Knauer, C. K. Li, J. A. Marozas, F. J. Marshall, P. W. McKenty, D. D. Meyerhofer, D. T. Michel, J. F. Myatt, P. M. Nilson, S. J. Padalino, R. D. Petrasso, P. B. Radha, S. P. Regan, T. C. Sangster, F. H. Séguin, W. Seka, R. W. Short, A. Shvydky, S. Skupsky, J. M. Soures, C. Stoeckl, W. Theobald, B. Yaakobi, and J. D. Zuegel, Nucl. Fusion **53**, 113021 (2013).

9. R. S. Craxton, K. S. Anderson, T. R. Boehly, V. N. Goncharov, D. R. Harding, J. P. Knauer, R. L. McCrory, P. W. McKenty, D. D. Meyerhofer, J. F. Myatt, A. J. Schmitt, J. D. Sethian, R. W. Short, S. Skupsky, W. Theobald, W. L. Kruer, K. Tanaka, R. Betti, T. J. B. Collins, J. A. Delettrez, S. X. Hu, J. A. Marozas, A. V. Maximov, D. T. Michel, P. B. Radha, S. P. Regan, T. C. Sangster, W. Seka, A. A. Solodov, J. M. Soures, C. Stoeckl, and J. D. Zuegel, Phys. Plasmas **22**, 110501 (2015).

10. S. W. Haan *et al.*, Phys. Plasmas **18**, 051001 (2011).

11. S. X. Hu, G. Fiksel, V. N. Goncharov, S. Skupsky, D. D. Meyerhofer, and V. A. Smalyuk, Phys. Rev. Lett. **108**, 195003 (2012).

12. G. Fiksel, S. X. Hu, V. N. Goncharov, D. D. Meyerhofer, T. C. Sangster, V. A. Smalyuk, B. Yaakobi, M. J. Bonino, and R. Jungquist, Phys. Plasmas **19**, 062704 (2012).

13. S. X. Hu, D. T. Michel, D. H. Edgell, D. H. Froula, R. K. Follett, V. N. Goncharov, J. F. Myatt, S. Skupsky, and B. Yaakobi, Phys. Plasmas **20**, 032704 (2013).

14. J. F. Myatt, H. X. Vu, D. F. DuBois, D. A. Russell, J. Zhang, R. W. Short, and A. V. Maximov, Phys. Plasmas **20**, 052705 (2013).

15. V. N. Goncharov, T. C. Sangster, R. Betti, T. R. Boehly, M. J. Bonino, T. J. B. Collins, R. S. Craxton, J. A. Delettrez, D. H. Edgell, R. Epstein, R. K. Follet, C. J. Forrest, D. H. Froula, V. Yu. Glebov, D. R. Harding, R. J. Henchen, S. X. Hu, I. V. Igumenshchev, R. Janezic, J. H. Kelly, T. J. Kessler, T. Z. Kosc, S. J. Loucks, J. A. Marozas, F. J. Marshall, A. V. Maximov, R. L. McCrory, P. W. McKenty, D. D. Meyerhofer, D. T. Michel, J. F. Myatt, R. Nora, P. B. Radha, S. P. Regan, W. Seka, W. T. Shmayda, R. W. Short, A. Shvydky, S. Skupsky, C. Stoeckl, B. Yaakobi, J. A. Frenje, M. Gatu-Johnson, R. D. Petrasso, and D. T. Casey, Phys. Plasmas **21**, 056315 (2014).

16. M. N. Pavlovskii, Sov. Phys.-Solid State **9**, 2514 (1968).

17. W. H. Gust and E. B. Royce, J. Appl. Phys. **42**, 1897 (1971).

18. T. Goto, T. Sato, and Y. Syono, Jpn. J. Appl. Phys. **21**, L369 (1982).

19. L. Loveridge-Smith, A. Allen, J. Belak, T. Boehly, A. Hauer, B. Holian, D. Kalantar, G. Kyrala, R. W. Lee, P. Lomdahl, M. A. Meyers, D. Paisley, S. Pollaine, B. Remington, D. C. Swift, S. Weber, and J. S. Wark, Phys. Rev. Lett. **86**, 2349 (2001).

20. P. Celliers, A. Ng, G. Xu, and A. Forsman, Phys. Rev. Lett. **68**, 2305 (1992).

21. A. Ng, P. Celliers, G. Xu, and A. Forsman, Phys. Rev. E **52**, 4299 (1995).

22. Th. Löwer *et al.*, Phys. Rev. Lett. **80**, 4000 (1998).

23. E. J. Reed, J. D. Joannopoulos, and L. E. Fried, AIP Conf. Proc. **620**, 343 (2002).

24. I. I. Oleynik *et al.*, AIP Conf. Proc. **845**, 413 (2006).

25. G. Mogni *et al.*, Phys. Rev. B. **89**, 064104 (2014).

26. D. C. Swift *et al.*, Phys. Rev. B **64**, 214107 (2001).

27. B. Militzer and K. P. Driver, Phys. Rev. Lett. **115**, 176403 (2015).

28. O. Strickson and E. Artacho, Phys. Rev. B **93**, 094107 (2016).

29. S. X. Hu, B. Militzer, L. A. Collins, K. P. Driver, and J. D. Kress, Phys. Rev. B **94**, 094109 (2016).

30. B. I. Bennett *et al.*, Los Alamos National Laboratory, Los Alamos, NM, Report LA-7130 (1978).

31. R. M. More *et al.*, Phys. Fluids **31**, 3059 (1988).

32. J. Delettrez, R. Epstein, M. C. Richardson, P. A. Jaanimagi, and B. L. Henke, Phys. Rev. A **36**, 3926 (1987).

33. L. Collins *et al.*, Phys. Rev. E **52**, 6202 (1995).

34. J. G. Clérouin and S. Bernard, Phys. Rev. E **56**, 3534 (1997).

35. L. A. Collins *et al.*, Phys. Rev. B **63**, 184110 (2001).

36. M. P. Desjarlais, Phys. Rev. B **68**, 064204 (2003).

37. C. Pierleoni *et al.*, Phys. Rev. Lett. **73**, 2145 (1994).

38. R. C. Clay *et al.*, Phys. Rev. B **93**, 035121 (2016).

39. S. Root *et al.*, Phys. Rev. Lett. **115**, 198501 (2015).

40. W. Kohn and L. J. Sham, Phys. Rev. **140**, A1133 (1965).

41. F. Lambert, J. Clérouin, and G. Zérah, Phys. Rev. E **73**, 016403 (2006).

42. G. Kresse and J. Hafner, Phys. Rev. B **47**, 558 (1993).

43. G. Kresse and J. Hafner, Phys. Rev. B **49**, 14,251 (1994).

44. G. Kresse and J. Furthmüller, Phys. Rev. B **54**, 11,169 (1996).

45. J. P. Perdew, K. Burke, and M. Ernzerhof, Phys. Rev. Lett. **77**, 3865 (1996); **78**, 1396(E) (1997).

46. P. Hohenberg and W. Kohn, Phys. Rev. **136**, B864 (1964).

47. J. P. Perdew and A Zunger, Phys. Rev. B **23**, 5048 (1981).

48. J. D. Johnson, High Press. Res. **6**, 277 (1991).

49. P. M. Celliers, G. W. Collins, L. B. Da Silva, D. M. Gold, R. Cauble, R. J. Wallace, M. E. Foord, and B. A. Hammel, Phys. Rev. Lett. **84**, 5564 (2000).

50. V. N. Goncharov, T. C. Sangster, P. B. Radha, R. Betti, T. R. Boehly, T. J. B. Collins, R. S. Craxton, J. A. Delettrez, R. Epstein, V. Yu. Glebov, S. X. Hu, I. V. Igumenshchev, J. P. Knauer, S. J. Loucks, J. A. Marozas, F. J. Marshall, R. L. McCrory, P. W. McKenty, D. D. Meyerhofer, S. P. Regan, W. Seka, S. Skupsky, V. A. Smalyuk, J. M. Soures, C. Stoeckl, D. Shvarts, J. A. Frenje, R. D. Petrasso, C. K. Li, F. Séguin, W. Manheimer, and D. G. Colombant, Phys. Plasmas **15**, 056310 (2008).

51. I. V. Igumenshchev, D. H. Edgell, V. N. Goncharov, J. A. Delettrez, A. V. Maximov, J. F. Myatt, W. Seka, A. Shvydky, S. Skupsky, and C. Stoeckl, Phys. Plasmas **17**, 122708 (2010).

52. S. X. Hu, B. Militzer, V. N. Goncharov, and S. Skupsky, Phys. Rev. Lett. **104**, 235003 (2010).

53. S. X. Hu, B. Militzer, V. N. Goncharov, and S. Skupsky, Phys. Rev. B **84**, 224109 (2011).

54. S. X. Hu, L. A. Collins, V. N. Goncharov, T. R. Boehly, R. Epstein, R. L. McCrory, and S. Skupsky, Phys. Rev. E **90**, 033111 (2014).

55. M. Lafon, R. Betti, K. S. Anderson, T. J. B. Collins, R. Epstein, P. W. McKenty, J. F. Myatt, A. Shvydky, and S. Skupsky, Phys. Plasmas **22**, 032703 (2015).

First Measurements of Deuterium–Tritium and Deuterium–Deuterium Fusion-Reaction Yields in Ignition-Scalable Direct-Drive Implosions

In direct-drive inertial confinement fusion (ICF) ignition designs, a cryogenic deuterium–tritium (DT) shell surrounding a vapor and encased in a thin ablator (<10 μm) is symmetrically heated with nominally identical laser beams. In most designs, laser ablation launches single or multiple shocks through the converging shell and into the vapor region. The shock-transit stage of the implosion is followed by a deceleration phase, where the kinetic energy of the converging shell is converted to the internal energy of the hot spot. Thermonuclear fusion reactions are initiated in both the shock phase and the compression phase once sufficiently high temperatures and densities are reached. To achieve conditions relevant for ignition implosion designs, the hot-spot size must exceed the mean free path of fusing ions and the mean free path of the alpha particles.

Previous experiments on OMEGA have reported anomalous Y_{DT}/Y_{DD} values (different by as much as a factor of 4) with the measured pre-shot fuel composition and experimentally inferred ion temperatures in room-temperature implosions.[1] Several studies suggest that species separation of the hydrogen isotope resulting from multifluid effects[2,3] is likely responsible for the observed discrepancies in the yield ratios. These classes of implosions—for example, exploding pushers that use thin glass (~3-μm SiO$_2$) or thin CH (<16-μm) shells—are, however, characterized by fusion reactions that occur predominantly during the shock phase at very high temperatures ($\geq$10 keV)

and relatively low densities ($\leq$10 mg/cm^3). The mean free path for 90° deflection is given by $\lambda_{ii} \sim T_i^2 / Z_i^2 Z^2 \rho$ (Ref. 4) for ions of charge Z_i, average ion temperature T_i, ion charge Z, and density ρ. Conditions during the shock phase result in large mean-free-path lengths of the ions relative to the size of the fusing-plasma region (see Table 149.II). These conditions are also typical of ignition-relevant direct-drive cryogenic implosions[5] during the shock phase; however, cryogenic targets differ from exploding-pusher targets in two respects: First, most of the neutron yield in a cryogenic implosion occurs later in the implosion, during the compression phase, when the kinetic energy is converted to the internal energy of the hot spot. Simulations using the spherically symmetric hydrodynamics code *LILAC*[6] indicate that nearly 99% of the yield occurs in this compression phase. Second, compression yields occur at significantly higher densities ($\geq$20 g/cm^3) and lower temperatures (~3 keV), leading to mean free paths of thermal ions that are much shorter than the hot-spot size. Nonlocal transport of energetic ions is therefore not expected to significantly influence yields during compression. Evidence of fuel species separation that persists into the compression phase would suggest a reduction in the number of alpha particles produced from the dominant D–T fusion reactions. In ignition-scalable cryogenic implosions described in this article, however, measurements give the first evidence that species separation does not persist from the shock phase and has an insignificant influence on

Table 149.II: Calculated implosion parameters for various plasma conditions ranging from a highly kinetic exploding pusher (in the shock phase in the vapor) to a strongly hydrodynamic-like plasma regime (cold-fuel layer in the shock or compression phase).

Implosion Type	ρ (g/cm^3)	T_i (keV)	λ_{ii} (μm)	R_{shell} (μm)
Exploding pusher:				
Shock phase	0.03	10	400	100
Cryogenic implosions:				
Shock phase: vapor	0.1	8	80	100
Shock phase: cold-fuel layer	6.0	0.02	0.0002	$\Delta R_{shell} \sim 10$
Compression phase	20.0	3	0.08	25

the yield ratio into the compression phase in direct-drive D–T cryogenic implosions consisting of a near-equimolar mixture of deuterium and tritium.[7]

Direct-drive ICF targets consisting of a deuterated plastic (ablator) shell with a 460-μm outer radius are imploded at an ignition-scalable, on-target laser intensity with a laser energy of ~25 kJ (Ref. 8). The implosion velocity (V_{imp}, defined as the velocity of the compressing shell when the kinetic energy of the shell is at a maximum) ranged from 3.5×10^7 cm/s to 4×10^7 cm/s and the adiabat (α, defined as the ratio of the pressure to the Thomas–Fermi pressure at maximum shell density) ranged from 2.4 to 5. The average ion temperature T_i in this class of implosions is varied by adjusting the implosion velocity, $T_i \sim V_{imp}^{1.1}$, which, in turn, is governed by the thickness of the cryogenic DT layers or the CH (CD) ablator. The capsule is filled by a permeation technique at a temperature of 300 K, where increasing pressure is applied to the outside of the shell, allowing the gas to diffuse inside. Fill rates for a typical cryogenic target are carefully controlled by holding the pressure ramp rate at ~1 atm/min to ensure the integrity of the shell is not compromised.[9] At the final fill pressure (between 400 and 800 atm) depending on the desired ice thickness, the capsule is cooled to a few mK below the triple point (~19.8 K), producing a DT ice layer ranging from 40 to 90 μm in thickness. The primary nuclear-fusion reactions examined in this study are given by

$$D + D \rightarrow {}^3He + n + (3.27 \text{ MeV}), \tag{1}$$

$$D + T \rightarrow {}^4He + n + (17.6 \text{ MeV}). \tag{2}$$

The neutron yields are measured using the time-of-flight (nTOF) diagnostics positioned around the OMEGA target chamber. The fusion yield is given by

$$Y_n^{DD/DT} = \int f_D f_{D/T} \left[\rho(\vec{r}, t) \right]^2 \langle \sigma v \rangle_{DT/DD}$$
$$\times \, dr^3 \, dt / (1 + \delta_{DD}) \overline{m}^2,$$

where f_T and f_D are the atomic fractions of the reactants, ρ is the fuel-mass density, $\langle \sigma v \rangle$ is the Maxwellian-averaged reactivity for the D–T or D–D fusion reaction (which scales as ~$T_i^{3.7}$ for the D–T reaction and ~$T_i^{3.3}$ for the D–D reaction for the typical temperatures in OMEGA implosions), T_i is the average ion temperature, $\overline{m}$ is the average reactant mass, and $\delta_{DD} = 1$ for DD and 0 for DT to account for double counting of the identical D–D reaction.

The primary D–T yields observed in cryogenic experiments are always lower relative to radiation–hydrodynamics codes that assume spherical symmetry and include the deposition of the laser energy through collisional absorption and account for laser–plasma interactions such as cross-beam energy transfer (CBET).[10] These codes include nonlocal heat conduction[10] and multigroup diffusive radiative transport.[11] Several multi-dimensional effects that reduce the overall yield relative to these state-of-the-art spherically symmetric fluid codes have been proposed, including nonuniformity growth caused by beam-to-beam energy imbalance,[12] on-target beam misalignment,[13] single-laser-beam nonuniformity,[13] and isolated defects on the target[14] that potentially reduce T_i and/or fuel density. All these mechanisms include only hydrodynamic effects and do not exhibit yield ratio anomalies. More recently, an extension to fluid codes has been proposed. Calculations that include plasma barotropic diffusion,[15,16] where hydrogen isotope species separation occurs during the shock phase into the hot spot because gradients in pressure and temperature, have been shown to influence the D–T and D–D fusion yields differently. Two phases of an ICF implosion have been analyzed using this model: the shock phase (when the shock is moving through the vapor toward the center of the capsule) followed by the rebound phase (outward-going shock). It was reported that during the shock phase, up to 5% of the deuterium can leave the fuel volume for an equimolar mixture of deuterium and tritium. During the subsequent shock-rebound phase, the barotropic diffusion rate decreases to zero and the ability for fuel to leave the volume is significantly reduced if not eliminated. Since the D–D fusion and D–T fusion reactivity are well-known[17] and the composition of the fuel is measured prior to the implosion, the ratio of the neutron yields $\left(Y_{DT} / Y_{DD} \right)$ from these reactions should follow a calculable trend with the measured ion temperature with the exclusion of diffusive effects. Table 149.II summarizes the mass-fuel density (ρ) and the key implosion parameters to calculate the ion–ion mean free path (λ_{ii}) for the plasma conditions across the class of implosions discussed earlier in this article. The radius of the shell (R_{shell}) is calculated from simulations for the different phases of the implosion.

As shown in Table 149.II, the mean free path during the shock phase for the ions at the relevant average ion temperature approaches the radius of the shell. At this time, however, the vapor region is surrounded by a relatively cold (~20-eV) and highly dense DT-fuel layer. The energetic and thermal ions that escape the vapor phase do not leave the target and instead are stopped in the cold dense DT shell. At peak neutron production, the mean free path is several orders of magnitude smaller (~10^{-2}) than the boundary of the cold-fuel shell.

Cryogenic implosions are additionally different from shock-driven implosions that have been studied previously since the shell material is also made of DT fuel. When the shell decelerates in the compression stage of any ICF implosion, the cold fuel ablates into the hot spot. Simulations using the code *LILAC* indicate that, in the case of cryogenic layered DT implosions, nearly 5× the mass of the original vapor[6] is injected into the hot spot through the ablation process, which is the primary source of the fusion neutrons during compression. Therefore, it would be expected that the ions that are stopped in the cold-fuel shell would be restored into the hot core during the compression phase, compensating for any loss of particles that may have occurred earlier in the implosion.

For this analysis, the yields (Y_{DT} and Y_{DD}) for the different reactions are measured along the same diagnostic line of sight using the 13.4-m high-resolution nTOF spectrometer.[18] This diagnostic uses several microchannel-plate–based phototubes to increase the dynamic range required to measure the primary DT and DD signal in a single line of sight. The yield is inferred by fitting the recorded signal with a forward-fit approach using a relativistic model of the neutron distribution.[19] Cross-calibration of the neutron diagnostics with standard measurements on OMEGA give an uncertainty in the D–T and D–D yields of 5% and 9%, respectively.[20,21] In ignition-scalable implosions, the neutron yield is attenuated by the compressed fuel at peak neutron production (see Table 149.II). To recover the fusion birth yield, a correction to the measured yields must be included as a function of the areal density from the compressed fuel. The elastic scattering is proportional to the areal density of the implosion, which is inferred from separate measurements.[22] The transmission factors (η_{DT} and η_{DD}) for the neutrons from the two fusion reactions are calculated using the well-known total scattering cross sections and the measured areal density. Typical values of these transmission factors for an areal density of 220 mg/cm^2 are 4% and 10% for the DT and DD neutrons, respectively. With the areal densities achieved on OMEGA, multiple scattering can be neglected, thereby providing an ideal platform to study the effects of fuel-species separation in ignition-scalable implosions. By adding the uncertainty of the D–T and D–D yields, the attenuation of the yield from the compressed fuel and the reaction rate for both of the primary reactions in quadrature, an error of 10% for the $Y_{DT}\big/Y_{DD}$ ratio can be inferred.

As indicated earlier, it is important to know the ion temperature in the implosion and the fuel composition. The energy spread of the primary neutron distribution provides a good measure of the ion temperature characteristics of peak neutron production. If mass flow within the reaction region is present, this effect can lead to a broadening of peak distribution and an incorrect interpretation of ion temperature.[23] On OMEGA, several nTOF detectors measure the width of the DT neutron spectrum temperature from various lines of sight around the target chamber.[24] The ion temperature inferred from the width of the neutron spectrum in ignition-scalable implosions can vary up to ~1 keV across the three different detectors. Simulations indicate that this variation in the temperature is caused by bulk fluid motion of the fusing plasma.[25] The uncertainty in the inferred ion temperature, excluding effects caused by bulk fluid motion, is ±0.2 keV for implosions between 2 keV and 5 keV. To minimize the effect of bulk motion, the minimum ion temperature will be used in this analysis as an approximation of the thermal temperature. It should be noted that the implosions that can vary up to 1 keV are only 3% of the data points. The remaining 2σ that vary up to 0.8 keV account for 90% of the implosion analyzed. Using this variation in the ion temperature, the calculated fuel fraction has an uncertainty of less than 7%.

The observed reaction yield ratio is plotted as a function of the minimum ion temperature in Fig. 149.24 for each cryogenic shot on OMEGA (35 experimental campaigns with 120 implosions taken over a period of three years). The composition of the DT inventory in the assay volume is periodically measured on OMEGA to within an accuracy of 1.5%. In this case, the gas used to fill the targets was taken at various stages during the pressurization of the fuel so that the deuterium-to-tritium (D:T) concentration could be calculated. Over time, the tritium supply in the system gradually changes as a result of beta decay of the hydrogen isotope. Figure 149.24 also shows the calculated ratios using the measured fuel fraction and the minimum ion temperature. The measured ratios show good agreement with the calculated ratios expected from the DT inventory and experimentally inferred ion temperatures. It should be noted that while the accuracy of the fuel composition in the both the assay volume and the pressurized system are well understood, an extrapolation of the fuel fraction is required of the gas composition during the fill process in the permeation cell that is used to fill cryogenic capsules. A project is underway to better characterize the fuel composition of the gas as it is sent into the permeation cell used to fill the capsules. Presently, this effect is known to change the composition between 3% and 5%. The calculated reaction yield ratios follow the form $Y_{DT}\big/Y_{DD} \sim 2T_i^{0.4}\left(f_T\big/f_D\right)$ using the assumption that hydrodynamic models of an ICF implosion predict that the reactant density ratio $\left(f_T\big/f_D\right)$ is spatially and temporally constant during all phases. This indicates that additional effects that change this ratio or the volume over

which each of the D–T and D–D reactions are produced do not significantly influence yields from the hot-spot stagnation. Pre-shot fuel fractions are measured during each fill process for every campaign. Variations in the yield ratio measurements resulting from the fuel composition are reflected in Fig. 149.24 with the solid and dashed lines representing the initial and final


(a)

(b)

(c)

$$T_i^{DT} \text{(keV)}$$
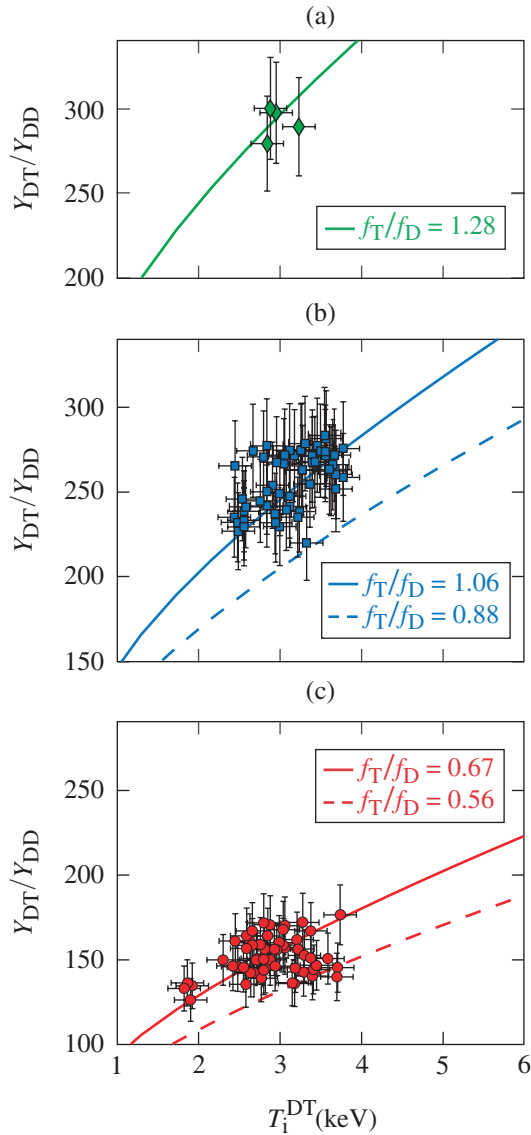
E25147JR

Figure 149.24
With each cryogenic implosion, the Y_{DT}/Y_{DD} yield ratio is plotted with the minimum DT neutron averaged ion temperature. The T:D fuel fraction used to fill the cryogenic targets varied between (a) $f_T/f_D \sim 0.58$ and (b) $f_T/f_D \sim 1$ for the majority of the cryogenic targets. (c) A single campaign had a fill fraction of $f_T/f_D \sim 1.28$. The solid lines represent the initial measurement of fuel inventory and the dashed lines show how much the fuel has changed over time resulting from tritium decay. The hydrogen concentration does not contribute to the fusion yield and is not included in this analysis.

measurement, respectively, before the inventory underwent a scheduled refinement.

The measured D–T and D–D yield ratios and the ion temperature are used to instead infer a fuel fraction (f_D and f_T) for each of these shots. The measured fuel fraction is compared against values inferred from nuclear measurements in Fig. 149.25. The average of the ratio of the inferred fuel fraction from the nuclear measurement over the composition obtained from the permeation cell is 1.07 with a standard deviation of 0.09. Although error on the mean is small with 1% for 120 implosions used for this study, given the 10% systematic error on the Y_{DT}/Y_{DD} ratio, both measurements of the fuel fractions are consistent within the experimental uncertainties.
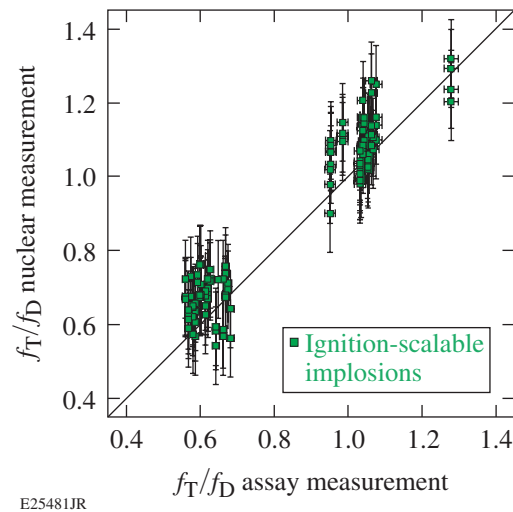
E25481JR

Figure 149.25
The measured fuel fraction determined at the fill station (assay measurement) is compared with the values inferred from the nuclear measurements over a three-year period. The changes in the fuel fraction used to fill the targets is clearly visible between $f_D/f_D \sim 0.58$ and $f_D/f_D \sim 1$. A single campaign with four implosions had a fill fraction of $f_T/f_D \sim 1.28$.

In summary, nuclear measurements of the D–T to D–D yield ratio from OMEGA cryogenic implosions scale predictably with the known composition of the fuel and experimentally inferred ion temperatures with a calculated 7% systematic offset. These observations indicate that multifluid effects that may take place during the shock phase of the implosion (and potentially influence species profiles in the compressing target) do not persist into the subsequent compression phase of the implosion. A plausible explanation for this rests on the composition of the target; the shell is also DT fuel. During the deceleration phase of cryogenic DT implosions, the fuel from the inner DT wall is ablated into the hot spot. Simula-

tions indicate that nearly 5× the mass of the neutron-emitting region is from the ablation of the cold DT shell. Therefore, the energetic ions that may be lost because of their long mean free paths earlier in the implosion return to the hot spot during peak neutron production, leading to an unchanged fusion yield ratio. These observations indicate that multifluid effects have an insignificant influence on the yield ratio in ignition-scalable cryogenic implosions.

The largest contribution to the uncertainty in the yield ratio measurement is caused by the D–D yield. Upcoming experiments are designed to increase the accuracy of this measurement to 5%. These experiments will reduce the uncertainty in the $Y_{\text{DT}}/Y_{\text{DD}}$ ratio to 7%, which, in turn, will also increase the accuracy of the inferred fuel fractions obtained from this measurement.

Presently, there is no measurement available of the true temperature of the plasma, which is very important for this measurement. Several projects are being considered that will provide a true thermal temperature that is not influenced by the bulk motion of the plasma.

ACKNOWLEDGMENT

REFERENCES

1. D. T. Casey, J. A. Frenje, M. Gatu Johnson, M. J.-E. Manuel, H. G. Rinderknecht, N. Sinenian, F. H. Séguin, C. K. Li, R. D. Petrasso, P. B. Radha, J. A. Delettrez, V. Yu. Glebov, D. D. Meyerhofer, T. C. Sangster, D. P. McNabb, P. A. Amendt, R. N. Boyd, J. R. Rygg, H. W. Herrmann, Y. H. Kim, and A. D. Bacher, Phys. Rev. Lett. **108**, 075002 (2012).

2. M. J. Rosenberg, A. B. Zylstra, F. H. Séguin, H. G. Rinderknecht, J. A. Frenje, M. Gatu Johnson, H. Sio, C. J. Waugh, N. Sinenian, C. K. Li, R. D. Petrasso, P. W. McKenty, M. Hohenberger, P. B. Radha, J. A. Delettrez, V. Yu. Glebov, R. Betti, V. N. Goncharov, J. P. Knauer, T. C. Sangster, S. LePape, A. J. Mackinnon, J. Pino, J. M. McNaney, J. R. Rygg, P. A. Amendt, C. Bellei, L. R. Benedetti, L. Berzak Hopkins, R. M. Bionta, D. T. Casey, L. Divol, M. J. Edwards, S. Glenn, S. H. Glenzer, D. G. Hicks, J. R. Kimbrough, O. L. Landen, J. D. Lindl, T. Ma, A. MacPhee, N. B. Meezan, J. D. Moody, M. J. Moran, H.-S. Park, B. A. Remington, H. Robey, M. D. Rosen, S. C. Wilks, R. A. Zacharias, H. W. Herrmann, N. M. Hoffman, G. A. Kyrala, R. J. Leeper, R. E. Olson, J. D. Kilkenny, and A. Nikroo, Phys. Plasmas **21**, 122712 (2014).

3. H. G. Rinderknecht, M. J. Rosenberg, C. K. Li, N. M. Hoffman, G. Kagan, A. B. Zylstra, H. Sio, J. A. Frenje, M. Gatu Johnson, F. H. Séguin, R. D. Petrasso, P. Amendt, C. Bellei, S. Wilks, J. Delettrez, V. Yu. Glebov, C. Stoeckl, T. C. Sangster, D. D. Meyerhofer, and A. Nikroo, Phys. Rev. Lett. **114**, 025001 (2014).

4. D. B. Henderson, Phys. Rev. Lett. **33**, 1142 (1974).

5. V. N. Goncharov, T. C. Sangster, R. Betti, T. R. Boehly, M. J. Bonino, T. J. B. Collins, R. S. Craxton, J. A. Delettrez, D. H. Edgell, R. Epstein, R. K. Follet, C. J. Forrest, D. H. Froula, V. Yu. Glebov, D. R. Harding, R. J. Henchen, S. X. Hu, I. V. Igumenshchev, R. Janezic, J. H. Kelly, T. J. Kessler, T. Z. Kosc, S. J. Loucks, J. A. Marozas, F. J. Marshall, A. V. Maximov, R. L. McCrory, P. W. McKenty, D. D. Meyerhofer, D. T. Michel, J. F. Myatt, R. Nora, P. B. Radha, S. P. Regan, W. Seka, W. T. Shmayda, R. W. Short, A. Shvydky, S. Skupsky, C. Stoeckl, B. Yaakobi, J. A. Frenje, M. Gatu-Johnson, R. D. Petrasso, and D. T. Casey, Phys. Plasmas **21**, 056315 (2014).

6. J. Delettrez, R. Epstein, M. C. Richardson, P. A. Jaanimagi, and B. L. Henke, Phys. Rev. A **36**, 3926 (1987).

7. S. P. Regan, V. N. Goncharov, I. V. Igumenshchev, T. C. Sangster, R. Betti, A. Bose, T. R. Boehly, M. J. Bonino, E. M. Campbell, D. Cao, T. J. B. Collins, R. S. Craxton, A. K. Davis, J. A. Delettrez, D. H. Edgell, R. Epstein, C. J. Forrest, J. A. Frenje, D. H. Froula, M. Gatu Johnson, V. Yu. Glebov, D. R. Harding, M. Hohenberger, S. X. Hu, D. Jacobs-Perkins, R. T. Janezic, M. Karasik, R. L. Keck, J. H. Kelly, T. J. Kessler, J. P. Knauer, T. Z. Kosc, S. J. Loucks, J. A. Marozas, F. J. Marshall, R. L. McCrory, P. W. McKenty, D. D. Meyerhofer, D. T. Michel, J. F. Myatt, S. P. Obenschain, R. D. Petrasso, R. B. Radha, B. Rice, M. Rosenberg, A. J. Schmitt, M. J. Schmitt, W. Seka, W. T. Shmayda, M. J. Shoup III, A. Shvydky, S. Skupsky, S. Solodov, C. Stoeckl, W. Theobald, J. Ulreich, M. D. Wittman, K. M. Woo, B. Yaakobi, and J. D. Zuegel, Phys. Rev. Lett. **117**, 025001 (2016); **117**, 059903(E) (2016).

8. C. D. Zhou and R. Betti, Phys. Plasmas **14**, 072703 (2007).

9. W. T. Shmayda, M. D. Wittman, R. F. Earley, J. L. Reid, and N. P. Redden, Fusion Eng. Des. **109–111**, 128 (2016).

10. I. V. Igumenshchev, W. Seka, D. H. Edgell, D. T. Michel, D. H. Froula, V. N. Goncharov, R. S. Craxton, L. Divol, R. Epstein, R. Follett, J. H. Kelly, T. Z. Kosc, A. V. Maximov, R. L. McCrory, D. D. Meyerhofer, P. Michel, J. F. Myatt, T. C. Sangster, A. Shvydky, S. Skupsky, and C. Stoeckl, Phys. Plasmas **19**, 056314 (2012).

11. V. N. Goncharov, O. V. Gotchev, E. Vianello, T. R. Boehly, J. P. Knauer, P. W. McKenty, P. B. Radha, S. P. Regan, T. C. Sangster, S. Skupsky, V. A. Smalyuk, R. Betti, R. L. McCrory, D. D. Meyerhofer, and C. Cherfils-Clérouin, Phys. Plasmas **13**, 012702 (2006).

12. I. V. Igumenshchev, V. N. Goncharov, F. J. Marshall, J. P. Knauer, E. M. Campbell, C. J. Forrest, D. H. Froula, V. Yu. Glebov, R. L. McCrory, S. P. Regan, T. C. Sangster, S. Skupsky, and C. Stoeckl, Phys. Plasmas **23**, 052702 (2016).

13. S. X. Hu, V. N. Goncharov, P. B. Radha, J. A. Marozas, S. Skupsky, T. R. Boehly, T. C. Sangster, D. D. Meyerhofer, and R. L. McCrory, Phys. Plasmas **17**, 102706 (2010).

14. I. V. Igumenshchev, V. N. Goncharov, W. T. Shmayda, D. R. Harding, T. C. Sangster, and D. D. Meyerhofer, Phys. Plasmas **20**, 082703 (2013).

15. P. Amendt *et al.*, Phys. Rev. Lett. **105**, 115005 (2010).

16. G. Kagan and X.-Z. Tang, Phys. Lett. A **378**, 1531 (2014).

17. H.-S. Bosch and G. M. Hale, Nucl. Fusion **32**, 611 (1992).

18. C. J. Forrest, V. Yu. Glebov, V. N. Goncharov, J. P. Knauer, P. B. Radha, S. P. Regan, M. H. Romanofsky, T. C. Sangster, M. J. Shoup, and C. Stoeckl, Rev. Sci. Instrum. **87**, 11D814 (2016).

19. L. Ballabio, J. Källne, and G. Gorini, Nucl. Fusion **38**, 1723 (1998).

20. O. Landoas, V. Yu. Glebov, B. Rossé, M. Briat, L. Disdier, T. C. Sangster, T. Duffy, J. G. Marmouget, C. Varignon, X. Ledoux, T. Caillaud, I. Thfoin, and J.-L. Bourgade, Rev. Sci. Instrum. **82**, 073501 (2011).

21. C. Waugh, "An Improved Method for Measuring the Absolute DD Neutron Yield and Calibrating Neutron Time-of-Flight Detectors in Inertial Confinement Fusion Experiments," M.S. thesis, Massachusetts Institute of Technology, 2014.

22. C. J. Forrest, P. B. Radha, V. Yu. Glebov, V. N. Goncharov, J. P. Knauer, A. Pruyne, M. Romanofsky, T. C. Sangster, M. J. Shoup III, C. Stoeckl, D. T. Casey, M. Gatu-Johnson, and S. Gardner, Rev. Sci. Instrum. **83**, 10D919 (2012).

23. H. Brysk, Plasma Phys. **15**, 611 (1973).

24. V. Yu. Glebov, T. C. Sangster, C. Stoeckl, J. P. Knauer, W. Theobald, K. L. Marshall, M. J. Shoup III, T. Buczek, M. Cruz, T. Duffy, M. Romanofsky, M. Fox, A. Pruyne, M. J. Moran, R. A. Lerche, J. McNaney, J. D. Kilkenny, M. J. Eckart, D. Schneider, D. Munro, W. Stoeffl, R. Zacharias, J. J. Haslam, T. Clancy, M. Yeoman, D. Warwas, C. J. Horsfield, J.-L. Bourgade, O. Landoas, L. Disdier, G. A. Chandler, and R. J. Leeper, Rev. Sci. Instrum. **81**, 10D325 (2010).

25. T. J. Murphy, Phys. Plasmas **21**, 072701 (2014).

Observation of Enhanced Hot-Electron Production and Strong Shock Generation in Hydrogen-Rich Ablators

Generating strong shocks of up to several hundred megabars makes it possible (1) to explore plasma and material properties at the most-extreme conditions of energy density and (2) to develop two-step inertial confinement fusion (ICF) schemes, where ignition is separated from the main compression of the thermonuclear fuel. A promising two-step ignition scheme is shock ignition (SI),[1–4] where ignition is triggered by a strong shock launched at the end of the implosion and driven by a pressure above ~300 Mbar. Detailed reviews of the current status and physics issues for SI are found in Refs. 5–7. One of the most-critical issues is that the ignitor spike pulse requires a laser intensity of 5×10^{15} to 1×10^{16} W/cm^2, which will excite parametric laser–plasma instabilities (LPI's) in the hot plasma corona surrounding the imploding capsule, thereby transferring a significant amount of the laser energy to the hot electrons. Recent work[8–10] demonstrated that hot electrons can enhance the shock pressure. It is still an open question whether they might preheat a SI target[11] or if the benefits will prevail because the areal density is large enough to stop them in the shell and augment the shock.[12,13] Another concern pertains to the energy coupling. The spike pulse must couple sufficient energy into the target in order to generate a strong-enough shock. LPI's may reduce the coupling efficiency and prevent the seed shock pressure from reaching the required magnitude.

Measuring the pressure at these high intensities directly is nearly impossible, so it must be instead inferred indirectly. Experiments in planar geometry at the Laboratoire pour l'Utilisation des Lasers Intenses (LULI),[14] Omega,[15] and Prague Asterix Laser System (PALS)[16] laser facilities have inferred ablation pressures in the range of ~40 to 90 Mbar, which were limited by lateral heat flow from the laser spots in the planar geometries. The lateral transport was suppressed with the development of a new platform[17,18] that applies spherical targets and x-ray diagnostics. It allows one to evaluate the pressure at shock-ignition–relevant laser intensities. The laser launches an inwardly propagating shock wave that converges at the center, heating a small volume and generating a short x-ray flash that is measured with a time-resolved diagnostic. The shock-launching conditions are inferred by constraining radiation–hydrodynamic simulations to the experimental observables. Several experiments established this scheme as a reliable platform using a variety of laser energies, pulse shapes, and target diameters.

There is a continuing interest in exploring new ablator materials in direct-drive ICF research to improve the hydrodynamic efficiency,[19] mitigate the hot-electron production,[20,21] and suppress the Rayleigh–Taylor instability.[22–24] Recent theoretical work demonstrated an overall better performance with mid-Z ablators than plastic (CH) ablators by suppressing the threshold of detrimental LPI while preserving the hydrodynamic stability properties.[25] All of this work has been performed, however, at laser intensities of up to $\sim 1 \times 10^{15}$ W/cm^2, which is relevant for the standard hot-spot–ignition concept but not for the spike interaction in shock ignition. No work has been performed so far to study how the ablator material affects the spike interaction.

This article describes for the first time the important role that the ablator material plays in the interaction physics at shock-ignition–relevant laser intensities. We discovered that CH ablators produce significantly more hot electrons than the other materials and show that differences in the hot-electron production influence the shock formation. Instantaneous conversion efficiencies (CE's) of laser energy into hot-electron energy reach ~13% in CH and ~4% in C. According to simulations, hot electrons increase the effective maximum ablation pressure by ~77% in CH and by ~45% in C. This important finding sheds light on the LPI physics in an intensity and plasma regime that is insufficiently explored and might provide a path to higher-energy-density states in direct-drive geometry.

The experiment used 60 UV ($\lambda = 351$ nm) beams from the OMEGA laser[26] with a total energy of 22 to 26 kJ that were focused to an overlapping beam intensity of up to $\sim 5 \times 10^{15}$ W/cm^2 on the surface of a spherical solid target. The beams were equipped with small-spot phase plates,[27] polarization smoothing,[28] and smoothing by spectral dispersion (SSD).[29] Details on the phase-plate configuration can be found in Ref. 18.

The targets with an outer diameter of 412 to 496 μm consist of an inner CH core that is doped with Ti with an atomic concentration of 5% and an outer ablator layer with a thickness of 20 to 46 μm of a different material [Fig. 149.26(a)]. The outer layer is irradiated with the laser pulse shown in Fig. 149.26(b). A low-power prepulse of ~1-ns duration produces a plasma corona with which the high-power part of the pulse interacts to generate the shock and the hot electrons.
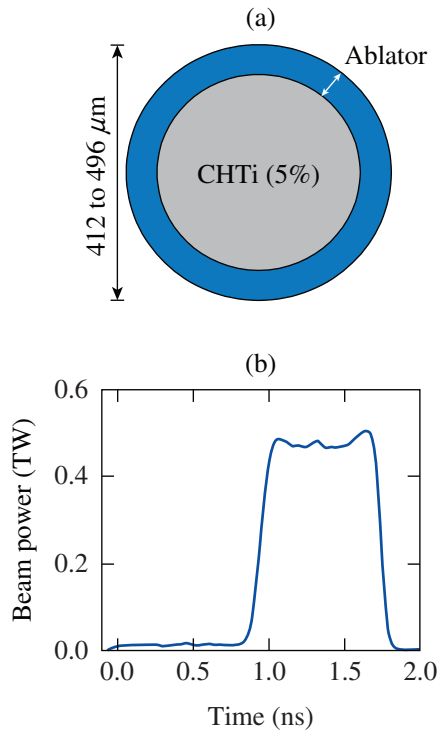
Figure 149.26
(a) Target design consisting of an outer ablator layer of various materials and an inner Ti-doped plastic core; (b) laser pulse shape.

Four different ablator materials (CH, Be, C, and SiO_2) with different atomic numbers (Z) were used. Table 149.III summarizes the parameters of the ablators. The shock wave converges in the center, which results in a short burst of x-ray radiation that is detected spatially and temporally resolved with multiple x-ray framing cameras. Each framing camera was absolutely timed through dedicated timing shots[19,30] with an accuracy of 30 ps. Time-resolved and time-integrated hard x-ray measurements provide a characterization of the hot-electron population (hot-electron temperature and total energy). Optical backscatter diagnostics measure the amount of absorbed laser energy and the back-reflected laser light.

Figure 149.27(a) shows the measured flash time, which is defined as the occurrence of the x-ray flash relative to the start of the laser pulse, for the different ablators with SSD on (squares) and SSD off (circles) in sequence of increasing Z. The measured flash times were adjusted to account for differences in target size, laser energy, and ablator thickness. One-dimensional (1-D) radiation–hydrodynamic simulations were performed with the code $LILAC^{31}$ to analyze the dependence of the flash time on these variables for each material using the actual measured mass densities. The flash times were then adjusted for an ablator thickness that results in a constant ablator mass, a laser energy of 24 kJ, and a target outer diameter of 430 μm in order to obtain a valid comparison for the different targets. The data show the general trend of an earlier flash with increasing Z except for CH, which produced the earliest flash. Turning SSD off advances the flash in CH by ~70 ps, while no significant effect is observed in the other materials. Figure 149.27(b) shows the measured time-integrated CE. Plastic stands out by producing by far the most hot electrons with up to ~2 kJ of total hot-electron energy (time-integrated CE ~8%) deposited in the target when SSD was turned off. Nine and seven shots were performed for CH with SSD on and off, respectively, to prove that the observed difference is

Table 149.III: Ablator materials along with the ratio of average mass number and average ionization degree (assuming full ionization), average outer target diameter (OD), average ablator layer thickness, and measured mass density.

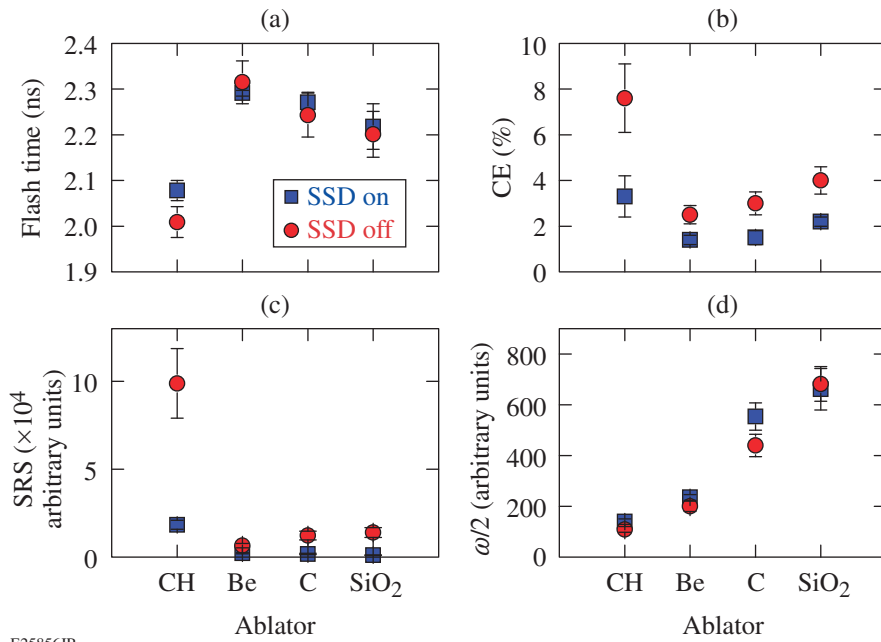| Ablator	$\langle A \rangle / \langle Z_i \rangle$	$\langle OD \rangle$ (μm)	$\langle Thickness \rangle$ (μm)	Density (g/cm^3)
CH	1.86	454	40	1.04±0.01
Be	2.25	430	20	1.84±0.01
C	2.00	444	28	1.4±0.4
SiO_2	2.00	433	20	1.75±0.2

Figure 149.27

(a) X-ray flash time for different ablators with smoothing by spectral dispersion (SSD) on (squares) and SSD off (circles); (b) measured time-integrated conversion efficiency (CE) of laser energy into hot electron energy; (c) stimulated Raman scattering (SRS) backscatter signal; and (d) $\omega/2$ signal.

E25856JR

not an artifact. If CH is treated as an exception, there is the general trend of a slight increase in hot-electron production with higher Z. The inferred hot-electron temperatures lie between 60 and 80 keV and are independent of the ablator and SSD. A high hot-electron fraction corresponds to an earlier flash time, which indicates that hot electrons play a role in the shock formation and augment its strength. The experimental data provide information about the dominant mechanism of hot-electron generation. A clear correlation between hot-electron production and the stimulated Raman scattering (SRS) backscatter signal is observed [Fig. 149.27(c)]. Switching SSD on significantly decreases the SRS signal in all ablators, potentially caused by the suppression of beam filamentation. In contrast, the two-plasmon–decay (TPD) instability, which is the other important hot-electron–generation mechanism, is unaffected by SSD and seems to be far less important than SRS in producing hot electrons. The optical emission generated by electron plasma waves (EPW's) with half the laser frequency ($\omega/2$) is much weaker than the SRS emission and monotonically increases [Fig. 149.27(d)] with Z.

An effective maximum ablation pressure has been inferred (see Fig. 149.28) from simulations. The effect of hot electrons was taken into account by increasing the flux limiter[32] so that the flash time was recovered in the simulations for each ablator material. Although it has been shown in Ref. 17 that the pressure increase from hot electrons may be described by an increased flux limiter, this simplified description does not capture important details such as slowing down, preheat, and
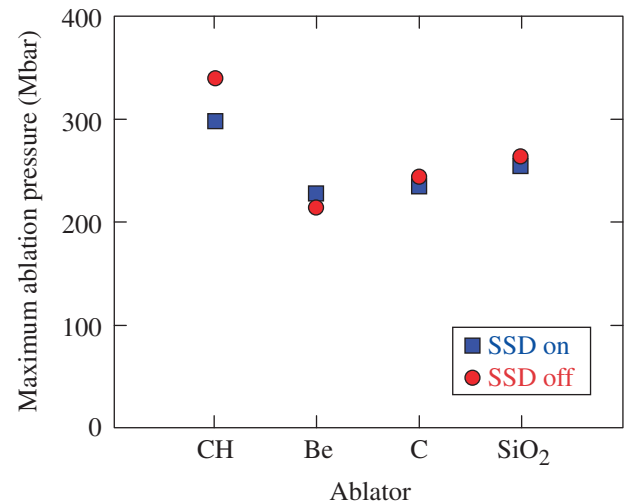
Figure 149.28

Inferred effective maximum ablation pressures for the various materials for an incident laser intensity of 5×10^{15} W/cm^2.

E25857JR

local energy deposition. Additional simulations were performed for the CH target that included a detailed hot-electron transport model, which confirmed the pressures shown in Fig. 149.28.

Figure 149.29 shows the inferred time-resolved CE (red) for two shots with CH (solid) and C (dashed). The blue curves represent the corresponding laser pulse shapes. The onset of hot-electron production lags by ~0.2 ns with respect to the
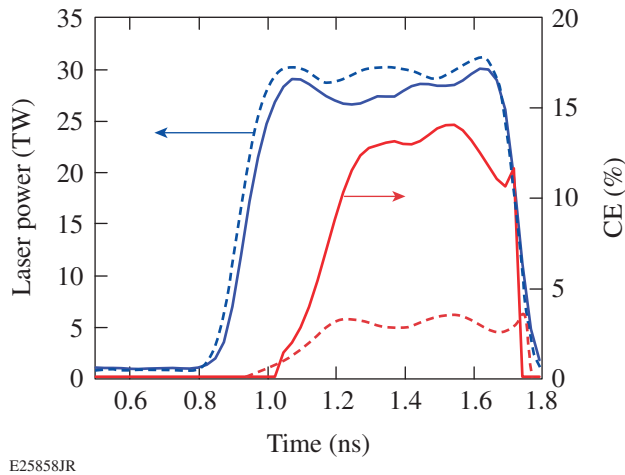
E25858JR

Figure 149.29
Inferred time-resolved conversion efficiency (red) and laser pulse shapes (blue) for two shots with CH (solid curves) and C (dashed curves). Both shots were taken with SSD off. The time resolution of the conversion efficiency is ~100 ps.

rising edge of the laser pulse. This is explained by a strong stimulated Brillouin scattering (SBS) backscatter spike upon the arrival of the main pulse, which reduces temporarily the laser intensity around quarter-critical density $(n_c/4)$ below the threshold of the SRS and TPD instabilities. In addition, the change in temperature and density scale length in this region also directly affects the LPI thresholds. The development of a plateau in the velocity profile in the region between $n_c/10$ and $n_c/4$ promotes a high SBS gain during this time. After the emission spike with a width of ~0.2 ns, SBS remains about constant on a lower level until the end of the laser pulse. Averaged over the laser pulse shape, SBS scatters back ~2% to 3% of the laser energy with no significant difference between ablators. Time-resolved measurements of the SRS backscattering appear to be closely correlated with the hot-electron production. The time-resolved conversion efficiency is based on the measured time-resolved hard x-ray emission[33] in the photon energy range between 50 and 100 keV. It is assumed that the instantaneous amount of hot electrons is proportional to the instantaneous hard x-ray emission. The conversion efficiencies reached 13±2% and 4±1% in CH and C, respectively, during the second half of the high-intensity pulse, while the time-integrated CE over the whole pulse, including the laser energy when no hot electrons were generated, yielded 9±1% and 3±1% for these shots, respectively.

The amount of hot-electron energy coupled into the target core can be estimated with the technique described in Ref. 34 by using two target types that provide the same corona condition and therefore the same hot-electron source but different core conditions. The differences in hard x-ray emission from a target containing a pure CH core and ablator and the Ti-doped core with CH ablator were compared. About 25% of the hot-electron energy was deposited beyond the ablator layer into the unablated dense target, emphasizing the importance of the energy transport by hot electrons.

The experiments demonstrated significant differences between CH and C ablators, indicating that the H species plays an important role in the LPI. To elucidate the SRS physics, 2-D particle-in-cell (PIC) simulations were performed with the code *OSIRIS*[35] by comparing simulations with and without H in the vicinity of $n_c/4$. A simulation with CH was compared to one where H was removed in the vicinity of $n_c/4$ $(n_e > 0.2\,n_c)$. These simulations were designed to identify differences in the fundamental physics of SRS caused by the presence of H between CH and C. A boundary with matched density between CH in the underdense portion and pure C in the higher-density portion ensured that equal conditions were created for the laser pulse propagating through the underdense plasma. The input parameters were obtained from a radiation–hydrodynamic simulation for a CH shot evaluated at 1.5 ns when peak hot-electron production was observed. The PIC simulations assumed the same initial plasma parameters. The input thermal electron and ion temperatures were $T_e = 4$ keV and $T_i = 0.8$ keV, respectively, and the plasma density ramped linearly from $0.12\,n_c$ to $0.30\,n_c$, slightly above $n_c/4$, with a scale length of 123 μm. A plane-wave, 351-nm-wavelength laser pulse propagated along the x axis with a nominal intensity of 2.6×10^{15} W/cm^2 (the same intensity as at $n_c/4$ in the implosion), assuming flattop profiles in both time and space. The effect of SSD was not taken into account in the simulation.

Figures 149.30(a) and 149.30(b) show the calculated longitudinal electric field strength from EPW as a function of time and distance along the direction of laser propagation. Distinct differences in the fields are observed. The electromagnetic wave excites strong EPW over a large region in CH compared to C. The wave modes survive longer in CH and couple better with thermal electrons because of a larger **k** vector. As a result, more hot electrons are generated. Figures 149.30(c) and 149.30(d) compare the calculated signal level of ion-acoustic waves (IAW's), showing a stronger damping in CH compared to C because of the presence of light H ions. The calculated CE's into electrons with kinetic energy exceeding 50 keV from the PIC simulations were 12% and 2% for CH and C, respectively. A possible explanation is that the SRS saturation level is controlled by the secondary parametric decay or collapse of the driven plasma wave. The secondary parametric decay has
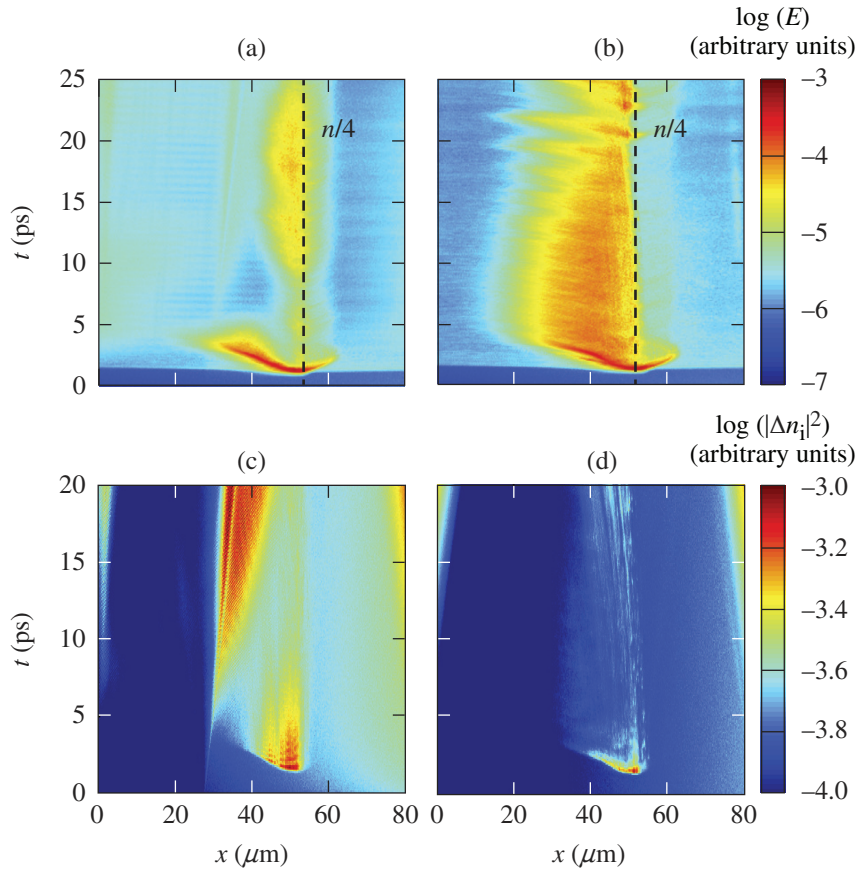
Figure 149.30
Calculated longitudinal electric field strength versus time and space (laser propagates from left to right) for (a) C and (b) CH and calculated ion-acoustic wave level for (c) C and (d) CH. The quantities were averaged over the transversal space coordinate and rendered on a logarithmic scale. The C simulation used a CH layer in the underdense portion, and the pure C layer starts at $x = 30~\mu$m.

E25859JR

been discussed in many papers; the experimental demonstration was reported in Ref. 36. The threshold of the parametric decay is proportional to the IAW damping rate. In the case of high IAW damping (with H), the threshold is higher and the plasma-wave amplitude can grow to a higher level, producing a stronger SRS signal and a larger number of hot electrons. Conversely, for a small IAW damping, the SRS is saturated by the EPW collapse at a lower level, producing large-scale density modulations and fewer hot electrons. It has been shown theoretically for a fixed T_e and density scale length that a high IAW damping rate promotes higher hot-electron generation;[20] also, theoretical work that studied the nonlinear saturation of SRS in laser hot spots linked an increased SRS reflectivity with a higher IAW damping rate.[37] The observed close correlation between SRS and hot-electron production indicates that IAW damping plays a major role in the CH plasma.

It is expected that the ablator material affects the ablation pressure in various ways. In general, thermal electron-heat conduction is lower in higher-Z materials, and we would expect a reduced mass ablation rate and lower ablation pressure. Based on a simple stationary laser ablation model[38] that neglects radiation and hot electrons, the ablation pressure from

thermal transport is given by $p_a = \rho_c^{1/3} I_{abs}^{2/3}$, where ρ_c is the critical mass density and I_{abs} is the absorbed laser intensity. Therefore, the ablation pressure $p_a \sim \left(\langle A \rangle / \langle Z_i \rangle\right)^{1/3}$ depends only weakly on the ratio of mass number and ionization degree for fixed laser wavelength and fixed I_{abs}. The expected increase in p_a from CH to Be is only ~7% and even less with respect to the other materials.[19] This experiment demonstrates higher ablation pressures for CH and SiO_2, however, indicating that other factors such as hot electrons and potentially radiation transport are more important. Higher-Z materials result in increased collisional absorption and a higher production of x-ray radiation. The radiation impinges deeper into the ablator layer than the thermal electrons, creating a double-ablation front for medium- and high-Z materials.[22,39]

In conclusion, the experiments demonstrate peculiar differences in hot-electron production in the various ablator materials—especially for CH, which generates the most electrons. PIC simulations using input parameters from radiation–hydrodynamic simulations reproduce the higher hot-electron production in CH. This is likely caused by a stronger damping of IAW's in the CH plasma because of the presence of light H ions.

ACKNOWLEDGMENT

REFERENCES

1. R. Betti, C. D. Zhou, K. S. Anderson, L. J. Perkins, W. Theobald, and A. A. Solodov, Phys. Rev. Lett. **98**, 155001 (2007).

2. W. Theobald, R. Betti, C. Stoeckl, K. S. Anderson, J. A. Delettrez, V. Yu. Glebov, V. N. Goncharov, F. J. Marshall, D. N. Maywar, R. L. McCrory, D. D. Meyerhofer, P. B. Radha, T. C. Sangster, W. Seka, D. Shvarts, V. A. Smalyuk, A. A. Solodov, B. Yaakobi, C. D. Zhou, J. A. Frenje, C. K. Li, F. H. Séguin, R. D. Petrasso, and L. J. Perkins, Phys. Plasmas **15**, 056306 (2008).

3. X. Ribeyre *et al.*, Plasma Phys. Control. Fusion **51**, 015013 (2009).

4. L. J. Perkins, R. Betti, K. N. LaFortune, and W. H. Williams, Phys. Rev. Lett. **103**, 045004 (2009).

5. S. Atzeni, X. Ribeyre, G. Schurtz, A. J. Schmitt, B. Canaud, R. Betti, and L. J. Perkins, Nucl. Fusion **54**, 054008 (2014).

6. D. Batani, S. Baton, A. Casner, S. Depierreux, M. Hohenberger, O. Klimo, M. Koenig, C. Labaune, X. Ribeyre, C. Rousseaux, G. Schurtz, W. Theobald, and V. T. Tikhonchuk, Nucl. Fusion **54**, 054009 (2014).

7. R. Betti and O. A. Hurricane, Nat. Phys. **12**, 435 (2016).

8. S. Gus'kov *et al.*, Phys. Rev. Lett. **109**, 255004 (2012); X. Ribeyre *et al.*, Phys. Plasmas **20**, 062705 (2013).

9. E. Llor Aisa *et al.*, Phys. Plasmas **22**, 102704 (2015).

10. Ph. Nicolaï *et al.*, Phys. Plasmas **22**, 042705 (2015).

11. A. Colaïtis *et al.*, Phys. Plasmas **23**, 072703 (2016).

12. R. Betti, W. Theobald, C. D. Zhou, K. S. Anderson, P. W. McKenty, S. Skupsky, D. Shvarts, V. N. Goncharov, J. A. Delettrez, P. B. Radha, T. C. Sangster, C. Stoeckl, and D. D. Meyerhofer, J. Phys.: Conf. Ser. **112**, 022024 (2008).

13. K. S. Anderson, R. Betti, P. W. McKenty, T. J. B. Collins, M. Hohenberger, W. Theobald, R. S. Craxton, J. A. Delettrez, M. Lafon, J. A. Marozas, R. Nora, S. Skupsky, and A. Shvydky, Phys. Plasmas **20**, 056312 (2013).

14. S. D. Baton *et al.*, Phys. Rev. Lett. **108**, 195002 (2012).

15. M. Hohenberger, W. Theobald, S. X. Hu, K. S. Anderson, R. Betti, T. R. Boehly, A. Casner, D. E. Fratanduono, M. Lafon, D. D. Meyerhofer, R. Nora, X. Ribeyre, T. C. Sangster, G. Schurtz, W. Seka, C. Stoeckl, and B. Yaakobi, Phys. Plasmas **21**, 022702 (2014).

16. D. Batani *et al.*, Phys. Plasmas **21**, 032710 (2014).

17. R. Nora, W. Theobald, R. Betti, F. J. Marshall, D. T. Michel, W. Seka, B. Yaakobi, M. Lafon, C. Stoeckl, J. A. Delettrez, A. A. Solodov, A. Casner, C. Reverdin, X. Ribeyre, A. Vallet, J. Peebles, F. N. Beg, and M. S. Wei, Phys. Rev. Lett. **114**, 045001 (2015).

18. W. Theobald, R. Nora, W. Seka, M. Lafon, K. S. Anderson, M. Hohenberger, F. J. Marshall, D. T. Michel, A. A. Solodov, C. Stoeckl, D. H. Edgell, B. Yaakobi, A. Casner, C. Reverdin, X. Ribeyre, A. Shvydky, A. Vallet, J. Peebles, F. N. Beg, M. S. Wei, and R. Betti, Phys. Plasmas **22**, 056310 (2015).

19. D. T. Michel, V. N. Goncharov, I. V. Igumenshchev, R. Epstein, and D. H. Froula, Phys. Rev. Lett. **111**, 245005 (2013).

20. J. F. Myatt, H. X. Vu, D. F. DuBois, D. A. Russell, J. Zhang, R. W. Short, and A. V. Maximov, Phys. Plasmas **20**, 052705 (2013).

21. S. X. Hu, D. T. Michel, D. H. Edgell, D. H. Froula, R. K. Follett, V. N. Goncharov, J. F. Myatt, S. Skupsky, and B. Yaakobi, Phys. Plasmas **20**, 032704 (2013).

22. S. Fujioka *et al.*, Phys. Plasmas **11**, 2814 (2004).

23. A. N. Mostovych, D. G. Colombant, M. Karasik, J. P. Knauer, A. J. Schmitt, and J. L. Weaver, Phys. Rev. Lett. **100**, 075002 (2008).

24. G. Fiksel, S. X. Hu, V. N. Goncharov, D. D. Meyerhofer, T. C. Sangster, V. A. Smalyuk, B. Yaakobi, M. J. Bonino, and R. Jungquist, Phys. Plasmas **19**, 062704 (2012).

25. M. Lafon, R. Betti, K. S. Anderson, T. J. B. Collins, R. Epstein, P. W. McKenty, J. F. Myatt, A. Shvydky, and S. Skupsky, Phys. Plasmas **22**, 032703 (2015).

26. T. R. Boehly, D. L. Brown, R. S. Craxton, R. L. Keck, J. P. Knauer, J. H. Kelly, T. J. Kessler, S. A. Kumpan, S. J. Loucks, S. A. Letzring, F. J. Marshall, R. L. McCrory, S. F. B. Morse, W. Seka, J. M. Soures, and C. P. Verdon, Opt. Commun. **133**, 495 (1997).

27. S. P. Regan, T. C. Sangster, D. D. Meyerhofer, W. Seka, R. Epstein, S. J. Loucks, R. L. McCrory, C. Stoeckl, V. Yu. Glebov, O. S. Jones, D. A. Callahan, P. A. Amendt, N. B. Meezan, L. J. Suter, M. D. Rosen, O. L. Landen, E. L. DeWald, S. H. Glenzer, C. Sorce, S. Dixit, R. E. Turner, and B. MacGowan, J. Phys.: Conf. Ser. **112**, 022077 (2008).

28. T. R. Boehly, V. A. Smalyuk, D. D. Meyerhofer, J. P. Knauer, D. K. Bradley, R. S. Craxton, M. J. Guardalben, S. Skupsky, and T. J. Kessler, J. Appl. Phys. **85**, 3444 (1999).

29. S. Skupsky, R. W. Short, T. Kessler, R. S. Craxton, S. Letzring, and J. W. Soures, J. Appl. Phys. **66**, 3456 (1989).

30. D. T. Michel, A. K. Davis, W. Armstrong, R. Bahr, R. Epstein, V. N. Goncharov, M. Hohenberger, I. V. Igumenshchev, R. Jungquist, D. D. Meyerhofer, P. B. Radha, T. C. Sangster, C. Sorce, and D. H. Froula, High Power Laser Science and Engineering **3**, e19 (2015).

31. J. Delettrez, R. Epstein, M. C. Richardson, P. A. Jaanimagi, and B. L. Henke, Phys. Rev. A **36**, 3926 (1987).

32. R. C. Malone, R. L. McCrory, and R. L. Morse, Phys. Rev. Lett. **34**, 721 (1975).

33. C. Stoeckl, R. E. Bahr, B. Yaakobi, W. Seka, S. P. Regan, R. S. Craxton, J. A. Delettrez, R. W. Short, J. Myatt, A. V. Maximov, and H. Baldis, Phys. Rev. Lett. **90**, 235002 (2003).

34. A. R. Christopherson, R. Betti, W. Theobald, C. J. Forrest, E. M. Campbell, J. Howard, J. A. Delettrez, C. Stoeckl, D. H. Edgell, W. Seka, V. Yu. Glebov, A. K. Davis, A. Bose, A. V. Maximov, M. S. Wei, and J. Peebles, "Direct Measurements of Hot-Electron Preheat in Inertial Confinement Fusion Implosions," to be submitted to Physical Review Letters.

35. R. A. Fonseca *et al.*, in *Computational Science—ICCS 2002*, edited by P. M. A. Sloot *et al.*, Lecture Notes in Computer Science (Springer, Berlin, 2002), Vol. 2331, pp. 342–351.

36. S. Depierreux *et al.*, Phys. Rev. Lett. **84**, 2869 (2000).

37. D. A. Russell, D. F. DuBois, and H. A. Rose, Phys. Plasmas **6**, 1294 (1999).

38. W. M. Manheimer, D. G. Colombant, and J. H. Gardner, Phys. Fluids **25**, 1644 (1982).

39. J. Sanz, R. Betti, V. A. Smalyuk, M. Olazabal-Loume, V. Drean, V. Tikhonchuk, X. Ribeyre, and J. Feugeas, Phys. Plasmas **16**, 082704 (2009).

Monochromatic Backlighting of Direct-Drive Cryogenic DT Implosions on OMEGA

Introduction

Layered cryogenic DT targets are the baseline approach to achieving ignition in direct-drive inertial confinement fusion (ICF) experiments.[1,2] Steady progress has been made in experiments with hydrodynamically equivalent,[3] energy-scaled implosions[4–9] on OMEGA.[10]

These implosions are designed to achieve similar peak shell velocities (v_{imp}), hot-spot convergence ratios (CR, the ratio of initial ice radius to hot-spot radius), and in-flight aspect ratios (IFAR's) as ignition designs. The IFAR is defined as the ratio of shell radius to shell thickness, given by the full width at $1/e$ density of the shell, when the shell has reached 2/3 of its initial radius. Recent direct-drive experiments on OMEGA[9] achieved record performance parameters that when scaled to the laser energy available at the National Ignition Facility (NIF), would achieve a Lawson parameter $P\tau \sim 60\%$ of the value required for ignition,[11] where P is the hot-spot pressure and τ is the confinement time. This scaled $P\tau$ is similar to the values achieved in indirect-drive implosions on the NIF.[12,13]

In these experiments the inferred hot-spot pressure P is ~40% lower than one-dimensional (1-D) simulations,[9] indicating that the experimental performance is significantly degraded. The current hypothesis to explain this performance degradation for implosions with an adiabat (α) > 3.5 (ratio of shell pressure to the Fermi pressure) is based on low-mode hydrodynamic instabilities.[8,9,14] These hydro-instabilities can be seeded by long-wavelength nonuniformites in the initial conditions, like ice-thickness variations,[5] target offset,[5,15] and laser-drive nonuniformity in space and time (target placement, beam pointing, power balance, and beam timing). Isolated defects like the target stalk,[16] debris on the target surface, or short-wavelength structures like target-surface roughness[17] or laser imprint,[15,18] especially for low-adiabat implosions (α < 3.5), can also seed these instabilities.

The performance of experiments with layered cryogenic DT targets has been measured using nuclear and x-ray self-emission diagnostics.[8,9] Recent three-dimensional (3-D) hydro simulations[14] have indicated that the x-ray self-emission images show the influence of long-wavelength nonuniformities on the hot core and do not observe the assembly of the cold shell. Figure 149.31 shows an equatorial density map from 3-D *ASTER* simulations[14] (a) at peak neutron production compared to (b) a simulated self-emission image from an orthogonal polar view in the 4- to 8-keV x-ray band at the same time. The comparison between the density map and a simulated x-ray image demonstrates that the shape of the x-ray image does not follow the density distribution in the shell.

X-ray backlighting can be used to observe the flow of the dense and relatively cold shell material in these cryo DT implosions. This technique has been used successfully in both direct-drive room-temperature experiments with gas-filled plastic (CH) targets[19] and in surrogate indirect-drive[20] ICF implosion experiments to measure the velocity and uniformity of the imploding shell. Figure 149.31(c) shows a simulated backlit image 50 ps before peak neutron production at CR ~ 12. The image is oriented so that the vertical is along the target offset direction. The image shows the absorption of the dense shell as a white ring and the self-emission of the core, which is seen as a darker central feature. The dominant effect from the offset, which will grow into a 5:1 density perturbation at peak compression, is clearly visible in the image and measurable in the lineout [Fig. 149.31(d)], even at this relatively modest convergence.

Direct-drive cryogenic DT implosions on OMEGA are difficult to radiograph because of the low opacity of the DT shell, the high shell velocity, the small size of the stagnating shell, and the very bright self-emission of the hot core. A shaped crystal imaging system with a Si backlighter driven by short (10- to 20-ps) laser pulses from OMEGA EP[21] was used to radiograph the OMEGA cryogenic implosions. It has the benefits of a narrow spectral width, high photon throughput, and a backlighter with a short emission time and high brightness. Processes with features below the spatial resolution of the imaging system, like mix, can be detected through the opacity effects from the carbon of the ablator material, which will significantly increase
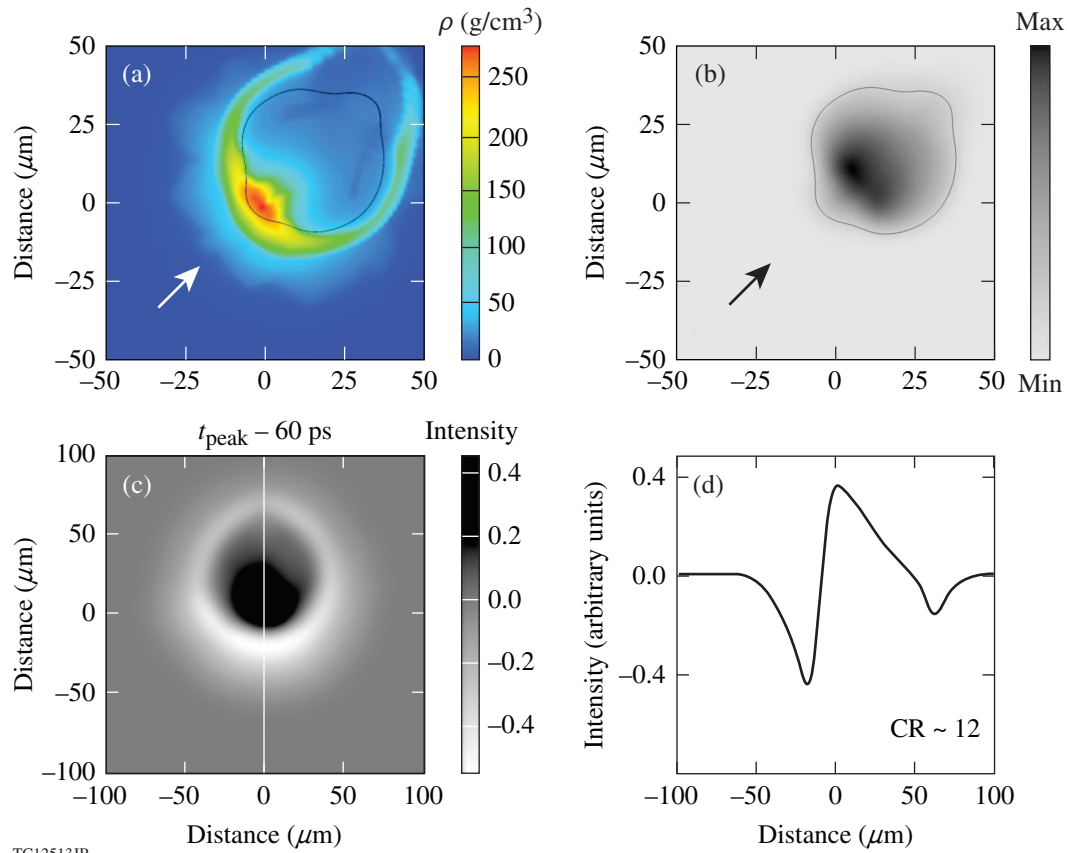
Figure 149.31

(a) Equatorial distributions of the density from a 3-D radiation–hydrodynamic simulation at peak neutron production taken from Ref. 14. (b) Simulated self-emission image from a polar view in the 4- to 8-keV x-ray band at the same time. The direction of the 20-μm target offset is indicated by an arrow. The thin black line in (b) shows the 17% contour of the maximum x-ray fluence. (c) A simulated backlit image 50 ps before peak neutron production at a convergence ratio (CR) ~ 12. The image is oriented so that the vertical is along the target offset direction. (d) Vertical lineout through the backlit image.

the absorption of the DT shell if mixing between the ablator and DT shell occurs.

The following sections (1) present the setup of the experiments, including a description of the narrowband crystal imaging system; (2) describe the experimental results in three subsections: (a) low-order modes, (b) stalk effects, and (c) mix; and (3) present our conclusions.

Experimental Setup

The cryogenic targets used in these experiments had an outer radius of ~430 to 480 μm. An ~8- to 12-μm-thick ablator shell of either plastic (CH), deuterated plastic (CD), or CD doped with 0.7% germanium encased a 50- to 75-μm-thick cryogenic DT ice layer [see Fig. 149.32(a)]. All targets were characterized using optical shadowgraphy and showed ice thickness variations of typically <1-μm root mean square (rms).[9] Triple-picket pulses of ~22- to 25-kJ laser energy were used to irradiate the

targets, with smoothing by distributed phase plates (DPP's);[22] polarization smoothing (PS) with birefringent wedges;[23] two-dimensional (2-D), three-color-cycle, 0.33-THz smoothing by spectral dispersion (SSD);[24,25] optimized energy balance (<4% beam-to-beam);[26] and optimized beam-to-beam timing of ~10-ps rms (Ref. 14). The targets were placed within ~10 μm of target chamber center.[14] The shape of the laser pulse was designed to put the shell on a specific adiabat that ranged from ~2 to 4 in these experiments. Figure 149.32(b) shows examples of both a lower- and a higher-adiabat pulse at comparable total laser energies. The high-adiabat pulses are shorter and have larger picket energies than the low-adiabat pulses. The total laser energy and the total shell mass determine the peak implosion velocity, which ranged from v_{imp} = 2.4 to 3.7 $\times 10^7$ cm/s. The IFAR ranged from 10 to 20 in these experiments. The IFAR is predominantly controlled by the shell thickness and shell adiabat.

(a)

Ablator

DT ice

8 to 12 μm

60 to 75 μm
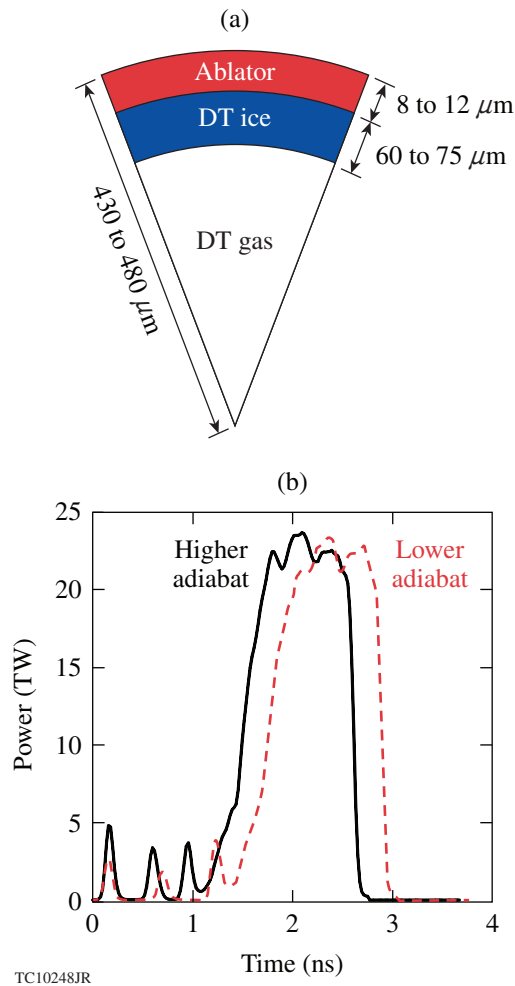
430 to 480 μm

DT gas

(b)

Figure 149.32

(a) The cryogenic DT capsules consist of a thin, 8- to 12-μm-thick CH, CD, or doped-CD ablator filled with several hundred atm of DT gas to create a 60- to 75-μm-thick ice layer at cryogenic temperatures below the triple point of DT (~19 K). (b) The laser drive pulse consists of a series of three pickets to establish the shell adiabat and control shock coalescence and a high-intensity main drive with a total energy of 22 to 25 kJ.

A shaped Bragg crystal-imaging system was used to obtain radiographs of the imploding targets at various convergence ratios. The OMEGA crystal-imaging radiography system[21] (see Fig. 149.33) uses a Si backlighter driven by the OMEGA EP laser to backlight implosion targets driven by the 60 beams of the OMEGA laser (not shown for clarity). A quartz crystal, cut along the 10$\bar{1}$1 planes for a 2d spacing of 0.6687 nm, was used for the Si He$_\alpha$ line at ~1.865 keV (0.664 nm). The Bragg angle for this configuration was 83.9°. The crystal was mounted by direct optical contact on an aspheric glass substrate by INRAD.[27] The crystal has a major radius of curvature of 500 mm and is placed 267 mm from the implosion target. The

image is recorded on a detector located ~3.65 m from the target, for a magnification of ~15×. The quartz crystal is rectangular with a size of 25 × 10 mm, resulting in f numbers of $f = 10$ in the horizontal and $f = 25$ in the vertical direction. The spectral bandwidth of the imager is of the order of 10 eV, which matches the typical broadened linewidth of the resonance line from the backlighter driven by a short-pulse laser.

The available solid angle for the backlighter foil is quite limited since the backlighter target must not intercept any of the 60 beams pointed at the implosion target. Because the backlighter laser intensity must be kept as high as possible, the 500-μm-sq backlighter was placed 5 mm from the implosion target. A fast target insertion system (FASTPOS) inserts the backlighter target 100 ms after the shroud that protects the layered cryogenic target from ambient thermal radiation has been removed. FASTPOS also acts as the direct line-of-sight (LOS) block. Two additional collimators are placed on the mounting structure for the FASTPOS to suppress background from Compton scattering and fluorescence from structures in the target chamber. To reduce the impact of the self-emission of the hot core of the cryo DT implosion, an x-ray framing-camera (XRFC) head[28] is used as a detector. The XRFC head is run with either a single-strip microchannel-plate (MCP) detector, with a 300- to 500-ps-long exposure, or a four-strip MCP with an exposure time of ~40 ps, where the backlit image is placed in the center of one of the four strips. The spatial resolution of the XRFC recording system is typically ~50 μm (Ref. 29). Experiments with resolution grids show an ~15-μm, 10% to 90% edge response for the crystal-imaging system. This spatial resolution is adequate for these initial experiments. Work is underway to improve the resolution to <10 μm. The XRFC is triggered by an ultrastable electro-optical trigger system with

Figure 149.33

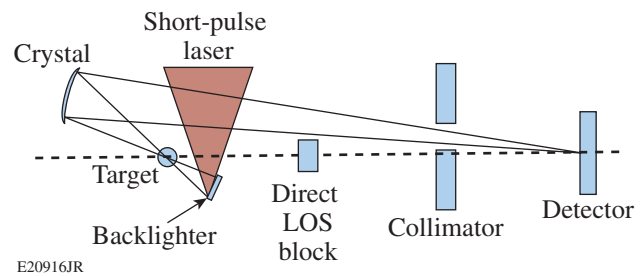Schematic of the spherical-crystal-imager backlighting setup from Ref. 21 (not to scale). The short-pulse laser illuminates a backlighter foil behind the primary target, which is heated by 60 beams from the OMEGA laser (not shown). A direct line-of-sight (LOS) block and a collimator protect the detector [an x-ray framing camera (XRFC)] from background x rays emitted by the backlighter and primary targets.

a jitter of ~1.5-ps rms. Experiments using only the backlighter foil showed that the XRFC system has a jitter of <10-ps rms with respect to the arrival of the OMEGA EP laser on the backlighter target. The timing of the OMEGA EP pulse to the OMEGA laser was measured to ~10-ps rms using the neutron temporal diagnostic (P11NTD),[30] which is also sensitive to the high-energy x rays produced during the interaction of the OMEGA EP laser with the backlighter target.

Figure 149.34(a) shows the temporal evolution of the implosion from 1-D *LILAC*[31] simulations close to peak compression compared to the laser pulse shape (blue line) for a typical backlit cryogenic implosion. All *LILAC* simulations shown in this article include the effects of cross-beam energy transfer (CBET)[32] and use a nonlocal thermal-conduction model.[6] The trajectory of the shell radius (peak density: green; $1/e$ of peak density: black) starts at the ~430-μm outer radius of the target and shows the shell moving toward the center until peak compression at ~3.5 ns. The neutron-production rate (orange) peaks ~40 ps before the calculated areal density (magenta). The exposure time of the XRFC is indicated by the gray-shaded area and the arrival time of the OMEGA EP short-pulse laser by the red vertical line. A time-gated image of a backlit DT cryogenic implosion with an exposure time of ~40 ps is shown in Fig. 149.34(b). The dashed white line indicates the original shell diameter, and the white line at the bottom of the image shows the location of the target stalk. The backlighter emission is shown in the center of the image. It is clipped at

the top of the XRFC slit because of a misalignment caused by repeatability issues in the crystal insertion mechanism. The absorption from the compressed shell is seen in the image as a ring-like feature around an emission feature from the central bright core of the implosion.

To measure the absorption in the compressed shell and to quantitatively compare the signal recorded by the crystal imager with simulations, the data must be corrected for the backlighter shape. A simple first-order physical model was constructed[21] to describe the shape of the backlighter by assuming a constant brightness source. This source was convolved with a Gaussian point-spread function (PSF), representing the spatial resolution of the imaging system at a 5-mm defocus. The brightness and extent of the source and the width of the PSF were varied to obtain a best fit to the shape of the measured signal outside the area affected by the absorption of the target. These uncertainties associated with correction are taken into account in the errors reported on the measured absorption.

Experimental Results
1. Low-Order Modes
  Long-wavelength nonuniformity can be seeded in an implosion by a number of processes including nonuniformities in the laser illumination, target placement, and thickness variations in both the ablator and the DT ice layer. To study the impact of these long-wavelength nonuniformities on the assembly of the compressed high-density shell close to stagnation, a series of

E25617JR
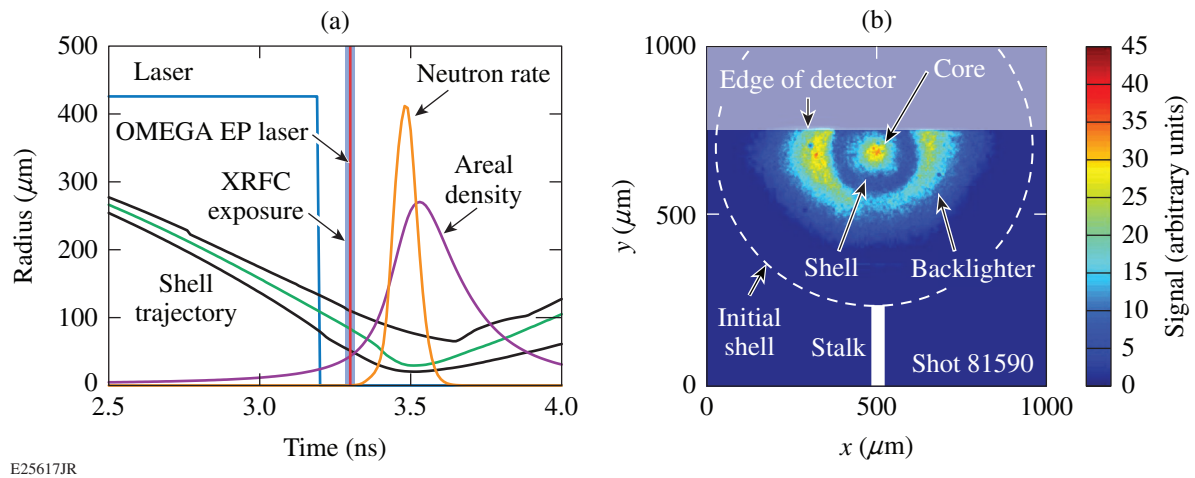
Figure 149.34
(a) Trajectory of the shell radius (center: green; inner, outer edge: black) compared to the temporal history of the laser power (blue) and neutron-production rate (orange) from 1-D *LILAC* simulations for the experiment shown in (b). The areal density evolution is shown for comparison (magenta). The exposure timing of the XRFC is indicated by the vertical gray area and the arrival time of the OMEGA EP short-pulse laser by the red vertical line. (b) Time-gated image of a backlit DT cryogenic implosion with an exposure time of ~40 ps. The initial shell radius and the location of the stalk are shown for comparison.

experiments were performed with preimposed initial-thickness perturbations in the CH shell.

Figure 149.35 illustrates a shaped target with preimposed initial-thickness perturbations in the CH shell. The amplitude of the variation in shell thickness was 2 to 4 μm peak to peak. This variation caused an ~2-μm–rms inner ice radius nonuniformity in the layering process. A fiducial glue spot of ~30-μm diameter was used to orient the target horizontally, i.e., perpendicular to the stalk that is mounted vertically in the target chamber. Standard-quality targets with an ablator-thickness nonuniformity of <0.1-μm rms in all modes and a DT ice layer nonuniformity of <1.0-μm rms were used in separate experiments to establish a reference.
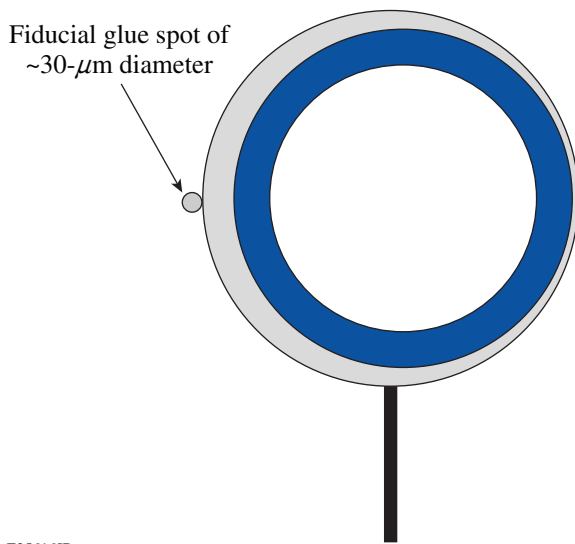
E25616JR

Figure 149.35
Illustration of a shaped target with a horizontal variation in CH shell thickness. The amplitude of this variation was 2 to 4 μm peak to peak. This variation caused an ~2-μm–rms nonuniformity in ice thickness. A fiducial glue spot of ~30-μm diameter was used to orient the targets with respect to the stalk.

The radiograph from the reference experiment with a standard-quality target (shot 81590) from Fig. 149.34(b) is shown on an expanded scale in Fig. 149.36(a). The image was recorded at ~100 ps before peak neutron production at a CR of 7, with an exposure time of ~40 ps. The absorption of the backlighter by the compressed shell is seen in the image as a ringlike feature around a central emission feature from the bright core of the implosion. The initial CH ablator thickness of the target was ~12 μm, with an outer diameter of ~890 μm. The measured nonuniformity of the outer surface was 0.24-μm rms. The thickness of the DT ice layer was measured at ~61 μm with a 0.5-μm–rms thickness variation. The target was imploded
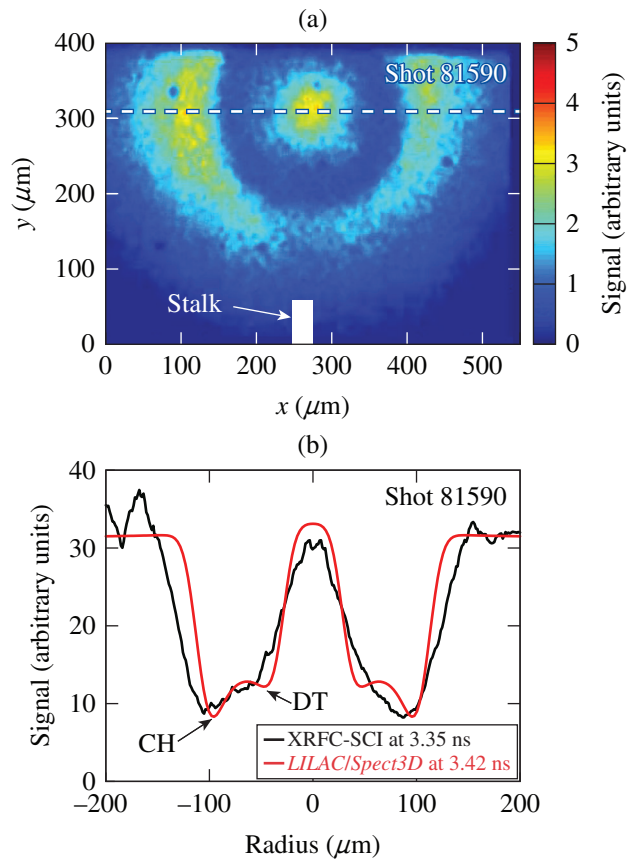
E25618JR

Figure 149.36
(a) Backlit image of cryogenic implosion (shot 81590). (b) Backlighter shape–corrected horizontal lineout compared to *Spect3D* post-processed, 1-D *LILAC* simulations.

with a triple-picket pulse of 24-kJ energy at a calculated adiabat of ~2.5, which led to a calculated IFAR = 10. The measured offset from target chamber center at shot time was <10 μm. The recorded yield was 20% of the 1-D calculations [yield over clean (YOC)] and the measured areal density was ~80% of the predictions.

Figure 149.36(b) shows the backlighter shape–corrected horizontal lineout of the radiograph in Fig. 149.36(a) compared to *Spect3D*[33] post-processed, 1-D *LILAC* simulations. The backlighter intensity was adjusted to match the observed ratio of the backlighter relative to the level of self-emission of the core. The measured spatial resolution of the imager of ~15 μm was taken into account in the *Spect3D* postprocessing. The simulated lineout matches the experiment quite closely in both size and magnitude of the absorption. The most-noticeable difference between experiment and simulation is that the slopes of the signal at the interface between shell and core and at the outside of the shell are significantly steeper in the simulation.

To further analyze the radiographs and to obtain quantitative data on the shape of the compressed shell, radial lineouts were taken from the center of the self-emission peak and the radius of peak absorption and its magnitude were evaluated as a function of azimuthal angle (see Fig. 149.37). The contour at $1/e$ of the peak of the core emission is also determined and plotted in Fig. 149.37(a) for comparison. The errors shown in the graph are estimates of the uncertainty determining the peak absorption location or the $1/e$ of the emission given the signal/noise on the experimental signal. The radius of peak absorption shows predominantly an $\ell = 1$ feature of ~10-μm amplitude, with a small extra feature at 180° azimuthal angle, which is associated with the stalk (see **Stalk Effects**, p. 42). Within the errors of the evaluation, the $1/e$ contour of the core self-emission is observed to be circular. The magnitude of peak absorption shows a small ~±5% peak-to-peak variation as a function of angle.

A radiograph obtained in an experiment using a shaped target with a 4-μm peak-to-peak variation in the CH ablator wall thickness (shot 82717) is shown in Fig. 149.38(a). The image was recorded at a CR = 10, ~50 ps before peak neutron production. The gate time of the XRFC was ~40 ps. Because of drifts in the OMEGA EP beam pointing, the registration between the backlighter emission and the implosion is not as good as it was for shot 81590. Nevertheless, the absorption feature from the compressed shell is clearly visible. Since the image was recorded ~50 ps closer to peak neutron production and at peak x-ray emission, the emission of the central core is brighter than in the shot shown in Fig. 149.36. The target had an outer diameter of ~960 μm with an initial CH ablator thickness of ~11 μm. The measured total variation in the radius of the inner DT ice layer was ~2-μm rms and its thickness was ~63 μm. The nonuniformity of the outer surface radius was 0.21-μm rms. The target was irradiated with a triple-picket

Figure 149.37
(a) Radius of peak absorption as a function of angle obtained by evaluating lineouts taken from the center of the self-emission peak. The $1/e$ radius contour from the self-emission is shown for comparison. (b) Peak absorption as a function of angle.

Figure 149.38
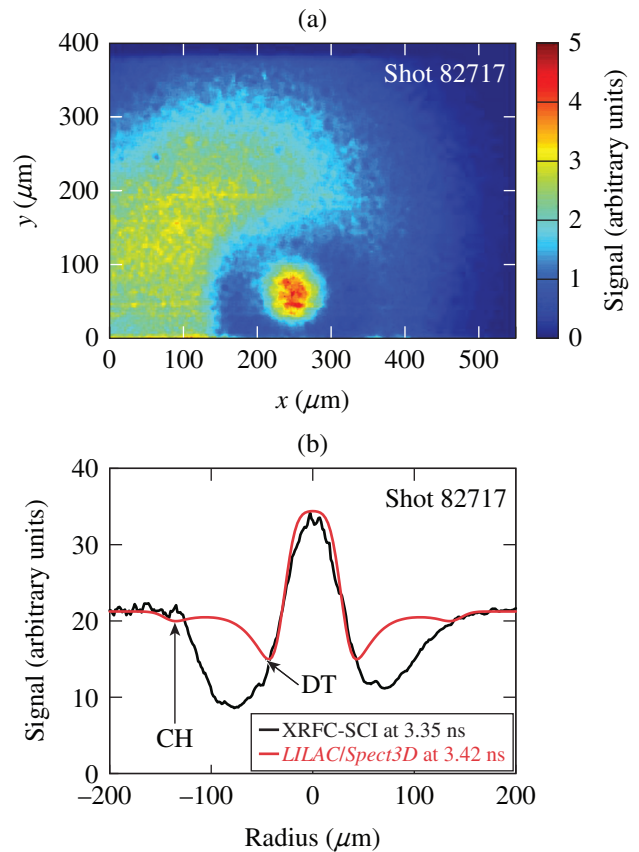(a) Backlit image of cryogenic implosion shot 82717 using a shaped target with a 4-μm variation in peak-to-peak CH shell thickness. (b) Backlighter shape–corrected horizontal lineout compared to *Spect3D* post-processed 1-D *LILAC* simulations.

pulse of 25-kJ energy at a calculated adiabat of ~2.0. The calculated IFAR was 14. The measured offset from target chamber center at shot time was <10 μm. The observed YOC was 8% and the measured areal density was ~40% of the calculated value.

Figure 149.38(b) shows the backlighter shape–corrected horizontal lineout of the radiograph in Fig. 149.38(a) compared to *Spect3D* post-processed, 1-D *LILAC* simulations, where the backlighter intensity was adjusted to match the observed self-emission of the core. The simulated lineout does not match the experiment quite as well as it did for the comparison shot 81590. While the shape of the self-emission peak is reproduced quite well, the absorption feature from the compressed shell is significantly underestimated. The experimental lineout shows a significant left–right asymmetry, which is consistent with the initial placement of the target, where the thicker side of the CH ablator is placed on the left side of the image shown in Fig. 149.34(a).

The radius of peak absorption and its magnitude are evaluated again as a function of azimuthal angle, together with the contour at 1/e of the peak of the core emission (see Fig. 149.39). The radius of peak absorption shows a feature of ~20-μm amplitude. Clipping on the XRFC strip caused by the pointing instability of the crystal-insertion mechanism made it impossible to extract data in the stalk region around the 180° azimuthal angle. The 1/e contour of the core self-emission shows a measurable ℓ = 2 variation with an amplitude of ~7 μm. A much larger perturbation in the magnitude of peak absorption as a function of an angle of ~±20% is observed with the shaped shell compared to the reference shell.

The backlit images show that even for the reference implosion without any preimposed nonuniformity, deviations from a spherical shell assembly can be seen. Additionally, the fact that the interfaces between shell and core and at the outside of the shell are significantly steeper in the simulation indicates that there is probably small-scale mixing occurring in the deceleration phase that cannot be spatially resolved with the imager and therefore is visible only in the change of the gradients compared to the 1-D simulations. The radiograph for the reference implosion also shows that the shape of the dense shell where a significant ℓ = 1 perturbation is visible, does not necessarily correspond to the shape of the hot spot, which is seen to be round.

The images from the experiments using targets with preimposed CH ablator thickness variations show much larger perturbations than the reference implosion, both in the radius and magnitude of peak absorptions. The lineouts show significantly more absorption over a larger radius than the post-processed 1-D simulation, indicating more mixing between the ablator CH and the DT ice layer. Even though the targets and laser pulses are quite similar, the small differences in both the adiabat and the IFAR lead to significant differences in the shape of the absorption features as compared to simulations.

2. Stalk Effects

The impact of the target stalk and the glue spot, with which the stalk is attached to the shell, on the implosion symmetry has been observed previously using the crystal-imaging system in an implosion experiment with a mass-equivalent CH target fielded from the cryo target insertion system.[21] At a conver-
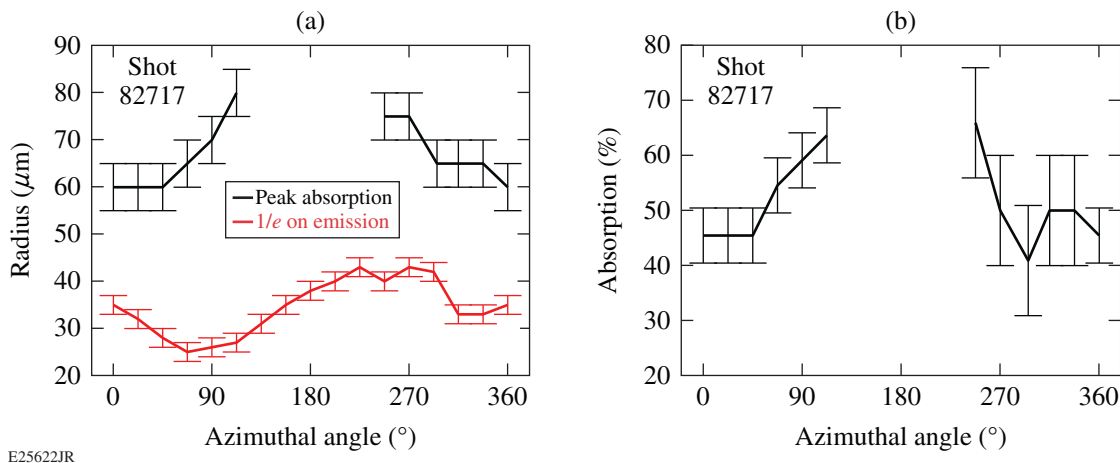

Figure 149.39

(a) Radius of peak absorption as a function of angle obtained by evaluating lineouts taken from the center of the self-emission peak. The 1/e radius contour from the self-emission is shown for comparison. (b) Peak absorption as a function of angle.

gence of 2.5, the image revealed a cusp-like feature in the shell radius at the location of the stalk. Figure 149.40(a) shows the shell radius as a function of azimuthal angle, evaluated at the 50% point on the absorption feature seen in the backlit image of the mass-equivalent CH target (shot 69789). The target had a shell thickness of 24 μm and was irradiated with 23 kJ of laser energy. The evaluation shows a narrow feature of ~25-μm amplitude at the stalk location at 180° azimuthal angle. At the stalk feature, the shell radius is larger than the average shell radius.
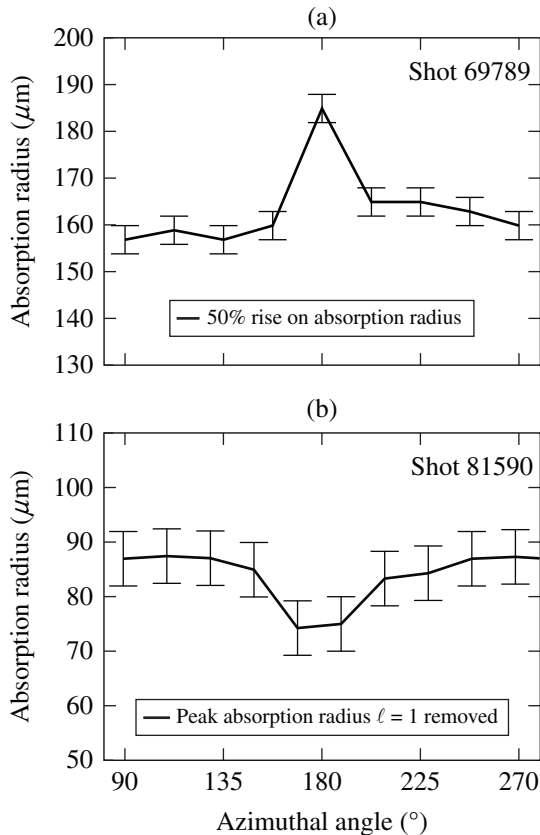
Figure 149.40
(a) Shell radius as a function of angle, inferred from the 50% point on the absorption feature seen in the backlit image of a CH target mass equivalent to a cryo target as shown in Ref. 20 (shot 69789). (b) Radius of peak absorption as a function of angle, obtained by taking lineouts from the center of the image from the cryo implosion shown in Fig. 149.35 (shot 81590). An $\ell = 1$ mode of 10-μm amplitude was removed to show the effect of the stalk more clearly.

Figure 149.40(b) shows the radius of peak absorption as a function of angle at a convergence of 7, obtained by taking lineouts from the center of the image from the cryo implosion shown in Fig. 149.35 (shot 81590). An $\ell = 1$ mode of 10-μm amplitude was removed to show the effect of the stalk more clearly. The radius of peak absorption shows a relatively wide feature of ~45° extent in azimuthal angle and an amplitude of ~10 μm. In this case the shell radius is smaller at the stalk feature than the average shell radius.

The change in direction of the stalk perturbation from being larger than the average radius at CR = 2.5 during the acceleration phase to being smaller than the average radius at CR = 7 during the deceleration phase is expected based on an analysis of multidimensional hydro simulations. During acceleration, the stalk area lags behind the rest of the shell because the extra mass of the glue and the shadowing of the laser drive by the stalk reduce the shell velocity. During deceleration, the extra mass at the stalk location causes it to decelerate more slowly against the growing pressure of the core, allowing it to push farther in compared to the rest of the shell.

3. Imprint and Mix

The images from most cryogenic DT target experiments show significantly more contrast than expected from *Spect3D* post-processed *LILAC* simulations, which indicates that carbon from the ablator mixes into the DT ice layer.

Figure 149.41 shows a lineout through the image of shot 70535 corrected for the backlighter shape. A 300-ps gate was used in these experiments and was timed to start ~500 ps before the calculated time of peak core emission, according to 1-D *LILAC* hydrocode simulations. The OMEGA EP short-pulse laser was fired ~100 ps before the end of the gate at a time when the shell assembly was compressed to an inner radius of ~90 μm, which translates to a convergence of ~4, given an inner ice shell radius of ~380 μm. The calculated areal density of the DT at this convergence was ~14 mg/cm^2 with an adiabat of 2.5. The simulations show an IFAR = 12 for this implosion.

The result from a 1-D *LILAC* simulation, post-processed with the radiation-transport code *Spect3D*, is plotted for comparison on the left side of the experimental lineout (green line). The backlighter timing had to be shifted ~50 ps earlier to match the measured size of the absorption feature, indicating that the implosion was slightly delayed compared to the simulations. The timing of the OMEGA EP laser during these experiments was not as well controlled as it was for the shots with the 40-ps-exposure-time framing camera and had a jitter of the order of 20-ps rms. The measured absorption was much higher than the absorption calculated from the simulations. One possible explanation for this discrepancy is Rayleigh–Taylor mixing of carbon from the outer CD shell into the DT ice during the shell acceleration. Adding a small amount of carbon
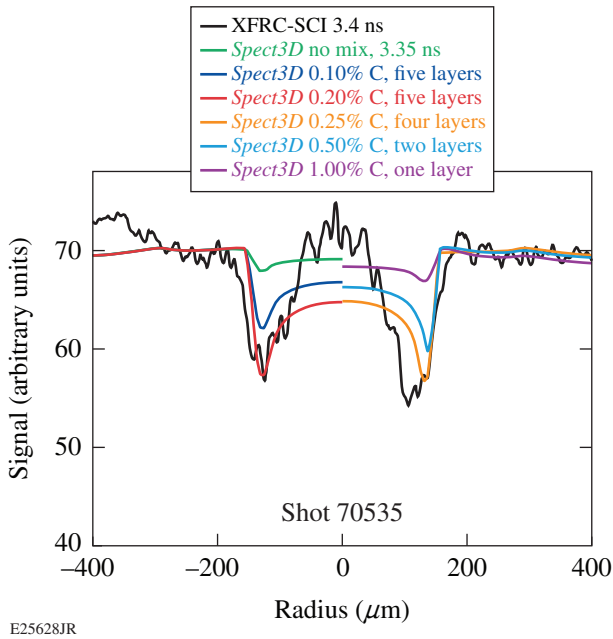
Figure 149.41

Backlighter shape–corrected lineout through the radiograph of a cryogenic target shown in Ref. 21 (black line) compared to a *Spect3D* post-processed *LILAC* simulation (colored lines). In the simulation the DT ice was split into five layers and C was uniformly mixed into these layers. The left side of the image shows that simulations with a uniform mix of 0.2% C into the DT match the experimental data (green, blue, and red lines). The right side of the image shows results from simulations where the same mass of C is added to the DT, penetrating into more and more layers (magenta, cyan, orange), showing that at least four layers must be mixed for and adequately matched to the experimental data.

uniformly into the shell in the *Spect3D* postprocessor [0.1% C (blue line), 0.2% C (red line)] significantly increases the absorption in the model and brings the simulation much closer to the experimental data, especially in the areas of highest absorption corresponding to the dense shell. In the center of the image, the calculated absorption with carbon mixing is higher than observed. This is probably caused by a small amount of self-emission, which is not fully suppressed by the gating.

To estimate the depth of the mixing of the carbon into the DT, the DT shell was split into five regions of equal thickness in the 1-D *LILAC* simulations. An equivalent mass of 0.2% C (atomic) was mixed either into the full DT shell or in the outer one, two, or four layers in the *Spect3D* postprocessor. The results from *Spect3D* are shown on the right side of Fig. 149.41. The one-layer simulations (magenta) show almost the same absorption as the unmixed simulations, indicating that the outermost 20% of the DT ice has already ablated at the time the radiograph was recorded, consistent with the predictions from

the 1-D *LILAC* simulations. The two-layer simulation (cyan) shows significantly more absorption but still does not match the experiment. Even the four-layer absorption does not compare as well to the experiment as the fully mixed data, indicating that the carbon is most probably fully mixed throughout the DT shell.

Figure 149.42 shows backlighter shape–corrected lineouts through the radiographs from two additional cryogenic target experiments compared to *Spect3D* post-processed *LILAC* simulations. The lineouts show only one side of the implosion because they could not be corrected for the backlighter shape resulting from a significant misalignment of the backlighter.
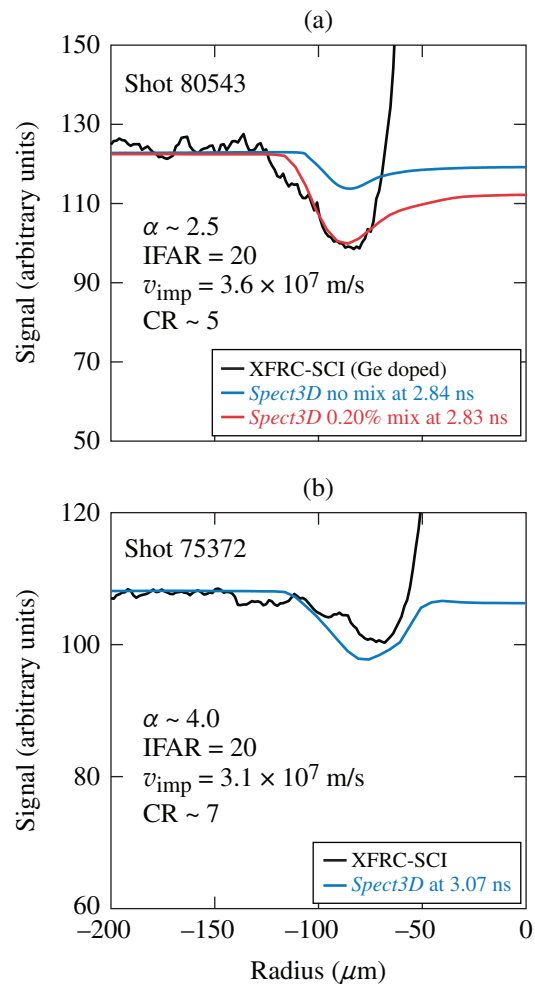

Figure 149.42

Backlighter shape–corrected lineouts through the radiographs from two cryogenic target experiments compared to *Spect3D* post-processed *LILAC* simulations. Mixing of ablator material is required to match the experimental data for a Ge-doped low-adiabat ($\alpha = 2.5$) shot (80543) but not for a high-adiabat ($\alpha = 4.0$) implosion (75372).

The target in shot 80543 had an 8-μm CD shell doped with 0.7% Ge (atomic) and a 50-μm-thick DT ice layer. It was imploded with 25 kJ of laser energy using a pulse that set the calculated adiabat of the shell to 2.5. Preheat from the Ge dopant caused the adiabat to rise to 3.5 at the end of the laser pulse. The IFAR of the shell was calculated to be 20. The radiograph was taken with a 40-ps-wide gate, ~150 ps before peak neutron production at a CR = 5 and a predicted areal density of ~40mg/cm^2. Shot 75372 used a target with a 7-μm pure CD shell without any dopant and a 75-μm-thick DT ice layer. It was imploded with 23 kJ of laser energy with a calculated shell adiabat of 4. The calculated IFAR was 20. The radiograph was recorded with a 200-ps XRFC gate, 150 ps before bang time at a CR = 7 and a predicted areal density of ~40 mg/cm^2.

Mixing of ablator material at a level of ~0.2% is required to match the experimental data for the low-adiabat, Ge-doped shot (80543), similar to the mix observed in the low-adiabat, pure-CD shot (70535). No indication of mixing is observed in the higher-adiabat implosion (75372). In both radiographs, strong self-emission from the core is observed.

The radiography data show that the most important parameter controlling the mix from the CH/CD outer shell into the ice seems to be the adiabat since even a stable, very low IFAR = 10 implosion (70535) shows significant mix throughout the DT quite early in the implosion at the end of the acceleration phase, well before the onset of deceleration of the shell. Two similar IFAR = 20 implosions show a mix threshold in adiabat at around $\alpha = 4$. The magnitude of the mixing appears to be quite small (~0.2%), which is most likely due to the fact that the DT is starting to be ablated quite early in the implosion. The analysis using five layers for shot 70535 shows that at least the outer 20% of the DT shell gets ablated before the end of the acceleration phase. This ablated DT could serve as a buffer between the CD and the dense DT shell that limits the mix.

Conclusions

X-ray backlighting has been used to radiograph the compressed shell in implosion experiments with layered cryogenic DT targets on OMEGA at convergence ratios from 4 to 10. A shaped-crystal-imaging system with a Si backlighter driven by short laser pulses from OMEGA EP has been set up for this challenging radiography configuration.

The effects of long-wavelength nonuniformities on the shell assembly close to stagnation have been studied in an experiment with preimposed initial thickness perturbations in the CH shell. The radiograph from the reference implosion without any

preimposed modulations shows a significant $\ell = 1$ perturbation in the shape of the dense shell, which does not match the shape of the hot spot. Additionally, indications of small-scale mixing are observed at the interfaces between ablator, DT shell, and the hot core. The images from targets with preimposed thickness variations show much larger perturbations than the reference implosion, in both the radius and magnitude of peak absorptions and significantly more mixing between the ablator CH and the DT ice layer.

The impact of the target stalk and the glue spot—with which the shell is attached to the stalk—on the implosion symmetry has been observed in both mass-equivalent CH targets and layered DT cryo targets. As expected from simulations, the stalk area lags behind the rest of the shell in the acceleration phase because the extra mass of the glue and the shadow from the stalk reduce the shell velocity and push in farther during the deceleration phase because of the extra mass at the stalk location.

The experimental data show that the most important parameter controlling the mix from the CH/CD outer shell into the ice is the adiabat. A threshold in adiabat at around $\alpha = 4$ has been observed, where mix is below the detection threshold of 0.02%. The magnitude of the mixing appears to be quite small at ~0.2%, which is most likely caused by the fact that the DT is starting to be ablated quite early in the implosion, thereby serving as a buffer between the CD and the dense DT shell, which could limit the amount of mix.

Future experiments will use this radiography technique to separate the performance degradation from different sources of nonuniformity, such as target offset and laser energy imbalance, and the experimental data will be compared with detailed multidimensional hydrocode calculations. A project has been started that will improve the spatial resolution of the shaped crystal imager and increase the brightness of the backlighter in order to radiograph the implosions at a higher convergence closer to peak neutron production. To illustrate the benefit from higher spatial resolution, radial lineouts from *Spect3D* post-processed *LILAC* simulations of cryogenic implosions at a convergence ratio of CR = 16 are shown in Fig. 149.43 using either (a) a measured spatial resolution of ~15 μm or (b) an improved resolution of 8 μm. The green lines show the absorption of the DT and CH shell, the red lines show the self-emission from the core, and the black lines show the combination of both effects. With the lower resolution of ~15 μm, the location of the minimum absorption feature from the DT shell with self-emission, indicated by the black arrows in (a) and (b), is seen at a significantly different radius than the mini-
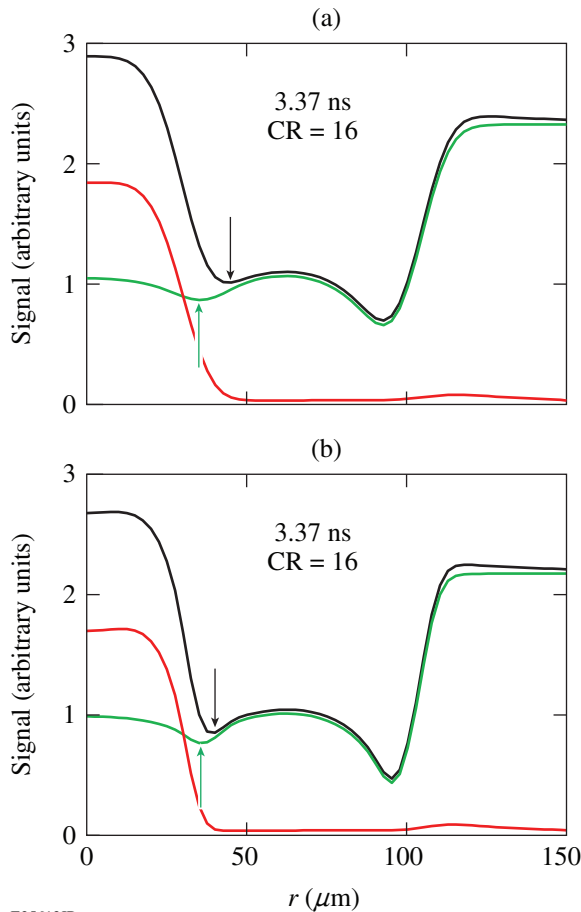
E25613JR

Figure 149.43
Radial lineouts from *Spect3D* post-processed *LILAC* simulations of cryogenic implosions at a convergence ratio of 16 using (a) a measured spatial resolution of ~15 μm and (b) an improved resolution of 8 μm. The green lines show the absorption of the DT and CH shell, the red lines show the self-emission from the core, and the black lines show the combination of both effects. The black arrows in (a) and (b) indicate the location of the minimum absorption feature from the DT shell with self-emission; the green arrows indicate the minimum absorption without self-emission.

mum absorption without self-emission, indicated by the green arrows. This discrepancy is reduced at the higher resolution of 8 μm, which will allow one to more-accurately determine the location of the dense DT in the presence of self-emission.

REFERENCES

1. R. S. Craxton, K. S. Anderson, T. R. Boehly, V. N. Goncharov, D. R. Harding, J. P. Knauer, R. L. McCrory, P. W. McKenty, D. D. Meyerhofer, J. F. Myatt, A. J. Schmitt, J. D. Sethian, R. W. Short, S. Skupsky, W. Theobald, W. L. Kruer, K. Tanaka, R. Betti, T. J. B. Collins, J. A. Delettrez, S. X. Hu, J. A. Marozas, A. V. Maximov, D. T. Michel, P. B. Radha, S. P. Regan, T. C. Sangster, W. Seka, A. A. Solodov, J. M. Soures, C. Stoeckl, and J. D. Zuegel, Phys. Plasmas **22**, 110501 (2015).

2. V. N. Goncharov, S. P. Regan, E. M. Campbell, T. C. Sangster, P. B. Radha, J. F. Myatt, D. H. Froula, R. Betti, T. R. Boehly, J. A. Delettrez, D. H. Edgell, R. Epstein, C. J. Forrest, V. Yu. Glebov, D. R. Harding, S. X. Hu, I. V. Igumenshchev, F. J. Marshall, R. L. McCrory, D. T. Michel, W. Seka, A. Shvydky, C. Stoeckl, W. Theobald, and M. Gatu-Johnson, Plasma Phys. Control. Fusion **59**, 014008 (2017).

3. V. N. Goncharov, T. C. Sangster, R. Betti, T. R. Boehly, M. J. Bonino, T. J. B. Collins, R. S. Craxton, J. A. Delettrez, D. H. Edgell, R. Epstein, R. K. Follet, C. J. Forrest, D. H. Froula, V. Yu. Glebov, D. R. Harding, R. J. Henchen, S. X. Hu, I. V. Igumenshchev, R. Janezic, J. H. Kelly, T. J. Kessler, T. Z. Kosc, S. J. Loucks, J. A. Marozas, F. J. Marshall, A. V. Maximov, R. L. McCrory, P. W. McKenty, D. D. Meyerhofer, D. T. Michel, J. F. Myatt, R. Nora, P. B. Radha, S. P. Regan, W. Seka, W. T. Shmayda, R. W. Short, A. Shvydky, S. Skupsky, C. Stoeckl, B. Yaakobi, J. A. Frenje, M. Gatu-Johnson, R. D. Petrasso, and D. T. Casey, Phys. Plasmas **21**, 056315 (2014).

4. C. Stoeckl, C. Chiritescu, J. A. Delettrez, R. Epstein, V. Yu. Glebov, D. R. Harding, R. L. Keck, S. J. Loucks, L. D. Lund, R. L. McCrory, P. W. McKenty, F. J. Marshall, D. D. Meyerhofer, S. F. B. Morse, S. P. Regan, P. B. Radha, S. Roberts, T. C. Sangster, W. Seka, S. Skupsky, V. A. Smalyuk, C. Sorce, J. M. Soures, R. P. J. Town, J. A. Frenje, C. K. Li, R. D. Petrasso, F. H. Séguin, K. Fletcher, S. Padalino, C. Freeman, N. Izumi, R. Lerche, and T. W. Phillips, Phys. Plasmas **9**, 2195 (2002).

5. F. J. Marshall, R. S. Craxton, J. A. Delettrez, D. H. Edgell, L. M. Elasky, R. Epstein, V. Yu. Glebov, V. N. Goncharov, D. R. Harding, R. Janezic, R. L. Keck, J. D. Kilkenny, J. P. Knauer, S. J. Loucks, L. D. Lund, R. L. McCrory, P. W. McKenty, D. D. Meyerhofer, P. B. Radha, S. P. Regan, T. C. Sangster, W. Seka, V. A. Smalyuk, J. M. Soures, C. Stoeckl, S. Skupsky, J. A. Frenje, C. K. Li, R. D. Petrasso, and F. H. Séguin, Phys. Plasmas **12**, 056302 (2005).

6. V. N. Goncharov, T. C. Sangster, P. B. Radha, R. Betti, T. R. Boehly, T. J. B. Collins, R. S. Craxton, J. A. Delettrez, R. Epstein, V. Yu. Glebov, S. X. Hu, I. V. Igumenshchev, J. P. Knauer, S. J. Loucks, J. A. Marozas, F. J. Marshall, R. L. McCrory, P. W. McKenty, D. D. Meyerhofer, S. P. Regan, W. Seka, S. Skupsky, V. A. Smalyuk, J. M. Soures, C. Stoeckl, D. Shvarts, J. A. Frenje, R. D. Petrasso, C. K. Li, F. Séguin, W. Manheimer, and D. G. Colombant, Phys. Plasmas **15**, 056310 (2008).

7. T. C. Sangster, V. N. Goncharov, R. Betti, T. R. Boehly, D. T. Casey, T. J. B. Collins, R. S. Craxton, J. A. Delettrez, D. H. Edgell, R. Epstein, K. A. Fletcher, J. A. Frenje, V. Yu. Glebov, D. R. Harding, S. X. Hu, I. V. Igumenshchev, J. P. Knauer, S. J. Loucks, C. K. Li, J. A. Marozas, F. J. Marshall, R. L. McCrory, P. W. McKenty, D. D. Meyerhofer, P. M. Nilson, S. P. Padalino, R. D. Petrasso, P. B. Radha, S. P. Regan, F. H. Seguin, W. Seka, R. W. Short, D. Shvarts, S. Skupsky, V. A. Smalyuk, J. M. Soures, C. Stoeckl, W. Theobald, and B. Yaakobi, Phys. Plasmas **17**, 056312 (2010).

8. T. C. Sangster, V. N. Goncharov, R. Betti, P. B. Radha, T. R. Boehly, D. T. Casey, T. J. B. Collins, R. S. Craxton, J. A. Delettrez, D. H. Edgell, R. Epstein, C. J. Forrest, J. A. Frenje, D. H. Froula, M. Gatu-Johnson, V. Yu. Glebov, D. R. Harding, M. Hohenberger, S. X. Hu, I. V. Igumenshchev, R. Janezic, J. H. Kelly, T. J. Kessler, C. Kingsley, T. Z. Kosc, J. P. Knauer, S. J. Loucks, J. A. Marozas, F. J. Marshall, A. V. Maximov, R. L. McCrory, P. W. McKenty, D. D. Meyerhofer, D. T. Michel, J. F. Myatt, R. D. Petrasso, S. P. Regan, W. Seka, W. T. Shmayda, R. W. Short, A. Shvydky, S. Skupsky, J. M. Soures, C. Stoeckl, W. Theobald, V. Versteeg, B. Yaakobi, and J. D. Zuegel, Phys. Plasmas **20**, 056317 (2013).

9. S. P. Regan, V. N. Goncharov, I. V. Igumenshchev, T. C. Sangster, R. Betti, A. Bose, T. R. Boehly, M. J. Bonino, E. M. Campbell, D. Cao, T. J. B. Collins, R. S. Craxton, A. K. Davis, J. A. Delettrez, D. H. Edgell, R. Epstein, C. J. Forrest, J. A. Frenje, D. H. Froula, M. Gatu Johnson, V. Yu. Glebov, D. R. Harding, M. Hohenberger, S. X. Hu, D. Jacobs-Perkins, R. T. Janezic, M. Karasik, R. L. Keck, J. H. Kelly, T. J. Kessler, J. P. Knauer, T. Z. Kosc, S. J. Loucks, J. A. Marozas, F. J. Marshall, R. L. McCrory, P. W. McKenty, D. D. Meyerhofer, D. T. Michel, J. F. Myatt, S. P. Obenschain, R. D. Petrasso, R. B. Radha, B. Rice, M. Rosenberg, A. J. Schmitt, M. J. Schmitt, W. Seka, W. T. Shmayda, M. J. Shoup III, A. Shvydky, S. Skupsky, S. Solodov, C. Stoeckl, W. Theobald, J. Ulreich, M. D. Wittman, K. M. Woo, B. Yaakobi, and J. D. Zuegel, Phys. Rev. Lett. **117**, 025001 (2016); **117**, 059903(E) (2016).

10. T. R. Boehly, D. L. Brown, R. S. Craxton, R. L. Keck, J. P. Knauer, J. H. Kelly, T. J. Kessler, S. A. Kumpan, S. J. Loucks, S. A. Letzring, F. J. Marshall, R. L. McCrory, S. F. B. Morse, W. Seka, J. M. Soures, and C. P. Verdon, Opt. Commun. **133**, 495 (1997).

11. A. Bose, K. M. Woo, R. Betti, E. M. Campbell, D. Mangino, A. R. Christopherson, R. L. McCrory, R. Nora, S. P. Regan, V. N. Goncharov, T. C. Sangster, C. J. Forrest, J. Frenje, M. Gatu Johnson, V. Yu. Glebov, J. P. Knauer, F. J. Marshall, C. Stoeckl, and W. Theobald, Phys. Rev. E **94**, 011201(R) (2016).

12. O. A. Hurricane *et al.*, Nature **506**, 343 (2014).

13. R. Betti, A. R. Christopherson, B. K. Spears, R. Nora, A. Bose, J. Howard, K. M. Woo, M. J. Edwards, and J. Sanz, Phys. Rev. Lett. **114**, 255003 (2015).

14. I. V. Igumenshchev, V. N. Goncharov, F. J. Marshall, J. P. Knauer, E. M. Campbell, C. J. Forrest, D. H. Froula, V. Yu. Glebov, R. L. McCrory, S. P. Regan, T. C. Sangster, S. Skupsky, and C. Stoeckl, Phys. Plasmas **23**, 052702 (2016).

15. S. X. Hu, V. N. Goncharov, P. B. Radha, J. A. Marozas, S. Skupsky, T. R. Boehly, T. C. Sangster, D. D. Meyerhofer, and R. L. McCrory, Phys. Plasmas **17**, 102706 (2010).

16. I. V. Igumenshchev, F. J. Marshall, J. A. Marozas, V. A. Smalyuk, R. Epstein, V. N. Goncharov, T. J. B. Collins, T. C. Sangster, and S. Skupsky, Phys. Plasmas **16**, 082701 (2009).

17. I. V. Igumenshchev, V. N. Goncharov, W. T. Shmayda, D. R. Harding, T. C. Sangster, and D. D. Meyerhofer, Phys. Plasmas **20**, 082703 (2013).

18. S. X. Hu, D. T. Michel, A. K. Davis, R. Betti, P. B. Radha, E. M. Campbell, D. H. Froula, and C. Stoeckl, Phys. Plasmas **23**, 102701 (2016).

19. P. B. Radha, F. J. Marshall, J. A. Marozas, A. Shvydky, I. Gabalski, T. R. Boehly, T. J. B. Collins, R. S. Craxton, D. H. Edgell, R. Epstein, J. A. Frenje, D. H. Froula, V. N. Goncharov, M. Hohenberger, R. L. McCrory, P. W. McKenty, D. D. Meyerhofer, R. D. Petrasso, T. C. Sangster, and S. Skupsky, Phys. Plasmas **20**, 056306 (2013).

20. D. G. Hicks, B. K. Spears, D. G. Braun, R. E. Olson, C. M. Sorce, P. M. Celliers, G. W. Collins, and O. L. Landen, Phys. Plasmas **17**, 102703 (2010).

21. C. Stoeckl, M. Bedzyk, G. Brent, R. Epstein, G. Fiksel, D. Guy, V. N. Goncharov, S. X. Hu, S. Ingraham, D. W. Jacobs-Perkins, R. K. Jungquist, F. J. Marshall, C. Mileham, P. M. Nilson, T. C. Sangster, M. J. Shoup III, and W. Theobald, Rev. Sci. Instrum. **85**, 11E501 (2014).

22. Y. Lin, T. J. Kessler, and G. N. Lawrence, Opt. Lett. **20**, 764 (1995).

23. T. R. Boehly, V. A. Smalyuk, D. D. Meyerhofer, J. P. Knauer, D. K. Bradley, R. S. Craxton, M. J. Guardalben, S. Skupsky, and T. J. Kessler, J. Appl. Phys. **85**, 3444 (1999).

24. S. Skupsky, R. W. Short, T. Kessler, R. S. Craxton, S. Letzring, and J. W. Soures, J. Appl. Phys. **66**, 3456 (1989).

25. S. P. Regan, J. A. Marozas, R. S. Craxton, J. H. Kelly, W. R. Donaldson, P. A. Jaanimagi, D. Jacobs-Perkins, R. L. Keck, T. J. Kessler, D. D. Meyerhofer, T. C. Sangster, W. Seka, V. A. Smalyuk, S. Skupsky, and J. D. Zuegel, J. Opt. Soc. Am. B **22**, 998 (2005).

26. F. J. Marshall, J. A. Delettrez, R. Epstein, R. Forties, R. L. Keck, J. H. Kelly, P. W. McKenty, S. P. Regan, and L. J. Waxer, Phys. Plasmas **11**, 251 (2004).

27. Inrad Optics, Northvale, NJ 07647.

28. D. K. Bradley, P. M. Bell, O. L. Landen, J. D. Kilkenny, and J. Oertel, Rev. Sci. Instrum. **66**, 716 (1995).

29. J. A. Oertel, T. Archuleta, C. G. Peterson, and F. J. Marshall, Rev. Sci. Instrum. **68**, 789 (1997).

30. C. Stoeckl, R. Boni, F. Ehrne, C. J. Forrest, V. Yu. Glebov, J. Katz, D. J. Lonobile, J. Magoon, S. P. Regan, M. J. Shoup III, A. Sorce, C. Sorce, T. C. Sangster, and D. Weiner, Rev. Sci. Instrum. **87**, 053501 (2016).

31. J. Delettrez, R. Epstein, M. C. Richardson, P. A. Jaanimagi, and B. L. Henke, Phys. Rev. A **36**, 3926 (1987).

32. I. V. Igumenshchev, D. H. Edgell, V. N. Goncharov, J. A. Delettrez, A. V. Maximov, J. F. Myatt, W. Seka, A. Shvydky, S. Skupsky, and C. Stoeckl, Phys. Plasmas **17**, 122708 (2010).

33. Prism Computational Sciences, Inc., Madison, WI 53711.

An Improved Method for Characterizing Plasma Density Profiles Using Angular Filter Refractometry

Introduction

The measurement of plasma density profiles is important to many areas of high-energy-density (HED) laser–plasma interactions.[1] Quantitative analysis of large HED plasmas has historically been challenging in the range of electron densities near 10^{20} to 10^{21} cm^{-3}. This density range is too low for x-ray probing techniques[2] and too high for most optical techniques. The large integrated phase obtained with optical probes makes it difficult to quantitatively measure the density profile when using typical interferometric techniques.[3,4] A variety of techniques do exist by which one can attempt to measure this region, but each technique has limiting drawbacks.[5]

A novel diagnostic called angular filter refractometry[6] (AFR) can enable one to characterize plasma density profiles up to densities of 10^{21} cm^{-3} by measuring the refraction angle of a probe beam passing through the plasma. The refractive information can be analyzed to characterize the density profile of the plasma. Previously used methods of reducing this experimental data to produce a plasma density profile were cumbersome and at times oversimplified the density profile,[6,7] both resulting in higher uncertainties.

A new method of analysis has been developed that involves simulating the AFR diagnostic response. A density profile described by seven parameters is used to generate synthetic AFR data, and a quantitative method for defining the degree of similarity between synthetic and observed AFR data provides feedback for subsequent iterations. The synthetic density profile is altered using an intelligent annealing algorithm to iteratively converge upon a solution whose resulting synthetic AFR data closely matches observed AFR data.

This approach has multiple advantages over other methods of analysis: It requires minimal user interface, which eliminates human error that exists from direct manipulation of the observed data. It lends itself to a statistical uncertainty calculation based on χ^2 statistics, allowing one to assess quantitative uncertainties. The resultant density profile, by nature of

it being analytic, provides smooth gradients free of noise for scale-length calculations.

In this article, the process by which the synthetic density can be matched to observed AFR data is explained in detail. The different causes of uncertainty specific to this approach and to the diagnostic in general will be described.

Angular Filter Refractometry

The AFR diagnostic is part of the fourth-harmonic (4ω) probe system[8] on LLE's OMEGA EP laser.[9] The 4ω probe is created from the conversion of a Nd:glass laser pulse to its fourth harmonic ($\lambda_p = 263$ nm) and has a pulse width of 10 ps with 20 mJ of energy. Figure 149.44 shows a conceptual schematic for the AFR diagnostic. The red lines represent the path of the undisturbed probe beam. The beam has a diameter of 3.5 mm and passes through the target chamber center (TCC), where the plasma will be created. The probe is collected at $f/4$ and transported more than 4 m to the diagnostic table.
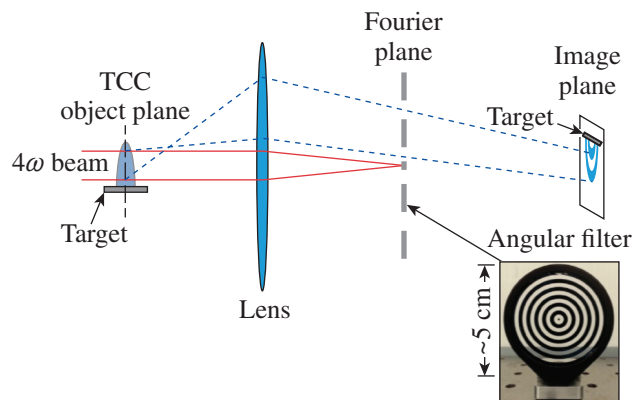
E22129JR

Figure 149.44
A simplified schematic of the angular filter refractometry (AFR) diagnostic. Unrefracted probe rays (red lines) are blocked by the opaque center of the angular filter. Refracted probe rays (dashed blue lines) hit or miss the filter based on their refraction angles through the plasma. The filter casts shadows corresponding to specific refraction angles that are observed on the image plane. TCC: target chamber center

The TCC plane is image relayed to a charge-coupled–device camera with a resolution of 5 μm over a 5-mm field of view in the object plane.[8]

An angular filter is placed at the focus of the unrefracted probe beam, or the Fourier plane.[10] The filter consists of a central opaque dot and oscillating transmissive and opaque rings (Fig. 149.44). The unrefracted probe is stopped by the central dot. In the presence of a plasma, refracted rays (dashed blue lines) will fill a larger area of the angular filter. The opaque regions of the filter block bands of refraction angles, thereby casting shadows in the image plane. Because the angle of refraction of a probe ray is directly proportional to its radial location in the Fourier plane, the shadows on the image plane have contours of constant refraction. To calibrate the specific angular cutoffs, a plano-concave lens was placed at TCC, allowing one to deduce the refraction angle (θ) as a function of displacement (r) from the optical axis in the Fourier plane. For a more-detailed description of the diagnostic, see Ref. 6.

Figure 149.45 shows an example of an AFR image measured from a 250-μm-thick CH target that was ablated by four UV (λ = 351 nm) laser beams with a total of 9 kJ of energy in a
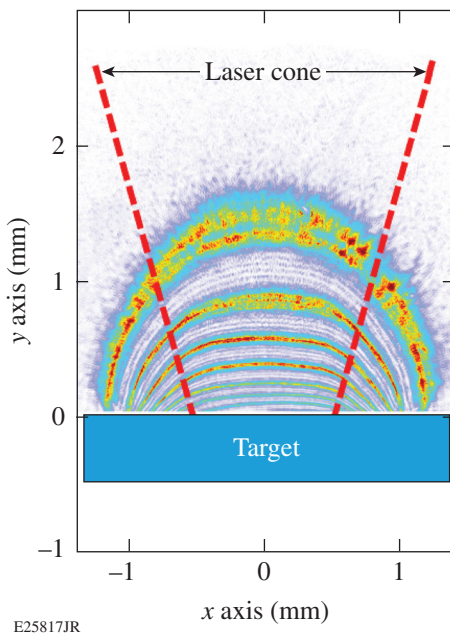

Figure 149.45
A laser irradiates a CH target and creates an axisymmetric plasma plume. The angular filter blocks certain refractive angles, resulting in the banded image.

2.5-ns square pulse focused to an 800-μm-diam spot that contained 95% of the energy. The target surface was set to $y = 0$, and the plasma expanded in the positive y direction away from the target. The refraction bands produced by the AFR diagnostic show the shape of the expanding plasma plume.

Analysis

1. Creating a Synthetic AFR Image

The AFR images are analyzed by comparing them to a synthetic image generated with a model 3-D plasma density n_e (x,y,z). (Note: All following references to n_e assume a dependence on x,y,z.) A typical HED laser-plasma plume from a planar target can be modeled by a super-Gaussian parallel to the target and exponential normal to the target.[11] The 3-D density profile was assumed to be axisymmetric along the target normal. The behavior along the target normal at the plasma's center is modeled as

$$n_e(0,y,0) = n_0 \cdot \left[A \cdot \exp\left(\frac{-y}{L_{y1}}\right) + (1-A) \cdot \exp\left(\frac{-y}{L_{y2}}\right) \right], \quad (1)$$

where n_0 is the peak density and A assigns relative strength to two exponential profiles with scale lengths L_{y1} and L_{y2}. This allows the profile to adapt to a decreasing scale length as typically occurs close to the target surface. The full density profile, including the transverse dimension, is

$$n_e(x,y,z) = n_e(0,y,0)$$
$$\times \exp\left\{ -\left(\frac{x^2+z^2}{L_{xz}^2}\right)^{\frac{1}{2}\left[c_1 - c_2 \cdot \ln(c_3 \cdot y)\right]} \right\}, \quad (2)$$

where L_{xz} is the scale length in both x and z and the parameters c_1, c_2, and c_3 (representing two independent parameters) are used to define the order term for the super-Gaussian profile. The order term was empirically found so one could accurately match experimentally observed AFR contours. Equations (1) and (2) together form the seven-parameter function that constitutes the synthetic 3-D density. Figure 149.46(a) shows the density solution to the experimental AFR map shown in Fig. 149.45, where the deduced density spans two orders of magnitude (10^{19} to 10^{21} cm^{-3}).

With the probe propagating in the z direction, the accumulated phase of the probe ray passing through the plasma is related to the 3-D plasma density according to
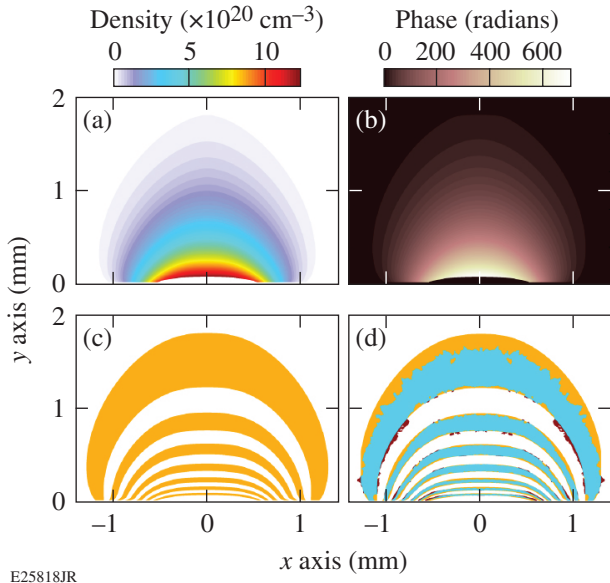
E25818JR

Figure 149.46

(a) A 2-D slice of a 3-D axisymmetric synthetic density profile generated from the density function described by Eq. (2). (b) The integrated phase accrued by the probe passing through the synthetic plasma. (c) The synthetic AFR image made by extracting refraction information from the phase map following Eq. (4) and eliminating angles blocked by the filter. (d) A visual overlay of the synthetic (orange) image and experimental (red) image. Blue indicates where the profiles overlap.

$$\phi(x,y) \approx \frac{\pi}{\lambda_p n_c} \int_{-\infty}^{+\infty} n_e(x,y,z)\,dz\,[\text{rad}], \qquad (3)$$

where λ_p is the probe-laser wavelength (263 nm) and $n_e \ll n_c$, where $n_c = 1.1 \times 10^{21} / \lambda_{p,\mu m}^2 = 1.6 \times 10^{22}$ cm^{-3} is the critical plasma density for the probe laser. Figure 149.46(b) shows the integrated phase of the density profile in Fig. 149.46(a), where changes in x and y along the ray path are ignored. The angle of refraction of a probe ray exiting the plasma is calculated from the transverse gradient of the accrued phase:

$$\theta(x,y) = \frac{\lambda_p}{2\pi} \sqrt{\left(\frac{\partial \phi}{\partial x}\right)^2 + \left(\frac{\partial \phi}{\partial y}\right)^2}\,[\text{rad}]. \qquad (4)$$

From the calculated 2-D refraction map, a filter function based on the calibration is applied that creates a synthetic AFR image comparable to that measured in the experiment [Fig. 149.46(c)].

2. Simulated Annealing

An iterative solver alters the parameters of the synthetic density function to optimize the match between the synthetic and experimental AFR images. The quality of the match is based on the location of the edges of the bands. This was

accomplished by taking many radial lineouts of the synthetic and experimental AFR images and finding the position of the edges of the bands at each angle [Fig. 149.47(a)]. The edge locations in the experimental images were found by applying a 20% intensity threshold to the normalized data, which eliminated most noise without notable alterations to the bands' behavior and size. Figure 149.47(b) compares the thresholded experimental edges to the synthetic AFR edges. The squared differences of the locations between the synthetic and experimental AFR band edges were averaged over the entire image:

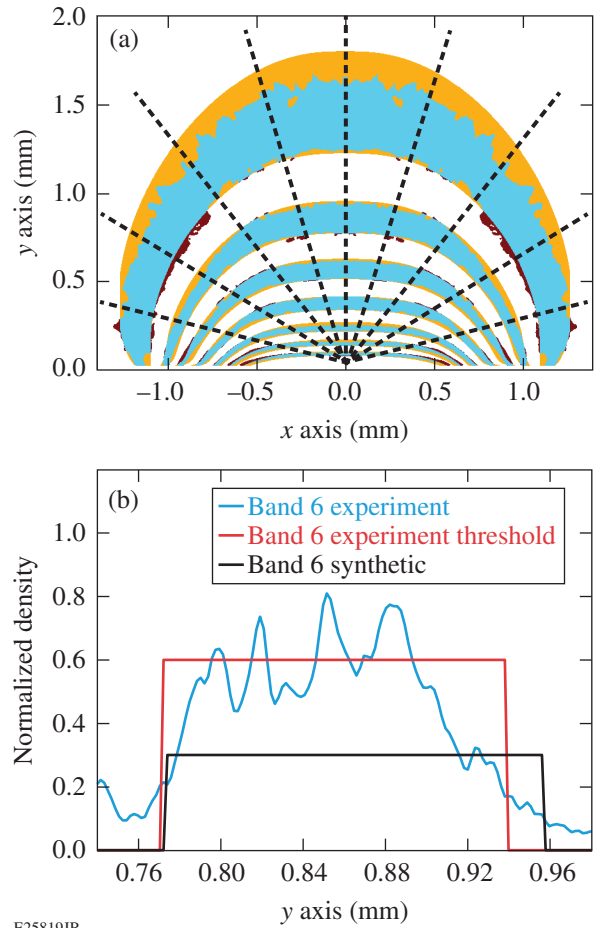$$m = \sum_{n=1}^{14} \sum_{r=1}^{100} (E_{n,r} - S_{n,r})^2, \qquad (5)$$

E25819JR

Figure 149.47

(a) The algorithm draws lineouts from the center of the target surface and finds the edges of the experimental and synthetic bands on those lines. (b) A lineout of the sixth band (counting from the bottom) taken along $x = 0$. A threshold was applied to the experimental data to eliminate noise.

where $E_{n,r}$ and $S_{n,r}$ are the edge locations of the experimental and synthetic bands, respectively, at an edge n and an angle r. All 14 edges were examined at a large number of angles so that slight fluctuations at some points in the experimental AFR image do not dominate the match (Fig. 149.47).

The solver incorporates the simulated annealing[12] (SA) algorithm to systematically alter the variables of the density function until a global minimum for m in the parameter space is found. An SA algorithm was chosen because of its ability to find a global minimum in a large parameter space [seven parameters; see Eq. (1)], where many local minima exist. Figure 149.48 displays the logical flowchart that the SA algorithm follows. The SA algorithm takes an initial user-defined density guess n_i, generates the synthetic AFR image, and calculates m_i. The density is then perturbed by Δn and a new match parameter $m_{i+\Delta n}$ is calculated. If $m_{i+\Delta n} - m_i < 0$, the new profile is accepted and $n_i + \Delta n$ becomes the new n_i. If $m_{i+\Delta n} - m_i > 0$, the new profile is considered for rejection, although there is a chance that it may be accepted.

Accepting a poorer match over a superior one allows the profile to escape from local minima enroute to the final solution. The range over which parameters' values are generated and the likelihood of accepting a poorer match decrease at later iterations[13] so that the algorithm focuses around a nearby solution. After a set number of runs, the SA algorithm resets the range of parameters in the search and the likelihood of accepting a poor match. Repeating this process numerous times makes it unlikely for the algorithm to get stuck in a local minimum. The simulated annealing algorithm terminates when a chosen number of iterations pass without a new best match being discovered (stop criterion). At this point the profile corresponding to the lowest calculated match is returned by the algorithm. Figure 149.49(a) shows how a single simulating annealing algorithm closes in on its results. Occasionally it escapes its local minimum and finds a new one, trending toward the optimal value. The process of escaping a local minimum can be seen more clearly in Fig. 149.49(b).

E25821JR
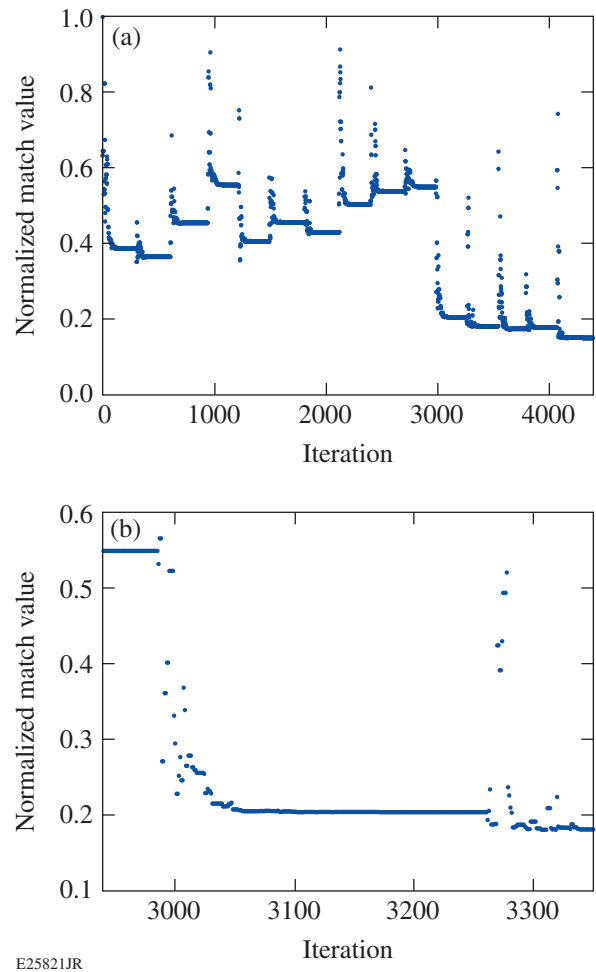
Figure 149.49
(a) The normalized match value m is plotted over a single simulating annealing run while modifying the parameters simultaneously. The long stretches of constant value represent local minima, which are typically escaped after first passing through inferior values. (b) A closer look at a certain portion of the run shows that the normalized value decreases sharply over 50 iterations that accept multiple poorer matches. After a long stretch in a local minimum, the algorithm begins accepting poorer matches again and then quickly finds a new lowest match value.

E25820JR

Figure 149.48
A flowchart describing simulated annealing.

This solver utilizes a series of SA algorithms that focus on particular groupings of parameters rather than one SA algorithm that modifies all parameters simultaneously. One group contains parameters that primarily affect the heights of the bands (n_0, A, L_{y1}, and L_{y2}); the other group contains parameters that primarily affect the behavior of the bands near the target surface (L_{xz}, c_1, c_2, and c_3). The SA algorithms are run in an alternating cycle on each parameter group, increasing the demand for accuracy the longer each group goes unaltered. The solver reaches the stop criterion when a certain number of iterations on both parameter groups pass without improving the match. This approach converges on a good match nearly twice as quickly as using one SA algorithm on all parameters. After the run is complete, a simple local neighborhood search is executed to fine-tune the answer.

Uncertainty Analysis

Three primary sources of uncertainty exist in the analysis. The first source is the statistical uncertainty in the match, which was accounted for by testing the χ^2 statistic.[14] A second source resides in the unknown integration constant in calculating phase from the angle of refraction [Eq. (4)]. The final source of uncertainty comes from a systemic left–right asymmetry in the AFR diagnostic presumed to be related to an optical aberration in the system. All three uncertainties are quantitatively accounted for and added in quadrature.

1. Statistical Uncertainty
    The uncertainty related to the sensitivity to fit is calculated as

$$\Delta n_{\text{stat}} = \pm \sqrt{\left(\frac{dn_e}{dp_1}\right)^2 \sigma_{p1}^2 + \left(\frac{dn_e}{dp_2}\right)^2 \sigma_{p2}^2 + \ldots} \ [\%] , \quad (6)$$

where dn_e/dp is the derivative of the density function with respect to parameter p and σ_p is the uncertainty in p. The uncertainty in each parameter is determined using χ^2 statistical testing, which describes the similarity between theoretical and observed data. For this data, the χ^2 value is

$$\chi^2 = \sum_{n=1}^{14} \sum_{r=1}^{100} \frac{(E_{n,r} - S_{n,r})}{\alpha^2} . \quad (7)$$

This equation is the match value m divided by α^2, which represents the experimental noise, or the observed data that *cannot* be fit by the theoretical model. This means that m_{min}

represents the degree of noise for a given experimental AFR image, so $\alpha^2 = m_{\text{min}}$.

The uncertainty in each parameter is related to the way it alters the behavior of χ^2 around χ^2_{min}. Altering the parameters around their best-fit values increases χ^2, indicating a lower probability that these parameter values are correct.[14] A confidence interval[15] ΔS is defined to describe the increase to χ^2_{min} that would result in an N-percent certainty that the solution lies within ΔS (Ref. 5). Each parameter is individually altered until $\chi^2 = \chi^2_{\text{min}} + \Delta S$; the boundaries of this window represent the uncertainty in the parameter, σ. This was factored back into Eq. (6) to find the uncertainty in density. Because χ^2 is inversely proportional to m_{min}, Δn_{stat} will be larger for profiles whose best matches are not as strong. The calculated uncertainty map from χ^2 statistics for the case in Fig. 149.46 is shown in Fig. 149.50(a).

E25822JR
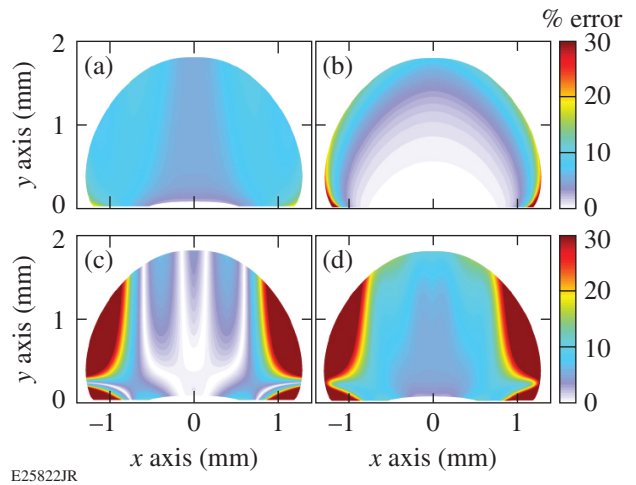
Figure 149.50
(a) The statistical uncertainty map corresponding to the density function. (b) The degenerative uncertainty. Note that the color bars cut off at 30% but at one point are as high as 100%. (c) The left–right uncertainty. Note that the color bars cut off at 30%, but uncertainties at the outer regions get higher. (d) The combined uncertainty.

2. Degenerative Uncertainty
    The next source of uncertainty is related to the fact that the AFR diagnostic measures refraction, which is proportional to the gradient of the plasma density, or phase. The phase is proportional to the integration of refraction plus an integration constant (c) allowing for degenerate solutions. The value of c is a source of uncertainty in the density since changing c does not change the AFR image; therefore, boundary conditions must be established.

The main physical boundary condition on the density function is that density must fall to zero away from the target surface. The lowest density that contributes to the AFR image lies somewhere along the outer band's edge. This value must be non-negative, which gives a lower bound for c (negative value). Positive values for c violate the boundary condition of density going to zero without the introduction of additional gradients that exist outside the outermost band that are smaller than measurable by the AFR diagnostic.

There is no way to define the upper bound for c, so for testing purposes, the maximum shift to the density in either direction was taken to be the largest downward shift possible. A density function with over 20 parameters was used to create test AFR images. Those AFR images were treated as experimental ones and run through the iterative solver. The statistical uncertainty and degenerative uncertainty combined were always able to encompass the percent difference between the test cases and the corresponding optimized synthetic densities, proving the validity of these uncertainty calculations.

The corresponding uncertainty can be described by [Fig. 149.50(b)]

$$\Delta n_{deg} = \pm \frac{c}{n_e} [\%] . \tag{8}$$

3. Asymmetry Uncertainty

There is a consistent left–right asymmetry in all AFR images. In theory the plasmas should be approximately axisymmetric due to nearly axisymmetric illumination, so it is believed that this asymmetry is symptomatic of an aberration in the probe beam. Efforts to model the presumed aberration were unsuccessful; therefore, it is accounted for as a source of uncertainty. Optimizations are run separately on the left and right sides of each shot and the solution is taken to exist somewhere within the percent difference between the resulting densities. This percent difference contributes to the uncertainty [Fig. 149.50(c)]:

$$\Delta n_{lr} = \frac{\left| n_{left} - n_{right} \right|}{1/2 \times \left(n_{left} + n_{right} \right)} [\%] . \tag{9}$$

Discussion

The total uncertainty is generated by adding the three separate uncertainty sources in quadrature.[16] The uncertainty calculations for the far left and right edges exceed 100% because

of the asymmetry. Over a large region of interest, the central two-thirds of the profile has an uncertainty of under 20%. The uncertainty along the target normal is under 10%.

The use of an analytic density function is an additional benefit to this analysis method. It facilitates an accurate calculation of the density scale lengths caused by the smoothness of the density derivative. This results in a low uncertainty for scale length. The scale length can be calculated as

$$L_y = \mp n_e \left[\frac{dn_e}{dy} \right]^{-1} . \tag{10}$$

Figure 149.51 shows the density and scale length of the plasma analyzed throughout this article along the target normal. Note that the uncertainty increases as the plasma is farther from the target surface but does not exceed 10%.

E25823JR
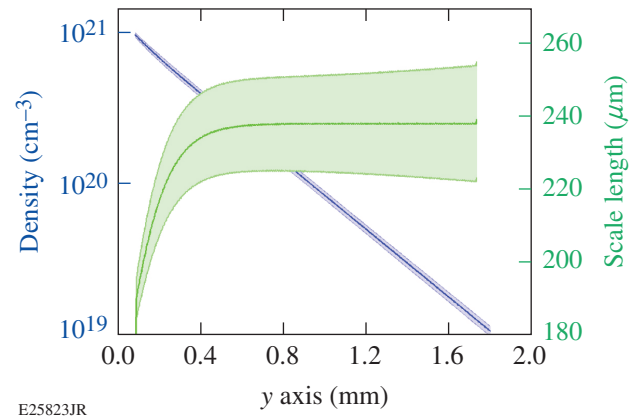
Figure 149.51
The blue line is the plasma density profile along the target normal at the center of the plasma profile ($x = 0$) measured from the AFR data shown in Fig. 149.45. The original target surface is located at $y = 0$. The green curve is the corresponding scale length. The uncertainty in scale length increases with y but is under 10% at all points.

Conclusion

A new method of analyzing data from the AFR diagnostic has been developed. A seven-parameter density profile was used to produce synthetic AFR images, and an iterative solver was developed that could successfully match synthetic data to experimental AFR images. A 2-D uncertainty map for the 3-D density was presented that has an uncertainty of less than 10% in the region of interest.

Several future improvements could increase the accuracy of this analysis. By adding more variables to the density function, it will have more flexibility to match the experimental AFR images, therefore improving the model fit. This would, however, be gained at the cost of computer run time. The degeneracy uncertainty could be erased completely if a boundary condition was known. This could be accomplished, for example, by measuring phase in the low-density regions using simultaneous interferometry. If the asymmetry was caused by an aberration, it could be largely reduced or eliminated by successful modeling the aberration on the probe beam, or experimentally fixing the aberration.

ACKNOWLEDGMENT

REFERENCES

1. National Research Council (U.S.) Committee on High Energy Density Plasma Physics, *Frontiers in High Energy Density Physics: The X-Games of Contemporary Science* (The National Academies Press, Washington, DC, 2003).

2. S. H. Glenzer, G. Gregori, F. J. Rogers, D. H. Froula, S. W. Pollaine, R. S. Wallace, and O. L. Landen, Phys. Plasmas **10**, 2433 (2003).

3. R. Benattar and C. Popovics, J. Appl. Phys. **54**, 603 (1983).

4. R. J. Noll *et al.*, Appl. Opt. **25**, 769 (1986).

5. R. S. Craxton, F. S. Turner, R. Hoefen, C. Darrow, E. F. Gabl, and Gar. E. Busch, Phys. Fluids B **5**, 4419 (1993).

6. D. Haberberger, S. Ivancic, S. X. Hu, R. Boni, M. Barczys, R. S. Craxton, and D. H. Froula, Phys. Plasmas **21**, 056304 (2014).

7. S. Ivancic, D. Haberberger, H. Habara, T. Iwawaki, K. S. Anderson, R. S. Craxton, D. H. Froula, D. D. Meyerhofer, C. Stoeckl, K. A. Tanaka, and W. Theobald, Phys. Rev. E **91**, 051101(R) (2015).

8. D. H. Froula, R. Boni, M. Bedzyk, R. S. Craxton, F. Ehrne, S. Ivancic, R. Jungquist, M. J. Shoup, W. Theobald, D. Weiner, N. L. Kugland, and M. C. Rushford, Rev. Sci. Instrum. **83**, 10E523 (2012).

9. J. H. Kelly, L. J. Waxer, V. Bagnoud, I. A. Begishev, J. Bromage, B. E. Kruschwitz, T. J. Kessler, S. J. Loucks, D. N. Maywar, R. L. McCrory, D. D. Meyerhofer, S. F. B. Morse, J. B. Oliver, A. L. Rigatti, A. W. Schmid, C. Stoeckl, S. Dalton, L. Folnsbee, M. J. Guardalben, R. Jungquist, J. Puth, M. J. Shoup III, D. Weiner, and J. D. Zuegel, J. Phys. IV France **133**, 75 (2006).

10. J. W. Goodman, *Introduction to Fourier Optics* (McGraw-Hill, New York, 1968).

11. M. Murakami *et al.*, Phys. Plasmas **12**, 062706 (2005).

12. S. Kirkpatrick, C. D. Gelatt, Jr., and M. P. Vecchi, Science **220**, 671 (1983).

13. S. Nozaki *et al.*, Rev. Sci. Instrum. **73**, 3198 (2002).

14. N. Bobroff, Rev. Sci. Instrum. **57**, 1152 (1986).

15. M. Lampton, B. Margon, and S. Bowyer, Astrophys. J. **208**, 177 (1976).

16. J. R. Taylor, *An Introduction to Error Analysis*, 2nd ed. (University Science Books, Sausalito, CA, 1982).

Publications and Conference Presentations

Publications

S. G. Demos and R. A. Negres, "Morphology of Ejected Particles and Impact Sites on Intercepting Substrates Following Exit-Surface Laser Damage with Nanosecond Pulses in Silica," Opt. Eng. **56**, 011016 (2016).

V. N. Goncharov, S. P. Regan, E. M. Campbell, T. C. Sangster, P. B. Radha, J. F. Myatt, D. H. Froula, R. Betti, T. R. Boehly, J. A. Delettrez, D. H. Edgell, R. Epstein, C. J. Forrest, V. Yu. Glebov, D. R. Harding, S. X. Hu, I. V. Igumenshchev, F. J. Marshall, R. L. McCrory, D. T. Michel, W. Seka, A. Shvydky, C. Stoeckl, W. Theobald, and M. Gatu-Johnson, "National Direct-Drive Program on OMEGA and the National Ignition Facility," Plasma Phys. Control. Fusion **59**, 014008 (2017) (invited).

M. C. Gregor, R. Boni, A. Sorce, J. Kendrick, C. A. McCoy, D. N. Polsin, T. R. Boehly, P. M. Celliers, G. W. Collins, D. E. Fratanduono, J. H. Eggert, and M. Millot, "Absolute Calibration of the OMEGA Streaked Optical Pyrometer for Temperature Measurements of Compressed Materials," Rev. Sci. Instrum. **87**, 114903 (2016).

S. X. Hu, D. T. Michel, A. K. Davis, R. Betti, P. B. Radha, E. M. Campbell, D. H. Froula, and C. Stoeckl, "Understanding the Effects of Laser Imprint on Plastic-Target Implosions on OMEGA," Phys. Plasmas **23**, 102701 (2016).

A. A. Kozlov, S. Papernov, J. B. Oliver, A. Rigatti, B. Taylor, B. Charles, and C. Smith, "Study of the Picosecond Laser Damage in HfO_2/SiO_2-Based Thin-Film Coatings in Vacuum," Proc. SPIE. **10014**, 100141Y (2016).

C. K. Li, P. Tzeferacos, D. Lamb, G. Gregori, P. A. Norreys, M. J. Rosenberg, R. K. Follett, D. H. Froula, M. Koenig, F. H. Seguin, J. A. Frenje, H. G. Rinderknecht, H. Sio, A. B. Zylstra, R. D. Petrasso, P. A. Amendt, H. S. Park, B. A. Remington, D. D. Ryutov, S. C. Wilks, R. Betti, A. Frank, S. X. Hu, T. C. Sangster, P. Hartigan, R. P. Drake, C. C. Kuranz, S. V. Lebedev, and N. C. Woolsey, "Scaled Laboratory Experiments Explain the Kink Behaviour of the Crab Nebula Jet," Nature Commun. **7**, 13081 (2016).

J. B. Oliver, "Analysis of a Planetary-Rotation System for Evaporated Optical Coatings," Appl. Opt. **55**, 8550 (2016).

J. B. Oliver, "Impact of Deposition-Rate Fluctuations on Thin-Film Thickness and Uniformity," Opt. Lett. **41**, 5182 (2016).

S. Papernov, A. A. Kozlov, J. B. Oliver, C. Smith, L. Jensen, S. Günster, H. Mädebach, and D. Ristau, "Role of HfO_2/SiO_2 Thin-Film Interfaces in Near-Ultraviolet Absorption and Pulsed Laser Damage," Opt. Eng. **56**, 011004 (2016).

B. W. Plansinis, W. R. Donaldson, and G. P. Agrawal, "Spectral Splitting of Optical Pulses Inside a Dispersive Medium at a Temporal Boundary," IEEE J. Quantum Electron. **52**, 6100708 (2016).

S. Salzman, H. J. Romanofsky, G. West, K. L. Marshall, S. D. Jacobs, and J. C. Lambropoulos, "Acidic Magnetorheological Finishing of Infrared Polycrystalline Materials," Appl. Opt. **55**, 8448 (2016).

A. A. Solodov, B. Yaakobi, D. H. Edgell, R. K. Follett, J. F. Myatt, C. Sorce, and D. H. Froula, "Measurements of Hot-Electron Temperature in Laser-Irradiated Plasmas," Phys. Plasmas **23**, 102707 (2016).

Forthcoming Publications

D. H. Barnak, R. Betti, M. J. Bonino, E. M. Campbell, J. R. Davies, V. Yu. Glebov, D. R. Harding, J. P. Knauer, S. P. Regan, A. B. Sefkow, A. J. Harvey-Thompson, K. J. Peterson, D. B. Sinars, S. A. Slutz, and M. R. Weis, "Magnetized Liner Inertial Fusion on OMEGA," to be published in Physics of Plasmas (invited).

C. Dorrer, W. A. Bittle, R. Cuffney, M. Spilatro, E. M. Hill, T. Z. Kosc, J. H. Kelly, and J. D. Zuegel, "Time-Multiplexed Pulse Shaping," to be published in the Journal of Lightwave Technology.

C. Dorrer and J. Hassett, "Model-Based Optimization of Near-Field Binary Pixelated-Beam Shapers," to be published in Applied Optics.

R. Epstein, S. P. Regan, B. A. Hammel, L. J. Suter, H. A. Scott, M. A. Barrios, D. K. Bradley, D. A. Callahan, C. Cerjan, G. W. Collins, S. N. Dixit, T. Doeppner, M. J. Edwards, D. R. Farley, K. B. Fournier, S. Glenn, S. H. Glenzer, I. E. Golovkin, A. Hamza, D. G. Hicks, N. Izumi, O. S. Jones, M. H. Key, J. D. Kilkenny, J. L. Kline, G. A. Kyrala, O. L. Landen, T. Ma, J. J. MacFarlane, A. J. Mackinnon, R. C. Mancini, R. L. McCrory, D. D. Meyerhofer, N. B. Meezan, A. Nikroo, H.-S. Park, P. K. Patel, J. E. Ralph, B. A. Remington, T. C. Sangster, V. A. Smalyuk, P. T. Springer, R. P. J. Town, and J. L. Tucker, "Applications and Results of X-Ray Spectroscopy in Implosion Experiments at the National Ignition Facility," to be published in the Proceedings of Atomic Processes in Plasmas (invited).

C. Fagan, M. Sharpe, W. T. Shmayda, and W. U. Schröder, "The Impact of Acid Treatments and Electropolishing Stainless-Steel Surfaces on Tritium Inventories," to be published in Fusion Science and Technology.

C. J. Forrest, P. B. Radha, J. P. Knauer, V. N. Goncharov, V. Yu. Glebov, S. P. Regan, M. J. Rosenberg, T. C. Sangster, W. T. Shmayda, C. Stoeckl, and M. Gatu Johnson, "First Measurements of Deuterium–Tritium and Deuterium–Deuterium Fusion-Reaction Yields in Ignition-Scalable Direct-Drive Implosions," to be published in Physical Review Letters.

R. F. Heeter, J. E. Bailey, R. S. Craxton, B. G. DeVolder, E. S. Dodd, E. M. Garia, E. J. Huffman, C. A. Iglesias, J. A. King, J. L. Kline, D. A. Liedahl, P. W. McKenty, Y. P. Opachich, G. A. Rochau, P. W. Ross, M. B. Schneider, M. E. Sherrill,

B. G. Wilson, R. Zhang, and T. S. Perry, "Conceptual Design of Initial Opacity Experiments on the National Ignition Facility," to be published in the Journal of Plasma Physics.

I. V. Igumenshchev, D. T. Michel, R. C. Shah, E. M. Campbell, R. Epstein, C. J. Forrest, V. Yu. Glebov, V. N. Goncharov, J. P. Knauer, F. J. Marshall, R. L. McCrory, S. P. Regan, T. C. Sangster, C. Stoeckl, A. J. Schmitt, and S. P. Obenschain, "Three-Dimensional Hydrodynamic Simulations of OMEGA Implosions," to be published in Physics of Plasmas (invited).

J. F. Myatt, R. K. Follett, J. G. Shaw, D. H. Edgell, D. H. Froula, I. V. Igumenshchev, and V. N. Goncharov, "A Wave-Based Model for Cross-Beam Energy Transfer in Direct-Drive Inertial Confinement Fusion," to be published in Physics of Plasmas.

J. B. Oliver, "Impact of Non-Integer Planetary Revolutions on the Distribution of Evaporated Optical Coatings," to be published in Applied Optics.

T. Petersen, J. Bromage, and J. D. Zuegel, "High-Average-Power, 2-μm Femtosecond Optical Parametric Oscillator Synchronously Pumped by a Thin-Disk, Mode-Locked Laser," to be published in Optics Express.

B. S. Rice, J. Ulreich, J. Crippen, P. Fitzsimmons, and A. Nikroo, "Permeation Fill-Tube Design for Inertial Confinement Fusion Target Capsules," to be published in High Power Laser Science and Engineering (special issue).

C. Stoeckl, R. Epstein, R. Betti, W. Bittle, J. A. Delettrez, C. J. Forrest, V. Yu. Glebov, V. N. Goncharov, D. R. Harding, I. V. Igumenshchev, D. W. Jacobs-Perkins, R. T. Janezic, J. H. Kelly, T. Z. Kosc, R. L. McCrory, D. T. Michel, C. Mileham, P. W. McKenty, F. J. Marshall, S. F. B. Morse, S. P. Regan, P. B. Radha, B. S. Rice, T. C. Sangster, M. J. Shoup III, W. T. Shmayda, C. Sorce, W. Theobald, J. Ulreich, M. D. Wittman, D. D. Meyerhofer, J. A. Frenje, M. Gatu Johnson, and R. D. Petrasso, "Monochromatic Backlighting of Direct-Drive Cryogenic DT Implosions on OMEGA," to be published in Physics of Plasmas (invited).

D. Turnbull, C. Goyon, G. E. Kemp, B. B. Pollock, D. Mariscal, L. Divol, J. S. Ross, S. Patankar, J. D. Moody, and P. Michel, "Refractive Index Seen by a Probe Beam Interacting with a Laser-Plasma System," to be published in Physical Review Letters.

Conference Presentations

Y. Zhao and W. R. Donaldson, "Materials Properties Characterization and Device Simulation on a Nonuniform Al Component $A1_xGa_{1-x}N$ Metal–Semiconductor–Metal Photodetector," International Workshop on Nitride Semiconductors, Orlando, FL, 2–7 October 2016.

_____

The following presentations were made at the Industrial Associates Fall Meeting 2016, Rochester, NY, 9–12 October 2016:

Y. Li and C. Dorrer, "Wavefront-Aberration Correction Using Binary Amplitude and Polarization Modulation."

B. W. Plansinis, W. R. Donaldson, and G. P. Agrawal, "Spectral Splitting of Optical Pulses Inside a Dispersive Medium at a Temporal Boundary."

_____

E. M. Campbell, J. Bromage, J. D. Zuegel, S. G. Demos, D. H. Froula, D. Haberberger, B. Krupke, P. A. Norreys, J. Sadler, B. Bingham, N. Fisch, and W. Leemans, "High-Peak-Power Laser Research at the Laboratory for Laser Energetics and the Pathway to a 100-Petawatt-Class Laser," Nuclear Photonics 2016, Monterey, CA, 16–21 October 2016.

_____

The following presentations were made at Frontiers in Optics, Rochester, NY, 17–21 October 2016:

S. G. Demos, B. N. Hoffman, T. J. Kessler, M. D. Feit, R. A. Negres, C. W. Carr, D. A. Cross, J. Bude, and A. M. Rubenchik, "Transient Modulation of Refractive Index Under Exposure to High-Power Laser Pulses" (invited).

T. Z. Kosc, "Steve Jacobs: The Optics Outreach Innovator."

Y. Li and C. Dorrer, "Wavefront-Aberration Correction Using Binary Amplitude and Polarization Modulation."

K. L. Marshall, "Thirty-Five Years of Liquid Crystal Research at the Laboratory for Laser Energetics: From Laser Fusion to Electronic Paper" (invited).

B. W. Plansinis, G. P. Agrawal, and W. R. Donaldson, "Removing Pulse Jitter with Temporal Waveguides."

J. M. Schoen, "History of the Center for Optics Manufacturing" (invited).

K. A. Sharma, T. A. Germer, C. Smith, J. D. Zuegel, J. B. Oliver, and T. G. Brown, "Scattered-Light Analysis of Birefringent Coatings for Distributed Polarization Rotators."

_____

The following presentations were made at the 37th Tritium Focus Group Meeting, Rochester, NY, 25–27 October 2016:

T. Burke, M. Sharpe, and W. T. Shmayda, "Tritium in Targets Measured by an X-Ray Detection System."

C. Fagan, M. Sharpe, W. T. Shmayda, and W. U. Schröder, "The Effect of Surface Modifications on Tritium Adsorption and Absorption by Stainless Steel (316)."

M. Sharpe, C. Fagan, and W. T. Shmayda, "Influence of the Water Layers Adsorbed onto Stainless-Steel 316 on Tritium Migration."

W. T. Shmayda, "Properties of DT Ice in Cryotargets."

M. D. Wittman, N. P. Redden, D. R. Harding, W. T. Shmayda, A. Agliata, C. Rees, R. Chapman, R. F. Earley, J. Magoon, M. J. Shoup III, C. Taylor, R. Taylor, J. Ulreich, C. Abbot, T. Lewis, M. H. Romanofsky, J. Szczepanski, J. Konzel, S. Reber, D. J. Lonobile, and J. L. Reid, "Cryogenic Fill-Tube Target Facility for Evaluating DT-Filled National Ignition Facility and OMEGA-Scale Cryogenic Targets."

_____

T. Petersen, J. Bromage, and J. D. Zuegel, "High-Average-Power, 2-μm Femtosecond Optical Parametric Oscillator Synchronously Pumped by a Thin-Disk, Mode-Locked Laser," Advanced Solid State Lasers Conference, Boston, MA, 30 October–3 November 2016.

_____

The following presentations were made at the 58th Annual Meeting of the APS Division of Plasma Physics, San Jose, CA, 31 October–4 November 2016:

K. S. Anderson, P. W. McKenty, A. Shvydky, J. P. Knauer, T. J. B. Collins, P. B. Radha, F. Weilacher, and M. M. Marinak, "Three-Dimensional Analysis of the Effects of Low-Mode Asymmetries on OMEGA Cryogenic Implosions."

D. H. Barnak, R. Betti, M. J. Bonino, E. M. Campbell, J. R. Davies, V. Yu. Glebov, D. R. Harding, J. P. Knauer, S. P. Regan, A. B. Sefkow, A. J. Harvey-Thompson, K. J. Peterson, D. B. Sinars, S. A. Slutz, and M. R. Weis, "Magnetized Liner Inertial Fusion on OMEGA" (invited).

R. Betti, J. P. Knauer, A. V. Maximov, T. J. B. Collins, C. Stoeckl, A. Bose, J. Woo, A. R. Christopherson, A. Shvydky, W. Theobald, J. A. Delettrez, F. J. Marshall, P. B. Radha, S. P. Regan, E. M. Campbell, W. Shang, W. Seka, and S. X. Hu, "The 1-D Campaign on OMEGA: A Systematic Approach to Find the Optimum Path to Ignition."

E. Borwick, S. X. Hu, J. Li, R. Yan, and C. Ren, "Full-Pulse Particle-in-Cell Simulations of Hot-Electron Generation in OMEGA Experiments."

A. Bose, K. M. Woo, R. Betti, D. Mangino, A. R. Christopherson, E. M. Campbell, R. L. McCrory, S. P. Regan, V. N. Goncharov, T. C. Sangster, C. J. Forrest, V. Yu. Glebov, J. P. Knauer, F. J. Marshall, C. Stoeckl, W. Theobald, R. Nora, J. A. Frenje, M. Gatu Johnson, and D. Shvarts, "Achievement of Core Conditions for Alpha Heating in Direct-Drive Inertial Confinement Fusion."

S. Bucht, D. Haberberger, J. Bromage, and D. H. Froula, "Transforming the Idler to Seed Raman Amplification."

D. Cao, P. W. McKenty, J. P. Knauer, and D. R. Harding, "Investigation of Acquired Fuel Motion Caused by Ice Roughness in OMEGA Cryogenic Experiments."

A. R. Christopherson, R. Betti, W. Theobald, C. J. Forrest, E. M. Campbell, J. Howard, J. A. Delettrez, C. Stoeckl, D. H. Edgell, W. Seka, V. Yu. Glebov, A. K. Davis, A. Bose, A. V. Maximov, M. S. Wei, and J. Peebles, "Direct Measurements of Hot-Electron Preheat in Inertial Confinement Fusion Implosions."

D. Clarkson, R. Ume, R. Sheets, S. P. Regan, T. C. Sangster, S. Padalino, and J. McLean, "Bulk Etch Rate and Swell Rate of CR-39."

T. J. B. Collins, R. Betti, A. Bose, A. R. Christopherson, V. N. Goncharov, J. P. Knauer, J. A. Marozas, F. J. Marshall, A. V. Maximov, D. T. Michel, A. Mora, P. B. Radha, S. P. Regan, W. Shang, A. Shvydky, C. Stoeckl, K. M. Woo, and G. Varchas, "Multidimensional Study of High-Adiabat OMEGA Cryogenic Experiments."

K. Cook, M. Coats, M. Yuly, S. Padalino, T. C. Sangster, and S. P. Regan, "Measurement of the 6He Decay Produced by the 9Be(n,α)6He Reaction."

R. S. Craxton, M. Hohenberger, W. E. Kehoe, F. J. Marshall, D. T. Michel, P. B. Radha, and M. J. Rosenberg, "Design of Platforms for Backlighting Spherical Implosions on OMEGA and the National Ignition Facility."

A. Davies, S. Bucht, J. Katz, D. Haberberger, I. A. Begishev, S.-W. Bahk, J. Bromage, J. D. Zuegel, D. H. Froula, J. D. Sadler, R. Trines, R. Bingham, and P. A. Norreys, "Picosecond Characterization of Underdense Plasmas for Studying Nonlinear Electron Plasma Wave Dynamics."

J. R. Davies, D. H. Barnak, R. Betti, E. M. Campbell, V. Yu. Glebov, J. P. Knauer, A. B. Sefkow, K. J. Peterson, D. B. Sinars, S. A. Slutz, and M. R. Weis, "Temperature Scaling for Magnetized Linear Inertial Fusion."

A. K. Davis, D. T. Michel, S. X. Hu, Y. Ding, R. Epstein, J. P. Knauer, and D. H. Froula, "Conduction-Zone Measurements Using X-Ray Self-Emission Images."

J. A. Delettrez, R. K. Follett, J. F. Myatt, and C. Stoeckl, "Evaluation of the Fast-Electron Source Function for Two-Plasmon Decay from the Temporal Hard X-Ray Emission."

D. H. Edgell, R. K. Follett, J. Katz, J. F. Myatt, J. G. Shaw, and D. H. Froula, "Three-Dimensional Modeling of Polarization Effects on Cross-Beam Energy Transfer in OMEGA Implosions."

R. Epstein, C. Stoeckl, V. N. Goncharov, P. W. McKenty, S. P. Regan, S. X. Hu, and I. V. Igumenshchev, "Simulation and Analysis of Time-Resolved Narrowband Radiographs of Cryogenic Implosions on OMEGA."

R. K. Follett, D. H. Edgell, D. H. Froula, V. N. Goncharov, I. V. Igumenshchev, J. G. Shaw, and J. F. Myatt, "Comparing Ray-Based and Wave-Based Models of Cross-Beam Energy Transfer."

C. J. Forrest, V. Yu. Glebov, V. N. Goncharov, J. P. Knauer, P. B. Radha, S. P. Regan, M. J. Rosenberg, T. C. Sangster, W. T. Shmayda, C. Stoeckl, and M. Gatu Johnson, "Measurements of Fusion Reaction Yield Ratios in Ignition-Relevant Direct-Drive Cryogenic Deuterium-Tritium Implosions."

D. H. Froula, D. Turnbull, D. H. Edgell, R. K. Follett, J. F. Myatt, T. J. Kessler, T. C. Sangster, M. Campbell, P. Michel, J. Weaver, and S. P. Obenschain, "Focused Cross-Beam Energy Transfer Experiments on OMEGA."

M. K. Ginnane, B. Kousar, J. Slish, K. Palmisano, S. Mandanas, S. J. Padalino, T. C. Sangster, S. P. Regan, C. Mileham, and C. Stoeckl, "TNSA Heavy Ion Measurements Using the Time-Resolved Tandem Faraday Cup."

V. Yu. Glebov, D. H. Barnak, J. R. Davies, J. P. Knauer, C. Stoeckl, R. Betti, S. P. Regan, T. C. Sangster, and E. M. Campbell, "Neutron Measurements in Laser-Driven MagLIF Experiments on OMEGA."

V. N. Goncharov, T. J. B. Collins, J. A. Marozas, S. P. Regan, E. M. Campbell, D. H. Froula, I. V. Igumenshchev, R. L. McCrory, J. F. Myatt, P. B. Radha, T. C. Sangster, and A. Shvydky, "High-Performance Cryogenic Designs for OMEGA and the National Ignition Facility."

M. C. Gregor, T. R. Boehly, G. W. Collins, R. Rygg, D. N. Polsin, B. J. Henderson, D. E. Fratanduono, P. M. Celliers, T. Braun, J. H. Eggert, C. A. McCoy, and D. D. Meyerhofer, "The Shock and Release Behavior of Diamond Compressed to 25 Mbar" (invited).

D. Haberberger, A. Davies, S. Bucht, J. Bromage, J. D. Zuegel, D. H. Froula, R. Trines, R. Bingham, P. A. Norreys, and J. Sadler, "Tunable Plasma-Wave Laser Amplifier."

L. Hao, R. Yan, J. Li, and C. Ren, "Development of a New Fluid Code to Study Laser-Plasma Instabilities."

H. Harrison, H. Seppala, H. Visca, P. Wakwella, K. Fletcher, S. Padalino, C. J. Forrest, S. P. Regan, and T. C. Sangster, "Characterizing Neutron Diagnostics on the nTOF Line at SUNY Geneseo."

R. F. Heeter, M. F. Ahmed, S. L. Ayers, J. A. Emig, C. A. Iglesias, D. A. Liedahl, M. B. Schneider, B. G. Wilson, E. J. Huffman, J. A. King, Y. P. Opachich, P. W. Ross, J. E. Bailey, G. A. Rochau, R. S. Craxton, E. M. Garcia, P. W. McKenty, R. Zhang, T. Cardenas, B. G. Devolder, E. S. Dodd, J. L. Kline,

M. E. Sherrill, and T. S. Perry, "Design of Initial Opacity Platform at the National Ignition Facility."

B. Henderson, T. R. Boehly, S. X. Hu, M. C. Gregor, D. N. Polsin, R. Rygg, G. W. Collins, D. E. Fratanduono, R. Kraus, J. H. Eggert, and P. M. Celliers, "Hugoniot Measurements of Silicon Shock Compressed to 25 Mbar."

M. Hohenberger, J. A. Marozas, P. W. McKenty, M. J. Rosenberg, P. B. Radha, D. Cao, J. P. Knauer, S. P. Regan, M. W. Bowers, J.-M. Di Nicola, G. Erbert, B. J. MacGowan, L. J. Pelz, and S. T. Yang, "Experimental Investigation of Cross-Beam Energy Transfer Mitigation via Wavelength Detuning in Directly Driven Implosions at the National Ignition Facility."

S. X. Hu, D. T. Michel, A. K. Davis, R. Betti, P. B. Radha, V. N. Goncharov, E. M. Campbell, D. H. Froula, C. Stoeckl, "Understanding Laser-Imprint Effects on Plastic-Target Implosions on OMEGA with New Physics Models."

I. V. Igumenshchev, D. T. Michel, R. C. Shah, E. M. Campbell, R. Epstein, C. J. Forrest, V. Yu. Glebov, V. N. Goncharov, J. P. Knauer, F. J. Marshall, R. L. McCrory, S. P. Regan, T. C. Sangster, C. Stoeckl, A. J. Schmitt, and S. P. Obenschain, "Three-Dimensional Hydrodynamic Simulations of OMEGA Implosions" (invited).

J. P. Knauer, S. X. Hu, V. N. Goncharov, and D. Haberberger, "Density Profile of a Foil Accelerated by Laser Ablation."

J. Li, R. Yan, and C. Ren, "Density-Modulation-Induced Absolute Laser-Plasma Instabilities in Inertial Confinement Fusion."

J. A. Marozas, M. J. Rosenberg, P. B. Radha, F. J. Marshall, W. Seka, D. Cao, P. W. McKenty, T. C. Sangster, S. P. Regan, V. N. Gonvharov, E. M. Campbell, R. L. McCrory, M. Hohenberger, M. W. Bowers, J.-M. Di Nicola, G. Erbert, B. J. MacGowan, L. J. Pelz, and S. T. Yang, "Wavelength Detuning Cross-Beam Energy Transfer Mitigation for Polar and Symmetric Direct Drive."

A. V. Maximov, H. Wen, J. F. Myatt, R. W. Short, W. Seka, M. J. Rosenberg, and C. Ren, "Laser–Plasma Interaction Near the Quarter-Critical Density in Direct-Drive Inertial Confinement Fusion."

P. W. McKenty, D. Cao, T. J. B. Collins, A. Shvydky, and K. S. Anderson, "Evaluations of Long-Wavelength Perturbations in OMEGA 80-Gbar Cryogenic Implosions."

D. T. Michel, S. X. Hu, A. K. Davis, E. M. Campbell, R. S. Craxton, V. Yu. Glebov, V. N. Goncharov, I. V. Igumenshchev, P. B. Radha, C. Stoeckl, and D. H. Froula, "Measurements of the Effect of Adiabat on the Shell Decompression in Direct-Drive Implosions on OMEGA."

J. F. Myatt, J. G. Shaw, R. K. Follett, D. H. Edgell, V. N. Goncharov, J. Bates, and J. Weaver, "A Wave-Based Model for Cross-Beam Energy Transfer in Direct-Drive Inertial Confinement Fusion Implosions" (invited).

P. M. Nilson, F. Ehrne, C. Mileham, D. Mastrosimone, R. K. Junquist, C. Taylor, R. Boni, J. Hassett, C. R. Stillman, S. T. Ivancic, D. J. Lonobile, R. W. Kidder, M. J. Shoup III, A. A. Solodov, C. Stoeckl, D. H. Froula, K. W. Hill, L. Gao, M. Bitter, P. Efthimion, and D. D. Meyerhofer, "High-Resolving-Power, Ultrafast Streaked X-Ray Spectroscopy on OMEGA EP."

Y. P. Opachich, P. W. Ross, R. F. Heeter, M. A. Barrios, D. A. Liedahl, M. J. May, M. B. Schneider, R. S. Craxton, E. M. Garcia, P. W. McKenty, R. Zhang, J. L. Weaver, K. A. Flippo, J. L. Kline, and T. S. Perry, "Iron Opacity Platform Performance Characterization at the National Ignition Facility."

A. Pak, "Shock-Wave Acceleration of Protons on OMEGA EP."

D. N. Polsin, T. R. Boehly, J. A. Delettrez, G. W. Collins, R. Rygg, M. C. Gregor, B. Henderson, C. A. McCoy, D. E. Fratanduono, R. Smith, R. Kraus, J. H. Eggert, F. Coppari, and P. M. Celliers, "Observation of Solid–Solid Phase Transitions in Ramp-Compressed Aluminum."

P. B. Radha, M. Hohenberger, J. A. Marozas, F. J. Marshall, M. J. Rosenberg, W. Seka, E. M. Campbell, D. H. Edgell, V. N. Goncharov, R. L. McCrory, P. W. McKenty, S. P. Regan, T. C. Sangster, J. D. Moody, H. Sio, J. A. Frenje, B. Lahmann, and R. D. Petrasso, "Signatures of Cross-Beam Energy Transfer Mitigation in Proof-of-Principle National Ignition Facility Direct-Drive Experiments."

S. P. Regan, V. N. Goncharov, R. Epstein, D. Cao, I. V. Igumenshchev, S. X. Hu, K. S. Anderson, R. Betti, M. J. Bonino, E. M. Campbell, T. J. B. Collins, C. J. Forrest, V. Yu. Glebov, D. R. Harding, J. A. Marozas, F. J. Marshall, P. W. McKenty, D. T. Michel, P. B. Radha, T. C. Sangster, C. Stoeckl, M. Schoff, R. Luo, and M. Farrell, "Hydrodynamic Mixing of Ablator Material into the Compressed Fuel and Hot Spot of Direct-Drive DT Cryogenic Implosions."

M. J. Rosenberg, F. H. Séguin, J. A. Frenje, H. Sio, M. Gatu Johnson, N. Sinenian, C. K. Li, R. D. Petrasso, P. W. McKenty, I. V. Igumenshchev, J. R. Rygg, V. Yu. Glebov, C. Stoeckl, W. Seka, F. J. Marshall, J. A. Delettrez, R. Betti, V. N. Goncharov, P. B. Radha, J. P. Knauer, T. C. Sangster, N. M. Hoffman, G. Kagan, A. Zylstra, H. W. Herrmann, R. E. Olson, D. D. Meyerhofer, H. G. Rinderknecht, P. A. Amendt, R. P. J. Town, S. Le Pape, M. Hohenberger, T. Ma, A. J. Mackinnon, S. C. Wilks, C. Bellei, D. T. Casey, O. L. Landen, J. D. Lindl, H.-S. Park, J. Pino, B. A. Remington, H. F. Robey, M. D. Rosen, A. Nikroo, S. Atzeni, W. Fox, and M. J.-E. Manuel, "Demonstration of Ion Kinetic Effects in Inertial Confinement Fusion Implosions and Investigation of Magnetic Reconnection Using Laser-Produced Plasmas" (invited).

M. J. Rosenberg, A. A. Solodov, W. Seka, J. F. Myatt, S. P. Regan, M. Hohenberger, A. V. Maximov, T. J. B. Collins, V. N. Goncharov, R. Epstein, R. W. Short, D. P. Turnbull, D. H. Froula, P. B. Radha, P. A. Michel, T. Chapman, J. D. Moody, L. Masse, C. Goyon, J. E. Ralph, M. A. Barrios, J. W. Bates, and A. J. Schmitt, "Planar Laser–Plasma Interaction Experiments at Direct-Drive Ignition-Relevant Scale Lengths at the National Ignition Facility."

W. Seka, M. J. Rosenberg, J. F. Myatt, A. A. Solodov, D. H. Edgell, R. W. Short, S. P. Regan, A. V. Maximov, P. Michel, C. S. Goyon, and J. D. Moody, "Stimulated Raman Scattering in Direct-Drive Inertial Confinement Fusion."

W. Shang, R. Betti, K. M. Woo, A. Bose, A. R. Christopherson, and S. X. Hu, "Two-Dimensional Simulations of Electron Shock Ignition at the Megajoule Scale."

J. L. Shaw, N. Lemos, L. D. Amorim, N. Vafaei-Najafabadi, K. A. Marsh, F. S. Tsung, W. B. Mori, and C. Joshi, "Direct Laser Acceleration of Electrons in a Laser Wakefield Accelerator with Ionization Injection."

R. Sheets, D. Clarkson, R. Ume, S. P. Regan, T. C. Sangster, S. Padalino, and J. Mclean, "Reduced Noise UV Enhancement of Etch Rates for Nuclear Tracks in CR-39."

R. W. Short, H. Wen, A. V. Maximov, J. F. Myatt, and W. Seka, "Relative Significance of the Stimulated Raman Scattering and Two-Plasmon–Decay Instabilities at Quarter-Critical Density."

A. Shvydky, M. Hohenberger, P. B. Radha, M. J. Rosenberg, K. S. Anderson, V. N. Goncharov, J. A. Marozas, F. J. Marshall,

P. W. McKenty, S. P. Regan, T. C. Sangster, J. M. Koning, M. M. Marinak, and L. Masse, "Three-Dimensional Evaluation of Laser Imprint in National Ignition Facility Multi-FM Smoothing by Spectral Dispersion Experiment."

A. A. Solodov, M. J. Rosenberg, J. F. Myatt, W. Seka, M. Hohenberger, R. Epstein, R. W. Short, J. G. Shaw, S. P. Regan, D. Turnbull, D. H. Froula, P. B. Radha, J. W. Bates, A. J. Schmitt, P. Michel, T. Chapman, J. D. Moody, J. E. Ralph, and M. A. Barrios, "Hot-Electron Generation at Direct-Drive Ignition-Relevant Plasma Conditions at the National Ignition Facility."

C. R. Stillman, P. M. Nilson, S. T. Ivancic, C. Mileham, I. A. Begishev, D. H. Froula, and I. E. Golovkin, "Picosecond Streaked K-Shell Spectroscopy of Near-Solid-Density Aluminum Plasmas."

C. Stoeckl, R. Epstein, R. Betti, W. Bittle, J. A. Delettrez, C. J. Forrest, V. Yu. Glebov, V. N. Goncharov, D. R. Harding, I. V. Igumenshchev, D. W. Jacobs-Perkins, R. T. Janezic, J. H. Kelly, T. Z. Kosc, R. L. McCrory, D. T. Michel, C. Mileham, P. W. McKenty, F. J. Marshall, S. F. B. Morse, S. P. Regan, P. B. Radha, B. S. Rice, T. C. Sangster, M. J. Shoup III, W. T. Shmayda, C. Sorce, W. Theobald, J. Ulreich, M. D. Wittman, D. D. Meyerhofer, J. A. Frenje, M. Gatu Johnson, and R. D. Petrasso, "Monochromatic Backlighting of Direct-Drive Cryogenic DT Implosions on OMEGA" (invited).

W. Theobald, R. Betti, A. Bose, W. Seka, C. Stoeckl, A. Casner, F. N. Beg, E. Llor Aisa, X. Ribeyre, V. Tikhonchuk, M. S. Wei, M. Vu, M. Hoppe Jr., M. E. Schoff, R. J. Florido, and R. Mancini, "The Generation of Gigabar Pressures for High-Energy-Density Plasmas."

D. Turnbull, P. A. Michel, C. Goyon, B. B. Pollock, G. E. Kemp, T. Chapman, D. Mariscal, L. Divol, J. S. Ross, S. Patankar, and J. D. Moody, "Measuring the Refractive Index of a Laser-Plasma Optical System."

R. J. Ward, G. M. Brown, D. Ho, B. F. O. F Stockler, C. G. Freeman, S. J. Padalino, and S. P. Regan, "Heavy Ion Beams from an Alphatross Source for Use in Calibration and Testing of Diagnostics."

K. M. Woo, R. Betti, R. Yan, H. Aluie, A. Bose, D. X. Zhao, and V. Gopalaswamy, "Study of Yield and Pressure Degradation in Inertial Confinement Fusion."

R. Yan, E. Borwick, R. Betti, J. Li, W. Theobald, and C. Ren, "Particle-in-Cell Simulations of Nonlinear Laser–Plasma Interactions and Hot-Electron Generation in the Shock-Ignition Regime."

————————

The following presentations were made at the 40th IEEE EDS Activities in Western New York Conference, Rochester, NY, 4 November 2016:

Y. Akbas, A. Jukna, L. Q. Zhang, Y. Almi, A. M. Song, I. Iñiguez-de-la-Torre, J. Mateos, T. González, T. Plecenik, P. Durina, A. Plecnik, G. Wicks, and R. Sobolewski, "Ultra-High Optical Responsivity of Semiconducting Asymmetric Nano-Channel Diodes."

G. Chen, R. Shrestha, A. Koroliov, A. Jukna, A. Amori, T. Krauss, Z. Staniszewski, E. Fray, A. Łaszcz, A. Czerwinski, M. C. Richter, and R. Sobolewski, "Characterization of Carbon Nanostructures Through THz Spectroscopy."

————————

The following presentations were made at the Rochester Academy of Science 43rd Annual Fall Session, Rochester, NY, 12 November 2016:

C. Fagan, M. Sharpe, W. T. Shmayda, and W. U. Schröder, "The Effect of Surface Modifications on Tritium Adsorption and Absorption by Stainless-Steel 316."

M. Sharpe, C. Fagan, and W. T. Shmayda, "Influence of the Water Layers Adsorbed onto Stainless-Steel 316 on Tritium Migration."

————————

B. P. Chock, D. R. Harding, and T. B. Jones, "Dispensing Surfactant-Containing Water Droplets Using Electrowetting," 2016 AIChE Annual Meeting, San Francisco, CA, 13–18 November 2016.

————————

P. M. Nilson, F. Ehrne, C. Mileham, D. Mastrosimone, R. K. Jungquist, C. Taylor, R. Boni, J. Hassett, C. R. Stillman, S. T. Ivancic, D. J. Lonobile, R. W. Kidder, M. J. Shoup III,

A. A. Solodov, C. Stoeckl, D. H. Froula, K. W. Hill, L. Gao, M. Bitter, P. Efthimion, and D. D. Meyerhofer, "High-Resolving-Power, Ultrafast Streaked X-Ray Spectroscopy on OMEGA EP," National Diagnostics Workshop, Livermore, CA, 29–30 November 2016.

———————

The following presentations were made at the 2016 International Workshop on Radiative Properties of Hot Dense Matter, Santa Barbara, CA, 5–9 December 2016:

R. Epstein, C. Stoeckl, V. N. Goncharov, P. W. McKenty, F. J. Marshall, S. P. Regan, R. Betti, W. Bittle, D. D. Harding, S. X. Hu, I. V. Igumenshchev, D. W. Jacobs-Perkins, R. T. Janezic, J. H. Kelly, T. Z. Kosc, C. Mileham, S. F. B. Morse, P. B. Radha, B. S. Rice, T. C. Sangster, M. J. Shoup III, W. T. Shmayda, C. Sorce, J. Ulreich, and M. D. Wittman, "Simulation and Analysis of Time-Resolved Narrowband Radiographs of Cryogenic Implosions on OMEGA."

S. T. Ivancic, P. M. Nilson, C. R. Stillman, C. Mileham, and D. H. Froula, "An Extreme Ultraviolet Spectrometer Suite for Characterization of Rapidly Heated Solid Matter."

P. M. Nilson, G. Fiksel, C. Stoeckl, P. A. Jaanimagi, C. Mileham, W. Theobald, J. R. Davies, J. F. Myatt, A. A. Solodov, D. H. Froula, R. Betti, and D. D. Meyerhofer, "Streaked X-Ray Imaging of Ultrafast Ionization Fronts Inside a Metal."

C. R. Stillman, P. M. Nilson, S. T. Ivancic, C. Mileham, I. A. Begishev, D. H. Froula, and I. E. Golovkin, "Picosecond Time-Resolved Observations of Dense Plasma Line Shifts."

———————

D. H. Froula, "Thomson Scattering in Laser-Produced Plasmas," Cornell Laboratory of Plasma Studies Seminar, Ithaca, NY, 7 December 2016.

———————

D. H. Froula, "Laser–Plasma Instabilities: The Pathway to Understanding and Control," NNSA Seminar, Washington, DC, 13 December 2016.

———————

T. C. Sangster, "The National Direct-Drive Program," Fusion Power Associates, Washington, DC, 13–14 December 2016.